NORSAR Scientific Report No. 2-2012

Semiannual Technical Summary

1 July – 31 December 2012

Tormod Kværna (Ed.)

Kjeller, June 2013

Table of Contents

1   Summary

This report provides summary information on operation and maintenance (O&M) activities at the Norwegian National Data Center (NOR-NDC) for CTBT verification during the period 1 July 2012 – 31 December 2012, as well as scientific and technical contributions relevant to verification in a broad sense. The O&M activities, including operation of monitoring stations and transmission links within Norway and to Vienna, Austria are being funded jointly by the CTBTO/PTS and the Norwegian Government, with the understanding that the funding of O&M activities for primary stations in the International Monitoring System (IMS) will gradually be transferred to the CTBTO/PTS. The O&M statistics presented in this report maintain consistency with long-standing reporting practices. Research activities described in this report are mainly funded by the Norwegian Government, with other sponsors acknowledged where appropriate.

A summary of the activities at NOR-NDC relating to field installations, data acquisition, data forwarding and processing during the reporting period is provided in chapters 2 – 4 of this report. Norway is contributing primary station data from two seismic arrays: the Norwegian Seismic Array NOA (IMS code PS27) and the Arctic Regional Seismic Array ARCES (IMS code PS28), one auxiliary seismic array on Spitsbergen (SPITS, IMS code AS72), and one auxiliary three-component station JMIC (IMS code AS73). These data are being provided to the International Data Centre (IDC) in Vienna via the Global Communications Infrastructure (GCI).

This report presents statistics for NOA, ARCES and SPITS, as well as for additional seismic stations which through cooperative agreements with institutions in the host countries provide continuous data to the NOR-NDC. These additional stations include the Finnish Regional Seismic Array (FINES, IMS code PS17) and the Hagfors array in Sweden (HFS, IMS code AS101).

So far among the Norwegian IMS stations, the NOA and the ARCES arrays (PS27 and PS28, respectively), the radionuclide station at Spitsbergen (RN49) and the auxiliary seismic stations on Spitsbergen (AS72) and Jan Mayen (AS73) have been certified. Provided that adequate funding continues to be made available (from the CTBTO/PTS and the Norwegian Ministry of Foreign Affairs), we envisage continuing the provision of data from these and other Norwegian IMS-designated stations in accordance with current procedures. As part of NORSAR's obsolescence management, a recapitalization plan for PS27 and PS28 was submitted to CTBTO/PTS in October 2008, with the purpose of preventing severe degradation of the stations due to lack of spare parts. The recapitalization of PS27 was concluded in 2012. In parallel the recapitalization of P28 has started with development and testing of particular equipment for PS28, like central timing system and hybrid sensor for surface vaults.

The IMS infrasound station IS37, originally planned to be located near Karasjok, will be established at another site, since the local authorities did not grant the permissions required. A site at Bardufoss, at 69.10° N, 18.60° E, has been approved by the municipal authorities for installation of IS37. The CTBTO Preparatory Commission has approved a corresponding coordinate change for the station.

Five scientific and technical contributions presented in chapter 6 of this report are provided as follows:

In section 6.1 we describe the analysis conducted at NORSAR of the February 12, 2013, announced nuclear test in North Korea. Seismic signals from the test were detected at all of NORSAR's array stations and, in addition to the standard detection and classification algorithms in operation, multi-channel waveform correlation detectors are operated in near real-time to detect close matches in the incoming data with the signals from the previous tests on October 9, 2006, and May 25, 2009. We provide a table of calibrated time-delays for the NOA array to generate a beam optimized for detecting P-arrivals from the site, and also illustrate the correlation detection made on the NOA array using the signal from the 2009 test as a template. We emphasize the importance of performing f-k analysis post-processing on the resulting correlation coefficient traces for running the detection process at aggressively low thresholds while maintaining an exceptionally low false alarm rate. The similarity of the arrivals at IMS stations globally allows for quite high-precision relative location estimates for the DPRK nuclear tests and we estimate the location of the 2013 event to be approximately 400 to 500 meters to the South West of the 2009 event.

Section 6.2 entitled "Automatic Parameter Extraction for Three-Component Observations" presents an algorithm on how the seismic signal parameters backazimuth (BAZ) and apparent velocity (V_{app}) can be estimated using data from single three-component stations. The algorithm is based on a two-stage approach. In the first stage, the best fitting values for BAZ and V_{app} are estimated for each of the three likely seismic phase types: P, S and Rg. In the second stage, the most likely seismic phase type is chosen by comparing typical polarity and amplitude relations between the different phase types. The theoretical background for the algorithm, as well as the different processing steps, is described in detail.

Section 6.3 presents analysis of an m_b 3.8 event in the north Ural Mountains on 24 December 2012 as observed at a newly established station in Amderma, northwest Russia. Waveforms and spectra are compared with observations at similar distances made in the 1990s at a previously operated station in Amderma, as well as with observations of underwater explosions at ARCES. For the time interval investigated (24 December 2012), the new Amderma station shows lower background noise levels at frequencies below 3 Hz as compared with the examples shown for the previously operated station (January and August 1997). This may be explained by microseisms caused by ocean waves in the open, ice-free Barents and Kara Seas during the Arctic summer. For frequencies above 3 Hz, higher noise levels are observed at the new station, indicating influence of anthropogenic noise sources. Without a detailed study of site effects at the new Amderma station, it is difficult to derive any firm conclusion regarding the characteristics of the 24 December 2012 event, but the large S/P ratio points in the direction of the event being an earthquake. The event is located in an area with no known mining activity, but the area is also characterized by very low natural seismicity.

Section 6.4 gives an overview on the instrument responses of infrasound sensors currently operational in the NORSAR station network. Since 2008, NORSAR has been running an experimental 3-site infrasound array at ARCES. This experimental array has been expanded in 2010 by a fourth site. In the beginning of 2013 NORSAR installed 9 infrasound sensors at sites of the A and B-ring of the NORES array. In NORES, as well as in ARCES, the sensors are co-located with seismic sensors.

In section 6.5, entitled "Classifying Seismic Signals at Small–Aperture Arrays via Stochastic Modeling of F-K Image Sequences", M. Ohrnberger and co-authors show how different features can be extracted from icequake signals recorded at the SPITS array. Initial results are shown on how these features can be analyzed with a Bayesian approach to classify unknown signals.

Tormod Kværna

2   Operation of International Monitoring System (IMS) Stations in Norway

2.1   PS27 — Primary Seismic Station NOA

The mission-capable data statistics were 99.993%, as compared to 99.940% for the previous reporting period. The net instrument availability was 98.180%.

There were no outages of all subarrays at the same time in the reporting period.

Monthly uptimes for the NORSAR on-line data recording task, taking into account all factors (field installations, transmissions line, data center operation) affecting this task were as follows:

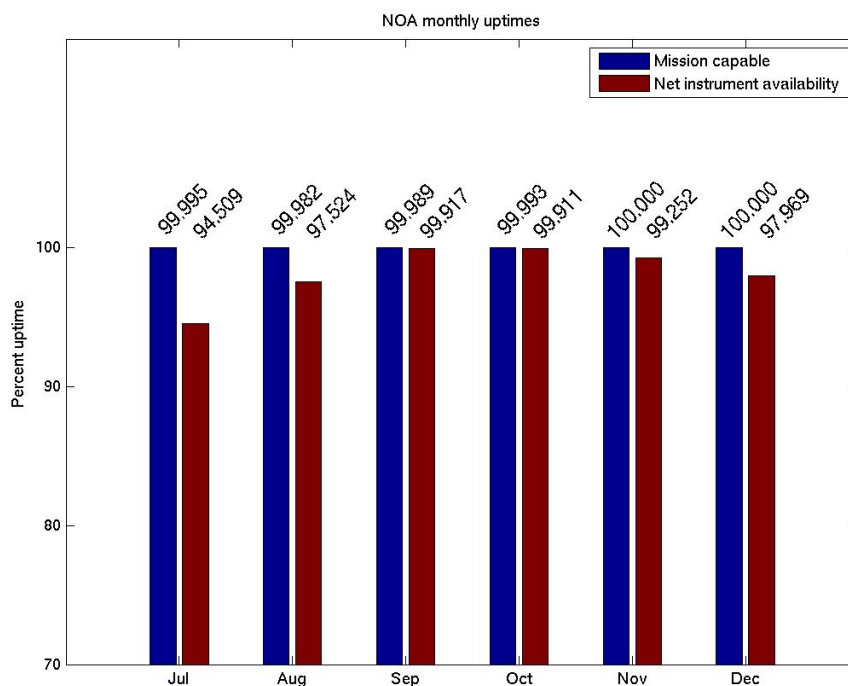|	Mission Capable	Net instrument availability
July 2012:	99.995	94.509
August 2012:	99.982	97.524
September 2012:	99.989	99.917
October 2012:	99.993	99.911
November 2012:	100.000	99.252
December 2012:	100.000	97.969

Fig. 2.1.1   Monthly uptimes for NOA for the period July – December 2012.

B. Paulsen

2.1.1 NOA event detection operation

In Table 2.1.1 some monthly statistics of the Detection and Event Processor operation are given. The table lists the total number of detections (DPX) triggered by the on-line detector, the total number of detections processed by the automatic event processor (EPX) and the total number of events accepted after analyst review (teleseismic phases, core phases and total).

	Total DPX	Total EPX	Accepted events		Sum	Daily average
			P-phases	Core Phases		
Jul 12	4030	741	313	85	398	12.8
Aug	5072	1010	323	79	402	13.0
Sep	6248	858	278	52	330	11.0
Oct	6860	1014	381	59	440	14.2
Nov	7574	951	242	50	292	9.7
Dec	7735	1048	305	64	369	11.9
	37519	5622	1842	389	2231	12.1

Table 2.1.1. Detection and event processor statistics, 1 July – 31 December 2012.
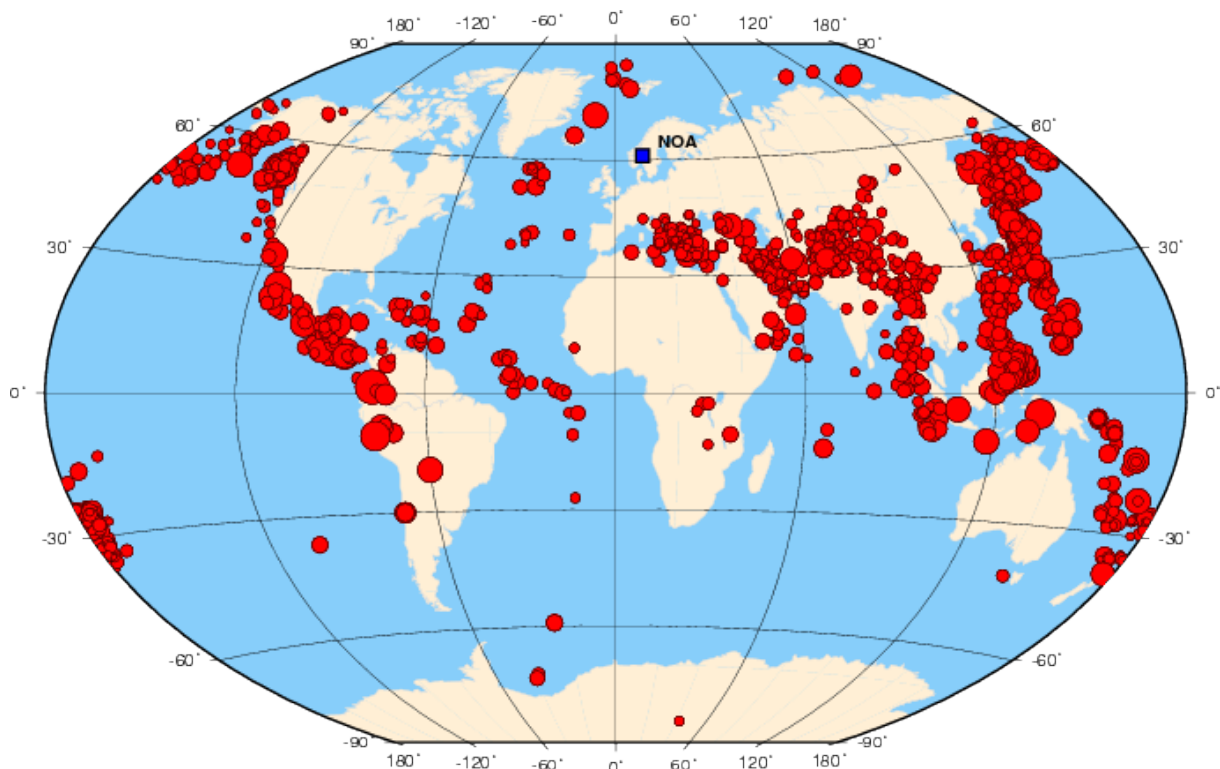

Fig. 2.1.2 Distribution of events in NORSAR's teleseismic reviewed bulletin for the time interval 1 July – 31 December 2012. Event symbols are scaled proportionally to event magnitude. The location of NOA is noted with a blue square. All locations are based on phase interpretation and inversion of slowness and backazimuth into a location, using the NOA array alone.

NOA detections

The number of detections (phases) reported by the NORSAR detector during day 183, 2012, through day 366, 2012, was 37,519, giving an average of 204 detections per processed day (184 days processed).

B. Paulsen
U. Baadshaug

2.2   PS28 — Primary Seismic Station ARCES

The mission-capable data statistics were 88.048%, as compared to 98.408% for the previous reporting period. The net instrument availability was 95.997%.

The main outages in the reporting period are presented in Table 2.2.1

Day	Period
Sep 28	08.17-15.04

Table 2.2.1. The main interruptions in recording of ARCES data at NOR-NDC, 1 July – 31 December 2012.

Monthly uptimes for the ARCES on-line data recording task, taking into account all factors (field installations, transmission lines, data center operation) affecting this task were as follows:

	Mission Capable	**Net instrument availability**
July 2012:	43.362	88.631
August 2012:	100.000	100.000
September 2012:	91.150	92.907
October 2012:	93.846	95.216
November 2012:	99.933	99.911
December 2012:	99.997	99.318
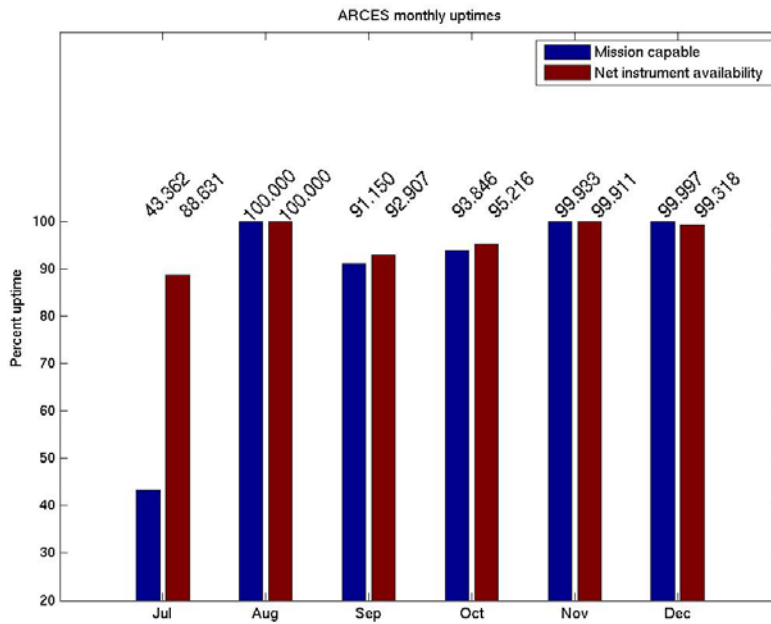
Fig. 2.2.1   Monthly uptimes for ARCES for the period July – December 2012.

B. Paulsen

2.2.1   Event detection operation

ARCES detections

The number of detections (phases) reported during day 183, 2012, through day 366, 2012, was 212,369, giving an average of 1,173 detections per processed day (181 days processed).

Events automatically located by ARCES

During day 183, 2012, through day 366, 2012, 9,451 local and regional events were located by ARCES, based on automatic association of P- and S-type arrivals. This gives an average of 52.5 events per processed day (180 days processed). 75% of these events are within 300 km, and 91% of these events are within 1000 km.

U. Baadshaug

2.3   AS72 — Auxiliary Seismic Station Spitsbergen

The mission-capable data for the period were 99.977%, as compared to 99.727% for the previous reporting period. The net instrument availability was 98.759%.
The main outages in the reporting period are presented in Table 2.3.1

Day	Period
Jul 30	07.53-08.08
Sep 12	08.56-09.13
Oct 19	09.20-09.37

Table 2.3.1. The main interruptions in recording of Spitsbergen data at NOR-NDC,
1 July – 31 December 2012.

Monthly uptimes for the Spitsbergen on-line data recording task, taking into account all factors (field installations, transmissions line, data center operation) affecting this task were as follows:

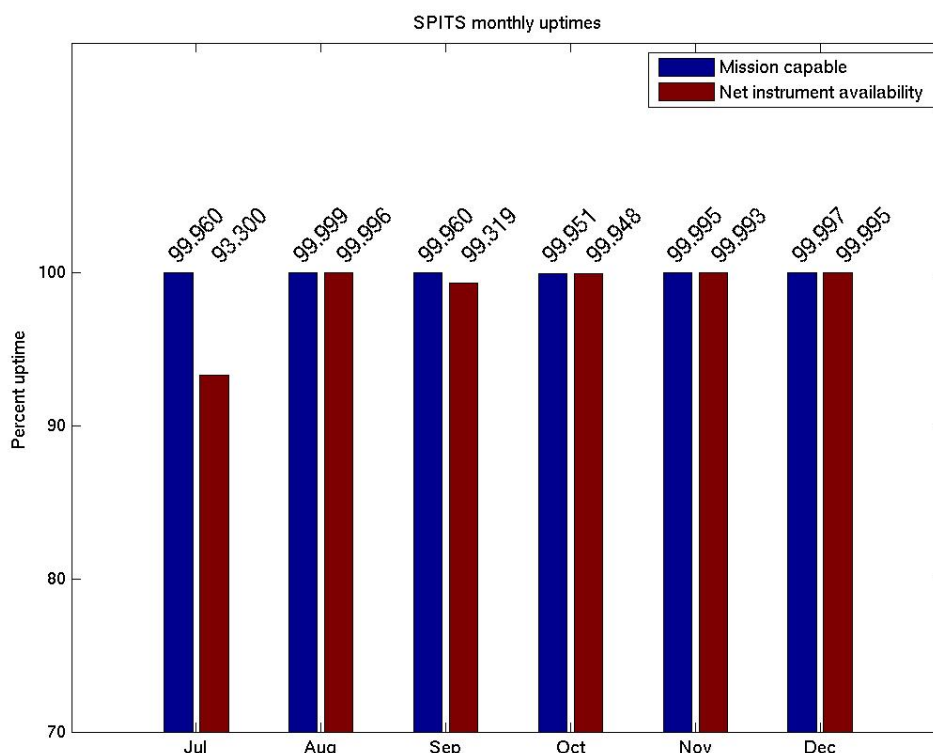|	Mission Capable	Net instrument availability
July 2012:	99.960	93.300
August 2012:	99.999	99.996
September 2012:	99.960	99.319
October 2012:	99.951	99.948
November 2012:	99.995	99.993
December 2012:	99.997	99.995

Fig. 2.3.1   Monthly uptimes for SPITS for the period July – December 2012.

B. Paulsen

2.3.1   Event detection operation

Spitsbergen array detections

The number of detections (phases) reported from day 183, 2012, through day 366, 2012, was 508,843, giving an average of 2,765 detections per processed day (184 days processed).

Events automatically located by the Spitsbergen array

During day 183, 2012, through day 366, 2012, 51,578 local and regional events were located by the Spitsbergen array, based on automatic association of P- and S-type arrivals. This gives an average of 280.3 events per processed day (184 days processed). 84% of these events are within 300 km, and 93% of these events are within 1000 km.

U. Baadshaug

2.4   AS73 — Auxiliary Seismic Station at Jan Mayen

The IMS auxiliary seismic network includes a three-component station on the Norwegian island of Jan Mayen. The station location given in the protocol to the Comprehensive Nuclear- Test-Ban Treaty is 70.9°N, 8.7°W.

The University of Bergen has operated a seismic station at this location since 1970. A so-called Parent Network Station Assessment for AS73 was completed in April 2002. A vault at a new location (71.0°N, 8.5°W) was prepared in early 2003, after its location had been approved by the PrepCom. New equipment was installed in this vault in October 2003, as a cooperative effort between NORSAR and the CTBTO/PTS. Continuous data from this station are being transmitted to the NDC at Kjeller via a satellite link installed in April 2000. Data are also made available to the University of Bergen.

The station was certified by the CTBTO/PTS on 12 June 2006.

J. Fyen

2.5   IS37 — Infrasound Station

The IMS infrasound network will, according to the protocol of the CTBT, include a station at Karasjok in northern Norway. The coordinates given for this station are 69.5°N, 25.5°E. These coordinates coincide with those of the primary seismic station PS28.

It has, however, proved impossible to obtain the necessary permits for use of land for an infrasound station at Karasjok. Various alternatives for locating the station at Karasjok were prepared, but all applications to the local authorities to obtain the permissions needed to establish the station were turned down by the local governing council in June 2007.

In 2008, investigations were initiated to identify an alternative site for IS37 outside Karasjok. A site at Bardufoss, at 69.1°N, 18.6°E, has now been approved by landowners and the municipal authorities for installation of IS37. The CTBTO preparatory Commission has approved the corresponding coordinate change for the station.

J. Fyen

2.6   RN49 — Radionuclide Station on Spitsbergen

The IMS radionuclide network includes a station on the island of Spitsbergen. This station has been selected to be among those IMS radionuclide stations that will monitor for the presence of relevant noble gases upon entry into force of the CTBT.

A site survey for this station was carried out in August of 1999 by NORSAR, in cooperation with the Norwegian Radiation Protection Authority. The site survey report to the PTS contained a recommendation to establish this station at Platåberget, near Longyearbyen. The infrastructure for housing the station equipment was established in early 2001, and a noble gas detection system, based on the Swedish "SAUNA" design, was installed at this site in May 2001, as part of CTBTO PrepCom's noble gas experiment. A particulate station ("ARAME" design) was installed at the same location in September 2001. A certification visit to the particulate station took place in October 2002, and the particulate station was certified on 10 June 2003. Both systems underwent substantial upgrading in May/June 2006. The noble gas system was certified on 21 December 2012. The equipment at RN49 is being maintained and operated under a contract with the CTBTO/PTS.

S. Mykkeltveit

3   Contributing Regional Arrays

3.1   NORES

NORES had been out of operation since lightning destroyed the station electronics on 11 June 2002.

The station has been rebuilt and is operational in an experimental mode (9 inner sites instrumented with 3-component sensors) since December 2011.

B. Paulsen

3.2   Hagfors (IMS Station AS101)

Data from the Hagfors array are made available continuously to NORSAR through a cooperative agreement with Swedish authorities.

The mission-capable data statistics were 100%, as compared to 99.939% for the previous reporting period. The net instrument availability was 100%.

Monthly uptimes for the Hagfors on-line data recording task, taking into account all factors (field installations, transmission lines, data center operation) affecting this task were as follows:

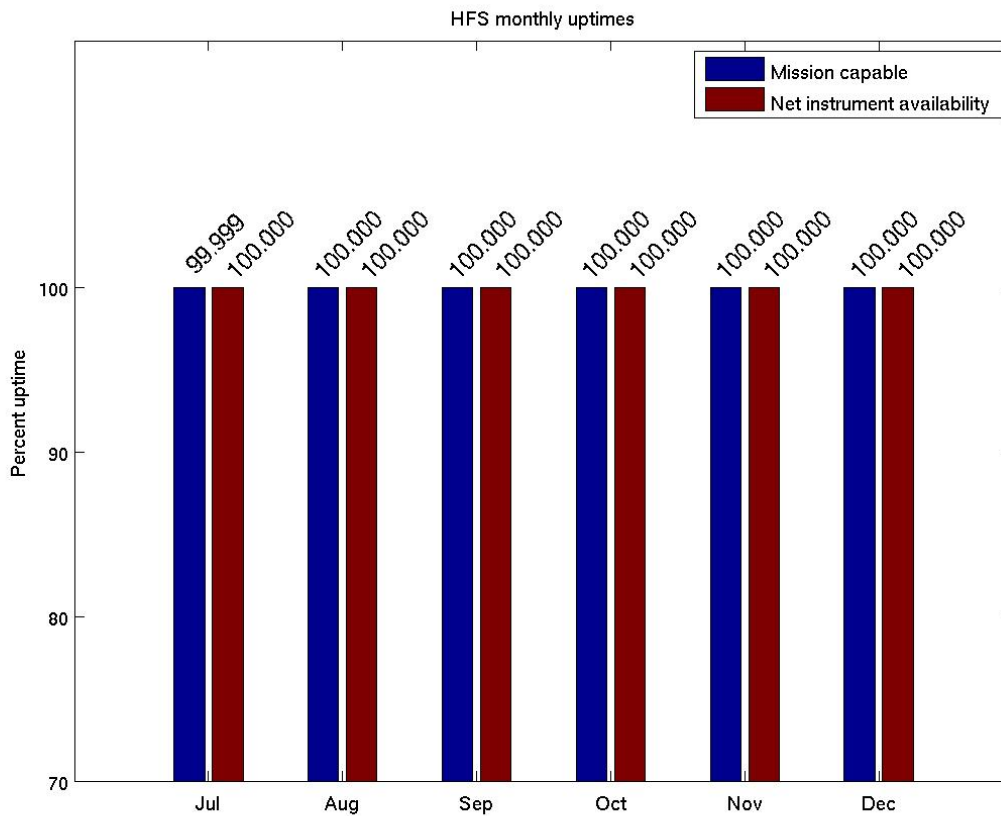|	Mission Capable	Net instrument availability
July 2012:	99.999%	100%
August 2012:	100%	100%
September 2012:	100%	100%
October 2012:	100%	100%
November 2012:	100%	100%
December 2012:	100%	100%

HFS monthly uptimes

Fig. 3.2.1   Monthly uptimes for HFS for the period July – December 2012.

B. Paulsen

3.2.1   Hagfors event detection operation

Hagfors array detections

The number of detections (phases) reported from day 183, 2012, through day 366, 2012, was 118,498, giving an average of 644 detections per processed day (184 days processed).

Events automatically located by the Hagfors array

During day 183, 2012, through 366, 2012, 4,579 local and regional events were located by the Hagfors array, based on automatic association of P- and S-type arrivals. This gives an average of 24.9 events per processed day (184 days processed). 78% of these events are within 300 km, and 94% of these events are within 1000 km.

U. Baadshaug

3.3 FINES (IMS Station PS17)

Data from the FINES array are made available continuously to NORSAR through a cooperative agreement with Finnish authorities.

The mission-capable data statistics were 96.431%, as compared to 99.935% for the previous reporting period. The net instrument availability was 95.741%.

Monthly uptimes for the FINES on-line data recording task, taking into account all factors (field installations, transmissions line, data center operation) affecting this task were as follows:

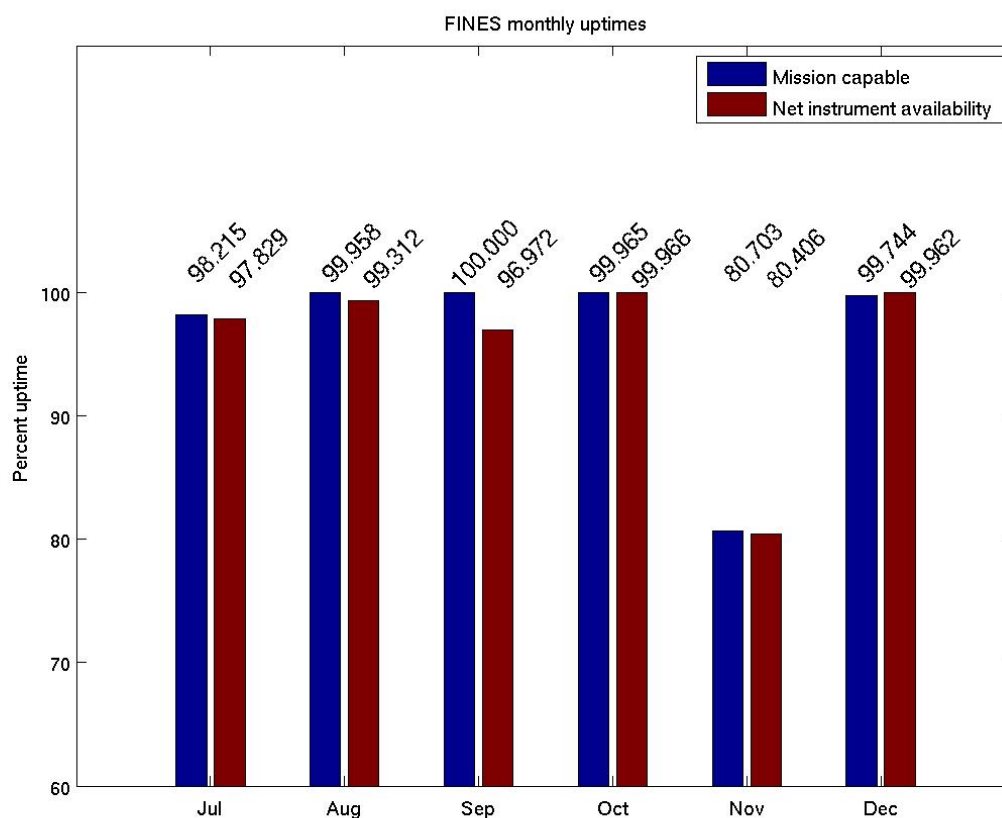|	Mission Capable	Net instrument availability
July 2012:	98.215%	97.829%
August 2012:	99.958%	99.312%
September 2012:	100%	96.972%
October 2012:	99.965%	99.966%
November 2012:	80.703%	80.406%
December 2012:	99.744%	99.962%

Fig. 3.3.1   Monthly uptimes for FINES for the period July – December 2012.

B. Paulsen

3.3.1   FINES event detection operation

FINES detections

The number of detections (phases) reported during day 183, 2012, through day 366, 2012, was 30,219, giving an average of 178 detections per processed day (170 days processed).

Events automatically located by FINES

During day 183, 2012, through 366, 2012, 1,796 local and regional events were located by FINES, based on automatic association of P- and S-type arrivals. This gives an average of 10.6 events per processed day (170 days processed). 89% of these events are within 300 km, and 94% of these events are within 1000 km.

U. Baadshaug

3.4   Regional Monitoring System Operation and Analysis

The Regional Monitoring System (RMS) was installed at NORSAR in December 1989 and has been operated from 1 January 1990 for automatic processing of data from ARCES and NORES. A second version of RMS that accepts data from an arbitrary number of arrays and single 3-component stations was installed at NORSAR in October 1991, and regular operation of the system comprising analysis of data from the 4 arrays ARCES, NORES, FINES and GERES started on 15 October 1991. As opposed to the first version of RMS, the one in current operation also has the capability of locating events at teleseismic distances.

Data from the Apatity array was included on 14 December 1992, and from the Spitsbergen array on 12 January 1994. Detections from the Hagfors array were available to the analysts and could be added manually during analysis from 6 December 1994. After 2 February 1995, Hagfors detections were also used in the automatic phase association.

Since 24 April 1999, RMS has processed data from all the seven regional arrays ARCES, NORES, FINES, GERES (until January 2000), Apatity, Spitsbergen, and Hagfors. Starting 19 September 1999, waveforms and detections from the NOA array have also been available to the analyst.

3.4.1   Phase and event statistics

Table 3.4.1 gives a summary of phase detections and events declared by RMS. From top to bottom the table gives the total number of detections by the RMS, the number of detections that are associated with events automatically declared by the RMS, the number of detections that are not associated with any events, the number of events automatically declared by the RMS, and finally the total number of events worked on interactively (in accordance with criteria that vary over time; see below) and defined by the analyst.

New criteria for interactive event analysis were introduced from 1 January 1994. Since that date, only regional events in areas of special interest (e.g, Spitsbergen, since it is necessary to acquire new knowledge in this region) or other significant events (e.g, felt earthquakes and large industrial explosions) were thoroughly analyzed. Teleseismic events of special interest are also analyzed.

To further reduce the workload on the analysts and to focus on regional events in preparation for Gamma-data submission during GSETT-3, a new processing scheme was introduced on 2 February 1995. The GBF (Generalized Beamforming) program is used as a pre-processor to RMS, and only phases associated with selected events in northern Europe are considered in the automatic RMS phase association. All detections, however, are still available to the analysts and can be added manually during analysis.

	Jul 12	Aug 12	Sep 12	Oct 12	Nov 12	Dec 12	Total
Phase detections	132474	157199	170086	177547	130303	153686	921295
- Associated phases	7664	10213	9629	9074	6453	6878	49911
- Unassociated phases	124810	146986	160457	168473	123850	146808	871384
Events automatically declared by RMS	2071	2648	2281	2009	1380	1372	11761
No. of events defined by the analyst	50	53	64	39	39	50	295

Table 3.4.1. RMS phase detections and event summary 1 July - 30 December 2012.

U. Baadshaug

B. Paulsen

4 The Norwegian National Data Center and Field Activities

4.1 NOR-NDC Activities

NORSAR functions as the Norwegian National Data Center (NOR-NDC) for CTBT verification. Six monitoring stations, comprising altogether 97 seismic and infrasound waveform systems plus radionuclide monitoring equipment, will be located on Norwegian territory as part of the future IMS, as described elsewhere in this report. The four seismic IMS stations are all in operation today, and all of them are currently providing data to the CTBTO/PTS on a regular basis. PS27, PS28, AS72, AS73 and RN49 are all certified. Data recorded by the Norwegian stations are being transmitted in real time to the NOR-NDC, and provided to the IDC through the Global Communications Infrastructure (GCI). Norway is connected to the GCI with a frame relay link to Vienna.

Operating the Norwegian IMS stations continues to require significant efforts by personnel both at the NOR-NDC and in the field. Strictly defined procedures as well as increased emphasis on regularity of data recording and timely data transmission to the IDC in Vienna have led to increased reporting activities and implementation of new procedures for the NOR-NDC. The NOR-NDC carries out all the technical tasks required in support of Norway's treaty obligations. NORSAR will also carry out assessments of events of special interest, and advise the Norwegian authorities in technical matters relating to treaty compliance. A challenge for the NOR-NDC is to carry 40 years' experience over to the next generation of personnel.

4.1.1 Verification functions; information received from the IDC

After the CTBT enters into force, the IDC will provide data for a large number of events each day, but will not assess whether any of them are likely to be nuclear explosions. Such assessments will be the task of the States Parties, and it is important to develop the necessary national expertise in the participating countries. An important task for the NOR-NDC will thus be to make independent assessments of events of particular interest to Norway, and to communicate the results of these analyses to the Norwegian Ministry of Foreign Affairs.

4.1.2 Monitoring the Arctic region

Norway will have monitoring stations of key importance for covering the Arctic, including Novaya Zemlya, and Norwegian experts have a unique competence in assessing events in this region. On several occasions in the past, seismic events near Novaya Zemlya have caused political concern, and NORSAR specialists have contributed to clarifying these issues.

4.1.3 International cooperation

After entry into force of the treaty, a number of countries are expected to establish national expertise to contribute to the treaty verification on a global basis. Norwegian experts have been in contact with experts from several countries with the aim of establishing bilateral or multilateral cooperation in this field.

4.1.4 NORSAR event processing

The automatic routine processing of NORSAR events as described in NORSAR Sci. Rep. No. 2-93/94, has been running satisfactorily. The analyst tools for reviewing and updating the solutions have been continually modified to simplify operations and improve results. NORSAR is currently applying teleseismic detection and event processing using the large-aperture NOA array, as well as regional monitoring using the network of small-aperture arrays in Fennoscandia and adjacent areas.

4.1.5 Communication topology

Norway has implemented an independent subnetwork, which connects the IMS stations AS72, AS73, PS28, and RN49 operated by NORSAR to the GCI at the NOR-NDC. A contract has been concluded and VSAT antennas have been installed at each station in the network. Under the same contract, VSAT antennas for 6 of the PS27 subarrays have been installed for intra-array communication. The seventh subarray is connected to the central recording facility via a leased land line. The central recording facility for PS27 is connected directly to the GCI (Basic Topology). All VSAT communication is functioning satisfactorily. As of 10 June 2005, AS72 and RN49 are connected to the NOR-NDC through a VPN link.

Jan Fyen

4.2 Status Report: Provision of Data from Norwegian Seismic IMS Stations to the IDC

4.2.1 Introduction

This contribution is a report for the period July – December 2012 on activities associated with provision of data from Norwegian seismic IMS stations to the International Data Centre (IDC) in Vienna. This report represents an update of contributions that can be found in previous editions of NORSAR's Semiannual Technical Summary. All four Norwegian seismic stations providing data to the IDC have been formally certified.

4.2.2 Norwegian IMS stations and communications arrangements

During the reporting interval, Norway has provided data to the IDC from the four seismic stations shown in Fig. 4.2.1. PS27 — NOA is a 60 km aperture teleseismic array, comprising of 7 subarrays, each containing five vertical broadband sensors and one three-component hybrid broadband instrument. PS28 — ARCES is a 25-element regional array with an aperture of 3 km, whereas AS72 — Spitsbergen array (station code SPITS) has 9 elements within a 1-km aperture. AS73 — JMIC has a single three-component broadband instrument.

The intra-array communication for NOA utilizes a land line for subarray NC6 and VSAT links based on iDirect technology for the other 6 subarrays. The central recording facility for NOA is located at the Norwegian National Data Center (NOR-NDC).

Continuous ARCES data are transmitted from the ARCES site to the NOR-NDC using the same iDirect network as NOA.

Continuous SPITS data were transmitted to NOR-NDC via a VSAT terminal located at Platåberget in Longyearbyen (which is the site of the IMS radionuclide monitoring station RN49 installed during 2001) up to 10 June 2005. The central recording facility (CRF) for the SPITS array has been moved to the University entre in Svalbard (UNIS). Data from the array elements to the CRF are transmitted via a 2.4 Ghz radio link (Wilan VIP-110). A 512 Kbps SHDSL link has been established between UNIS and NOR-NDC. Both AS72 and RN49 data are now transmitted to NOR-NDC over this link using VPN technology.

A minimum of 14-day station buffers have been established at the ARCES and SPITS sites and at all NOA subarray sites, as well as at the NOR-NDC for ARCES, SPITS and NOA. In addition, each individual site of the SPITS array has a 14-day buffer.

The NOA and ARCES arrays are primary stations in the IMS network, which implies that data from these stations are transmitted continuously to the receiving International Data Centre. Since October 1999, these data have been transmitted (from NOR-NDC) via the Global Communications Infrastructure (GCI) to the IDC in Vienna. Data from the auxiliary array station SPITS — AS72 have been sent in continuous mode to the IDC during the reporting period. AS73 — JMIC is an auxiliary station in the IMS, and also this station is transmitted in continuous mode to the IDC. In addition, continuous data from all three arrays is transmitted to the US_NDC under a bi-lateral agreement.

NORSAR also provides broadband data from Norwegian IMS stations to ORFEUS and IRIS.

4.2.3   Uptimes and data availability

Figs. 4.2.2 and 4.2.3 show the monthly uptimes for the Norwegian IMS primary stations ARCES and NOA, respectively, for the reporting period given as the hatched (taller) bars in these figures. These barplots reflect the percentage of the waveform data that is available in the NOR-NDC data archives for these two arrays. The downtimes inferred from these figures thus represent the cumulative effect of field equipment outages, station site to NOR-NDC communication outage, and NOR-NDC data acquisition outages.

Figs. 4.2.2 and 4.2.3 also give the data availability for these two stations as reported by the IDC in the IDC Station Status reports. The main reason for the discrepancies between the NOR-NDC and IDC data availabilities as observed from these figures is the difference in the ways the two data centers report data availability for arrays: Whereas NOR-NDC reports an array station to be up and available if at least one channel produces useful data, the IDC uses weights where the reported availability (capability) is based on the number of actually operating channels.

4.2.4   NOR-NDC automatic processing and data analysis

These tasks have proceeded in accordance with the descriptions given in Mykkeltveit and Baadshaug (1996). For the reporting period NOR-NDC derived information on 284 supplementary events in northern Europe and submitted this information to the Finnish NDC as the NOR-NDC contribution to the joint Nordic Supplementary (Gamma) Bulletin. These events are plotted in Fig. 4.2.4.

4.2.5   Current developments and future plans

NOR-NDC is continuing the efforts towards improving and hardening all critical data acquisition and data forwarding hardware and software components, so as to meet the requirements related to operation of IMS stations.

The NOA array was formally certified by the PTS on 28 July 2000, and a contract with the PTS in Vienna currently provides partial funding for operation and maintenance of this station. The ARCES array was formally certified by the PTS on 8 November 2001, and a contract with the PTS is in place which also provides for partial funding of the operation and maintenance of this station. The operation of the two IMS auxiliary seismic stations on Norwegian territory (Spitsbergen and Jan Mayen) is funded by the Norwegian Ministry of Foreign Affairs. Provided that adequate funding continues to be made available (from the PTS and the Norwegian Ministry of Foreign Affairs), we envisage continuing the provision of data from all Norwegian seismic IMS stations without interruption to the IDC in Vienna.

The PS27 - NOA equipment was recapitalized during 2010-2012, and has been revalidated. The PS28 - ARCES equipment was acquired in 1999, and it is no longer possible to get spare digitizers. A recapitalization plan for the array was submitted to the PTS in October 2008, and development of and testing of specific equipment for that array is ongoing.

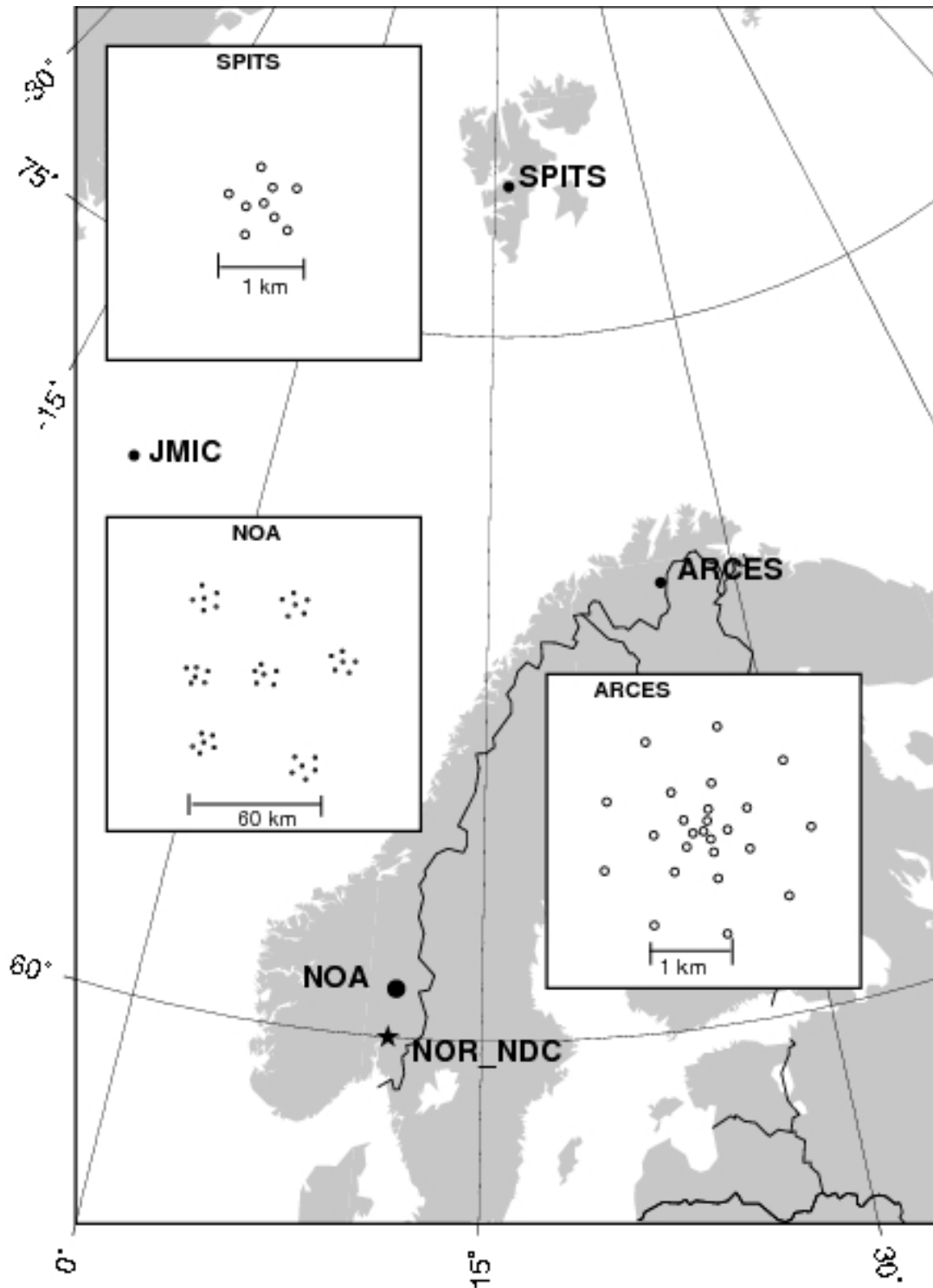**U. Baadshaug**
S. Mykkeltveit
J. Fyen

Fig. 4.2.1.   The figure shows the locations and configurations of the three Norwegian seismic IMS array stations that provided data to the IDC during the period July – December 2012. The data from these stations and the JMIC three-component station are transmitted continuously and in real time to the Norwegian NDC (NOR-NDC). The stations NOA and ARCES are primary IMS stations, whereas SPITS and JMIC are auxiliary IMS stations.
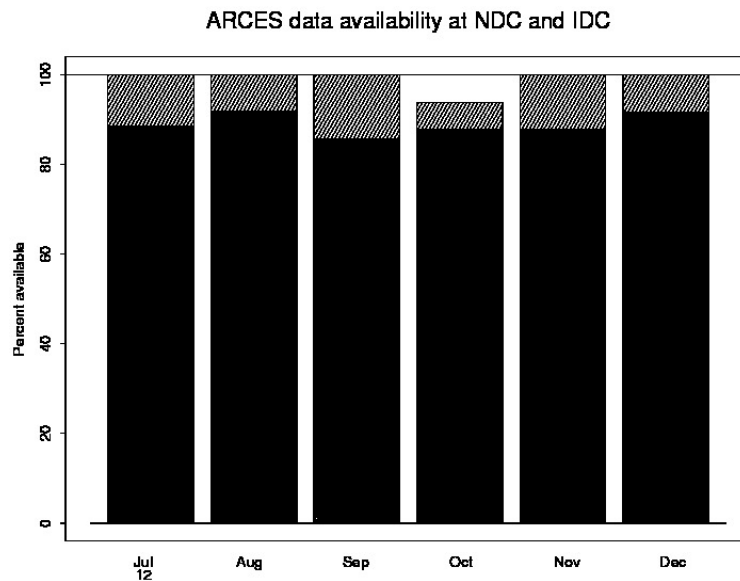
Fig. 4.2.2 *The figure shows the monthly availability of ARCES array data for the period July – December 2012 at NOR-NDC and the IDC. See the text for explanation of differences in definition of the term "data availability" between the two centers. The higher values (hatched bars) represent the NOR-NDC data availability.*
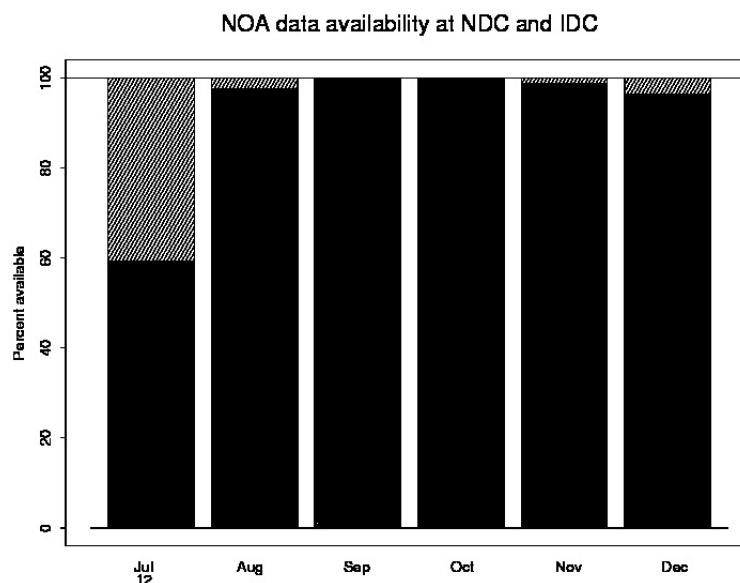

Fig. 4.2.3 *The figure shows the monthly availability of NORSAR array data for the period July – December 2012 at NOR-NDC and the IDC. See the text for explanation of differences in definition of the term "data availability" between the two centers. The higher values (hatched bars) represent the NOR-NDC data availability.*

Reviewed Supplementary events

Fig. 4.2.4   The map shows the 284 events in and around Norway contributed by NOR-NDC during July – December 2012 as supplementary (Gamma) events to the IDC, as part of the Nordic supplementary data compiled by the Finnish NDC. The map also shows the main seismic stations used in the data analysis to define these events.

4.3   Field Activities

The activities at the NORSAR Maintenance Center (NMC) at Hamar currently include work related to operation and maintenance of the following IMS seismic stations: the NOA teleseismic array (PS27), the ARCES array (PS28) and the Spitsbergen array (AS72). Some work has also been carried out in connection with the seismic station on Jan Mayen (AS73), the radionuclide station at Spitsbergen (RN49), and preparations for the infrasound station IS37. NORSAR also acts as a consultant for the operation and maintenance of the Hagfors array in Sweden (AS101).

NORSAR carries out the field activities relating to IMS stations in a manner generally consistent with the requirements specified in the appropriate IMS Operational Manuals, which are currently being developed by Working Group B of the Preparatory Commission. For seismic stations these specifications are contained in the Operational Manual for Seismological Monitoring and the International Exchange of Seismological Data (CTBT/WGB/TL-11/2), currently available in a draft version.

All regular maintenance on the NORSAR field systems is conducted on a one-shift-per-day, five-day-per-week basis. The maintenance tasks include:

- Operating and maintaining the seismic sensors and the associated digitizers, authentication devices and other electronics components.

- Maintaining the power supply to the field sites, as well as backup power supplies.

- Operating and maintaining the VSATs, the data acquisition systems and the intra-array data transmission systems.

- Assisting the NDC in evaluating the data quality and making the necessary changes in gain settings, frequency response and other operating characteristics as required.

- Carrying out preventive, routine and emergency maintenance to ensure that all field systems operate properly.

- Maintaining a computerized record of the utilization, status, and maintenance history of all site equipment.

- Providing appropriate security measures to protect against incidents such as intrusion, theft and vandalism at the field installations.

Details of the daily maintenance activities are kept locally. As part of its contract with CTBTO/PTS, NORSAR submits, when applicable, problem reports, outage notification reports and equipment status reports. The contents of these reports and the circumstances under which they will be submitted are specified in the draft Operational Manual.

P.W. Larsen
K.A. Løken

5 Documentation Developed

Backe, S., E. Enger, S. Hustveit, S. Høibråten, H. Kippe, S. Mykkeltveit, O. Reistad, T. Sekse, R.S. Sidhu, C. Waters, D. Chambers, H. White, I. Russell, K. Allen and A. Collinson (2012). The United Kingdom – Norway Initiative: Further Research into Managed Access of Inspectors During Warhead Dismantlement Verification. Proceedings of the 53rd Annual Meeting of the Institute of Nuclear Materials Management, Orlando, FL, July 15-19, 2012.

Gibbons, S.J.(2013). Detection and Location of the February 12, 2013, Announced Nuclear Test in North Korea. In: Semiannual Technical Summary, 1 July – 31 December 2012, NORSAR, Kjeller, Norway.

Harris, D. B., S. J. Gibbons, A. J. Rodgers and M. E. Pasyanos (2012). Nuclear Test Ban Treaty Verification: Improving Test Ban Monitoring with Empirical and Model-Based Signal Processing. IEEE signal processing magazine, doi: 10.1109/MSP.2012.2184869.

Kværna, T., S.G. Antonovskaya, Y. Konechnaya and V.E. Asming (2013). The Ural Mountains Event on 24 December 2012. In: Semiannual Technical Summary, 1 July – 31 December 2012, NORSAR, Kjeller, Norway.

Harris, D. B., S. J. Gibbons, A. J. Rodgers and M. E. Pasyanos (2012). Nuclear Test Ban Treaty Verification: Improving Test Ban Monitoring with Empirical and Model-Based Signal Processing. IEEE signal processing magazine, doi: 10.1109/MSP.2012.2184869.

Ohrnberger, M., C. Hammer, N. Giannotis and J. Schweitzer (2013). Classifying Seismic Signals at Small–Aperture Arrays via Stochastic Modeling of F-K Image Sequences. In: Semiannual Technical Summary, 1 July – 31 December 2012, NORSAR, Kjeller, Norway.

Roth, M. and M. Pirli (2013). Responses of the Infrasound Channels of ARCES and NORES: In: Semiannual Technical Summary, 1 July – 31 December 2012, NORSAR, Kjeller, Norway.

Schweitzer, J. (2013). Automatic Parameter Extraction for Three-Component Observations. In: Semiannual Technical Summary, 1 July – 31 December 2012, NORSAR, Kjeller, Norway.

6   Technical Reports / Papers Published

6.1   Detection and Location of the February 12, 2013, Announced Nuclear Test in North Korea

On February 12, 2013, The Democratic Peoples' Republic of Korea (the DPRK, or North Korea) announced that a nuclear test had been carried out. This was the third test of its kind, the first two having occurred on October 9, 2006, and May 25, 2009. Prior to the announcement by the DPRK, the Comprehensive Nuclear-Test-Ban Treaty Organization (CTBTO) had released a statement to say that seismic stations of the International Monitoring System (IMS) for verifying compliance with the treaty had detected "an unusual seismic event in the DPRK which measured 4.9 in magnitude"[1]. 25 stations of the primary seismic network contributed to the fully automatic SEL3 (Standard Event List 3) seismic event location estimate. Two primary IMS seismic stations operated by NORSAR, NOA (PS27) and ARCES (PS28), were among these stations.

The location estimates of the three DPRK nuclear tests, together with the origin time and m_b magnitude estimates, as provided in the Reviewed Event Bulletin (REB) of the International Data Centre (IDC) of the CTBTO, are displayed in Table 6.1.1.

Date	Origin time (UTC) in format yyyy-doy:hh.mm.ss.ss where doy is the Julian day	Latitude	Longitude	m_b magnitude estimate
October 9, 2006	2006-282:01.35.27.58	41.3119	129.0189	4.1
May 25, 2009	2009-145:00.54.42.80	41.4110	129.0464	4.5
February 12, 2013	2013-043:02.57.50.80	41.3005	129.0652	4.9

Table 6.1.1: Origins for the three DPRK nuclear tests provided in the REB of the IDC.

All of the solutions given have depth fixed to zero.

In this short summary we

- display the signals from the three DPRK nuclear tests recorded on the NOA array

- discuss the detection of the 2013 tests using a matched filter detector on the NOA array using the signal from the 2009 test as a waveform template

- discuss the location of the 2013 DPRK test relative to the location of the 2006 and 2009 tests. For this final investigation, waveform data from many IMS seismic stations were used.

---

[1] http://www.ctbto.org/the-treaty/developments-after-1996/2013-dprk-announced-nuclear-test/

6.1.1   Observations of the February 12, 2013, DPRK Nuclear Test on the NOA array

The large aperture NOA array in southern Norway was operational at the times of all of the three DPRK nuclear tests. Between the times of the 2009 and 2013 events, the short period vertical sensors were replaced with broadband instruments. A beam on the NOA array is shown for each of the three events in Fig. 6.1.1; all traces are shown to a common scale and all are corrected to a common instrument response.
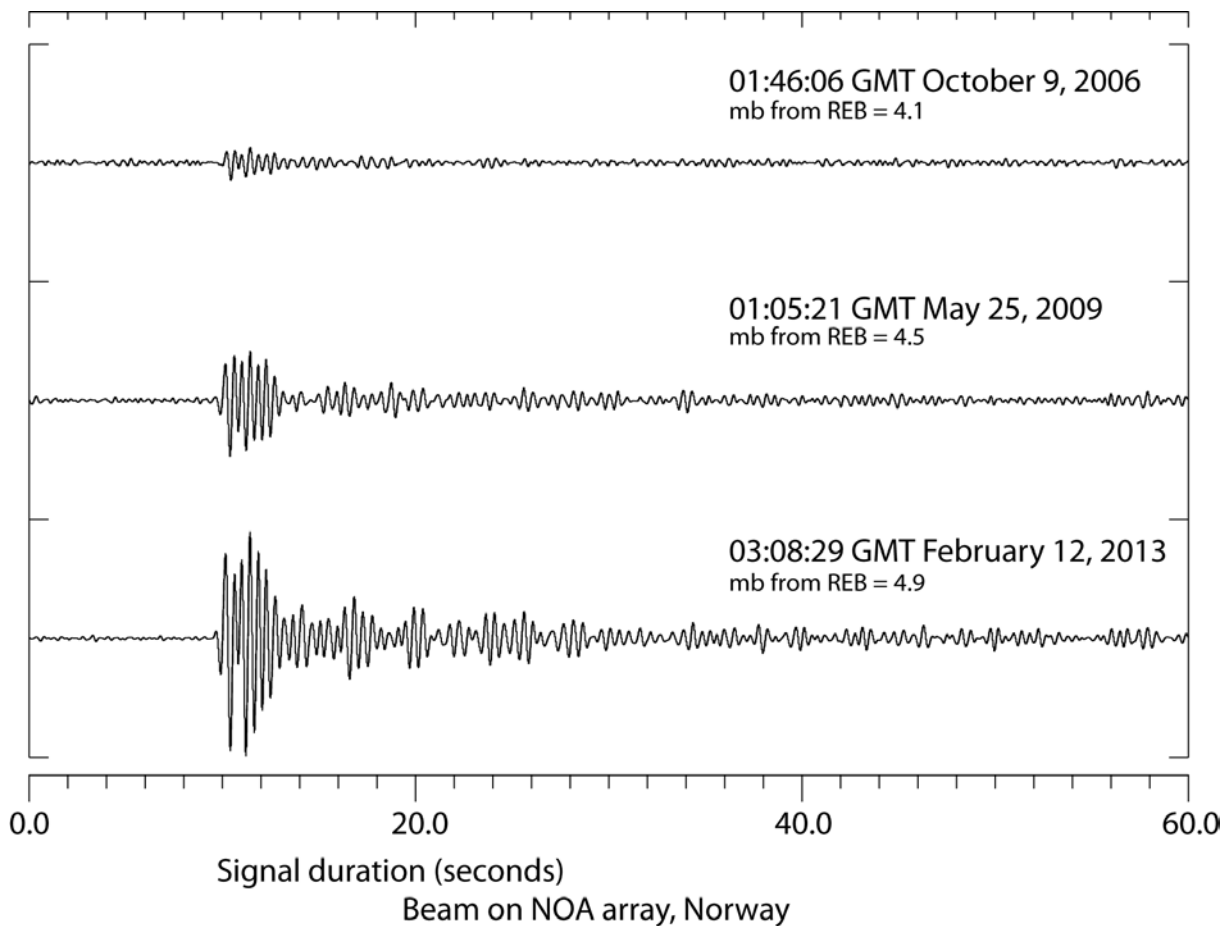

Fig. 6.1.1 *Beam on the NOA array (PS27) for the three DPRK nuclear tests displayed to a common scale. A bandpass filter 1-5 Hz has been applied to all traces and the 2013 signal on the new broadband instruments has been transformed to the instrument response of the short period sensors which recorded the first two tests (so that the signal amplitudes for all 3 events are directly comparable). The times displayed give the starting times of the traces; the arrival of the P phase comes approximately 10 seconds later.*

It has long been recognized that delay times over the large aperture NOA array based upon a plane-wave propagation model alone give poor signal alignment and result in significant destructive interference under the beamforming operation. The beams displayed in Fig. 6.1.1 are calculated using the semi-empirical time-delays provided in the Table 6.1.2 (see Gibbons et al., 2009, for further details).

Site	Predicted plane-wave time-delay (seconds) vel 17.3 km/s, azi 46.67^{o}	Estimated correction term (vel 17.3 km/s, azi 46.67 degrees)	Actual time-delay applied to channel (seconds)
NAO00	1.822	-0.348	1.474
NAO01	1.608	-0.308	1.299
NAO02	1.754	-0.344	1.410
NAO03	2.034	-0.346	1.688
NAO04	2.039	-0.337	1.702
NAO05	1.732	-0.274	1.458
NBO00	1.028	-0.075	0.953
NBO01	0.878	-0.054	0.824
NBO02	0.767	-0.085	0.682
NBO03	0.972	-0.128	0.845
NBO04	1.168	-0.100	1.068
NBO05	1.025	-0.034	0.991
NB200	0.000	0.000	0.000
NB201	-0.222	0.093	-0.129
NB202	0.002	0.005	0.007
NB203	0.234	0.102	0.336
NB204	0.084	0.093	0.177
NB205	-0.099	0.095	-0.004
NC200	-0.210	0.212	0.002
NC201	-0.466	0.221	-0.246
NC202	-0.264	0.220	-0.043
NC203	-0.039	0.164	0.125
NC204	-0.026	0.221	0.195
NC205	-0.370	0.272	-0.098
NC300	-1.425	0.109	-1.316
NC301	-1.660	0.092	-1.568
NC302	-1.429	0.103	-1.326
NC303	-1.163	0.103	-1.060
NC304	-1.314	0.116	-1.199
NC305	-1.560	0.130	-1.431
NC400	-1.311	0.099	-1.213
NC401	-1.499	0.146	-1.352
NC402	-1.248	0.054	-1.194
NC403	-1.086	0.017	-1.070
NC404	-1.230	0.070	-1.159
NC405	-1.451	0.132	-1.319
NC600	0.732	-0.310	0.422
NC601	0.423	-0.297	0.126
NC602	0.596	-0.325	0.270
NC603	0.867	-0.347	0.520
NC604	0.967	-0.339	0.628
NC605	0.711	-0.295	0.416

Table 6.1.2: Time-delays for construction of the NOA array beam (reference site NB200) for the DPRK nuclear test site.

6.1.2   Detection of the signal from the DPRK nuclear test using multi-channel correlation detectors

Signals from the February 12, 2013, DPRK event were detected with a high signal-to-noise ratio (SNR) at many seismic stations globally. However, in addition to the routine processing of the incoming seismic data for unknown signals, NORSAR operates in real time a number of so-called correlation or matched filter detectors for signals from sites of special interest from which seismic events have previously been observed (see Gibbons and Ringdal, 2006). The North Korea nuclear test site is naturally one of these sites of interest. Several templates, consisting of the signals from the 2006 and 2009 DPRK nuclear tests recorded on the various seismic arrays to which NORSAR has access to real-time data, are correlated with the incoming waveform data and the process is connected to an alarm system for occasions on which a trigger is declared. All correlation detectors which run on array datastreams (as opposed to 3-component data streams) are subject to a post-processing system for filtering out false alarms on each occasion for which a preliminary detection is made. This involves performing f-k analysis on the single channel detection statistic traces in order to confirm that the detected wavefront approached the array from the same direction as the master event wavefront (the principle is described in Section 4 of Gibbons and Ringdal, 2006). Gibbons and Ringdal (2012) describe a multi-channel correlation detector for the North Korea test site on data from the MJAR array in Japan and demonstrated that the application of this post-processing system reduced the number of detections made in a 3 year period from several thousand to fewer than 10. Fig. 6.1.2 displays the detection of the 2013 DPRK nuclear test, by performing correlation on the NOA array, using a waveform template from the 2009 DPRK event.

The corresponding slowness grid from the f-k post-processing system is displayed in Fig. 6.1.3. The zero slowness vector confirms that the NOA array is unable to differentiate between the direction of arrival of the detected signal and the direction of arrival of the master signal. This is strong evidence that the detected signal came from a location very close to the site of the 2009 DPRK nuclear test. It should be noted that the templates taken from both the 2006 and 2009 events on the NOA array generated clear detections which easily passed the f-k analysis post-processing system. The similarity between the 2009 and 2013 signals was far greater than that between the 2006 and 2013 signals, although the 2013 event signal was sufficiently similar to the significantly smaller 2006 signal for a clear correlation detection to be made.
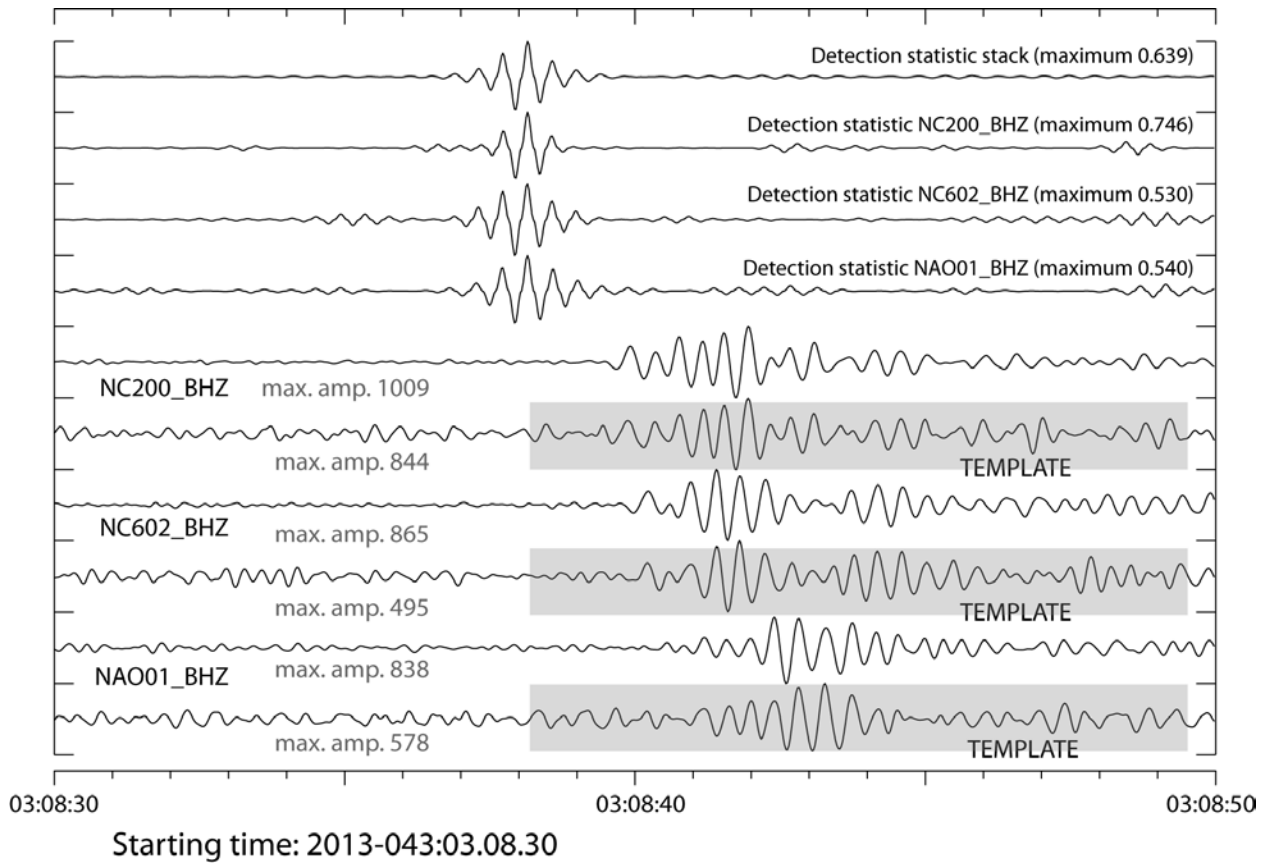
Fig. 6.1.2   *Detection of the February 12, 2013, event on the NOA array using a signal template from the May 25, 2009, DPRK nuclear test. The 60 second long waveform template begins at a time 01.05.30 UTC on 2009-145 and the maximum value is reached at a time of 03.08.38.153 UTC on 2013-043. The "detection statistic" is the square of the correlation coefficient but preserving the sign (see Gibbons and Ringdal, 2012, for details).*
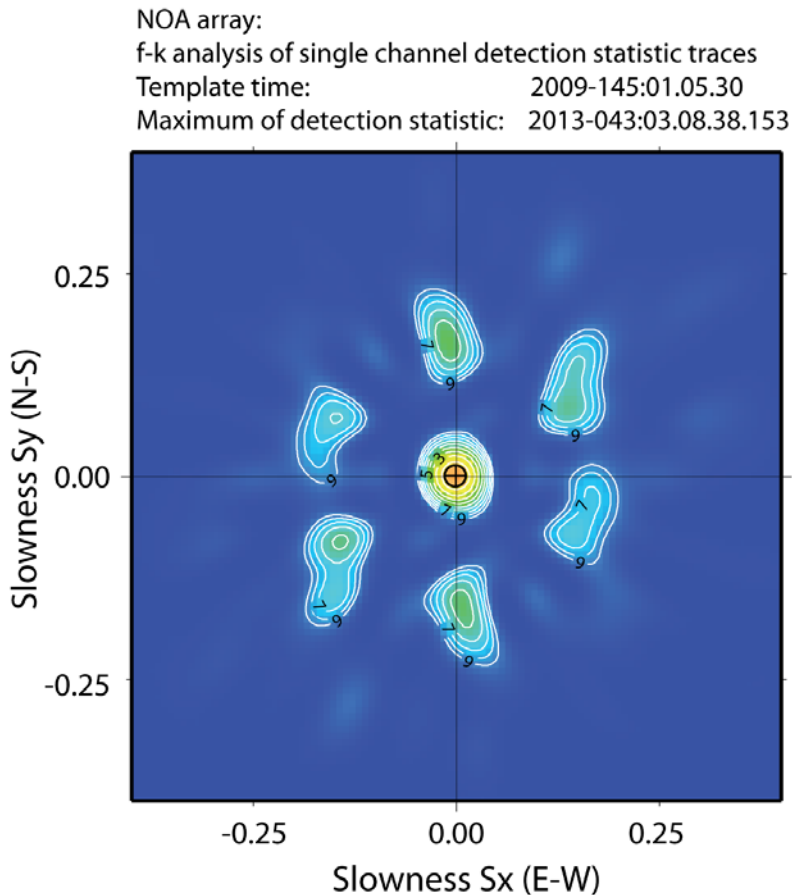
NOA array:
f-k analysis of single channel detection statistic traces
Template time: 2009-145:01.05.30
Maximum of detection statistic: 2013-043:03.08.38.153

Fig. 6.1.3   f-k analysis of the detection statistic traces in a 2-second long window centered on a time 2013-043:03.08.38.153 for each of the 42 vertical channels of the NOA array. The maximum beam-gain is for the zero slowness vector (i.e. with zero time-delay), the implication being that the detected wavefront approached the array from exactly the same direction as the wavefront in the waveform template. See Gibbons and Ringdal (2006) for details.

6.1.3   Location of the 2013 DPRK nuclear test relative to the 2006 and 2009 events

When two seismic events occur very close to each other, there may be sufficient similarity between the signals generated at any given station that very accurate relative times may be calculated by cross-correlating the one waveform against the other. The accuracy in these relative arrival times can exceed greatly the accuracy with which the arrival of a seismic phase can be read on a seismogram and, by measuring these very small time differences at many seismic stations observing the event from different directions, we may be able to locate the two events relative to each other with a high level of confidence. This principle forms the basis of the double difference location algorithms (e.g. Richards et al., 2006; Waldhauser and Ellsworth, 2000) which have been used to create earthquake catalogs of unprecedented detail.

When North Korea carried out their second nuclear test in 2009, it was evident that the signals generated by this explosion were very similar to those generated by the test in 2006. Several independent studies (Murphy et al., 2010; Selby, 2010; Wen and Long, 2010) examined closely the time differences between stations, both regional and global, and there is general agreement that the location of the explosion in 2009 is approximately 2 km to the West and slightly to the North of the 2006 test. These high precision relative location estimates have also been examined in relation to high-resolution satellite imagery of the test-site region (see also Schlittenhardt et al., 2010). Fig. 6.1.4 shows the locations that Wen and Long (2010) provide for the 2006 and 2009 tests based on both precision seismology and analysis of satellite imagery. The symbol to the right is the location of the 2006 explosion.
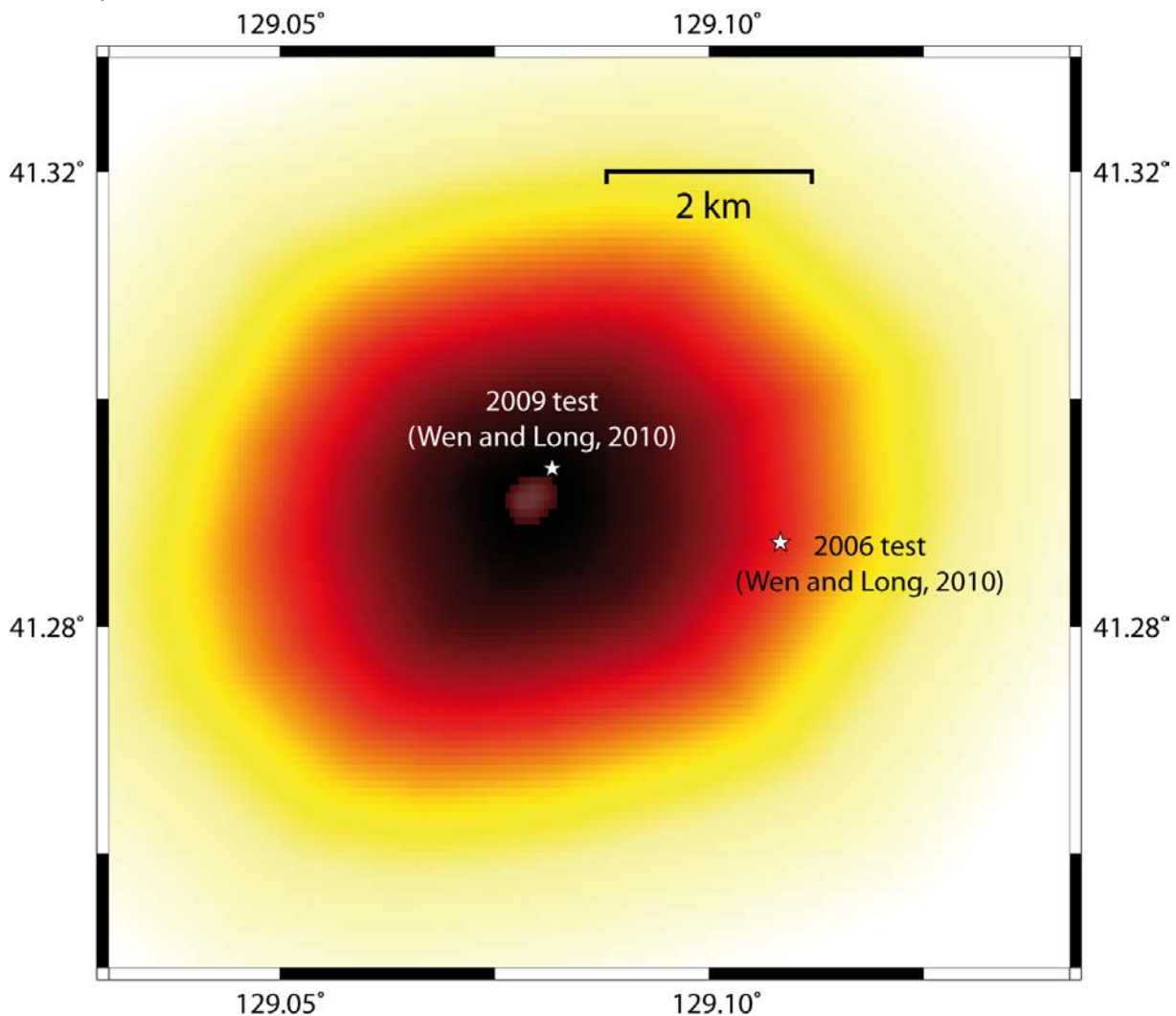

Fig. 6.1.4 *A grid of trial epicenters for the 2013 test scanned for goodness-of-fit between the predicted and observed traveltime differences using the method of Selby (2010). The white stars indicate the locations of the 2009 and 2006 explosions as provided by Wen and Long (2010). The location of the May 25, 2009, DPRK explosion is fixed at $41.2939^{o}N$ and $129.0817^{o}E$ and the colours indicate the size of the misfit. The minimum residual is associated with a location very close to the assumed site of the 2009 explosion: within 500 meters and to the South West. The depth was held constant for all trial hypocenters.*

The signals generated by the test on February 12, 2013, are remarkably similar to those generated by the test in 2009. Using correlation-based travel-time differences from selected IMS seismic stations (see Fig. 6.1.5), and applying the grid-search method of Selby (2010), we fixed the location of the 2009 test at 41.2939° N and 129.0817° E and calculated a residual or misfit for a grid of trial epicenters for the location of the 2013 explosion. The location with the smallest misfit value is located within 500 meters of the assumed site of the 2009 explosion and somewhat to the South West (Fig. 6.1.4). The geometrical distribution of observing stations is very good and the location of this optimal fit appears to be quite stable to the removal of selected stations from the inverse problem.
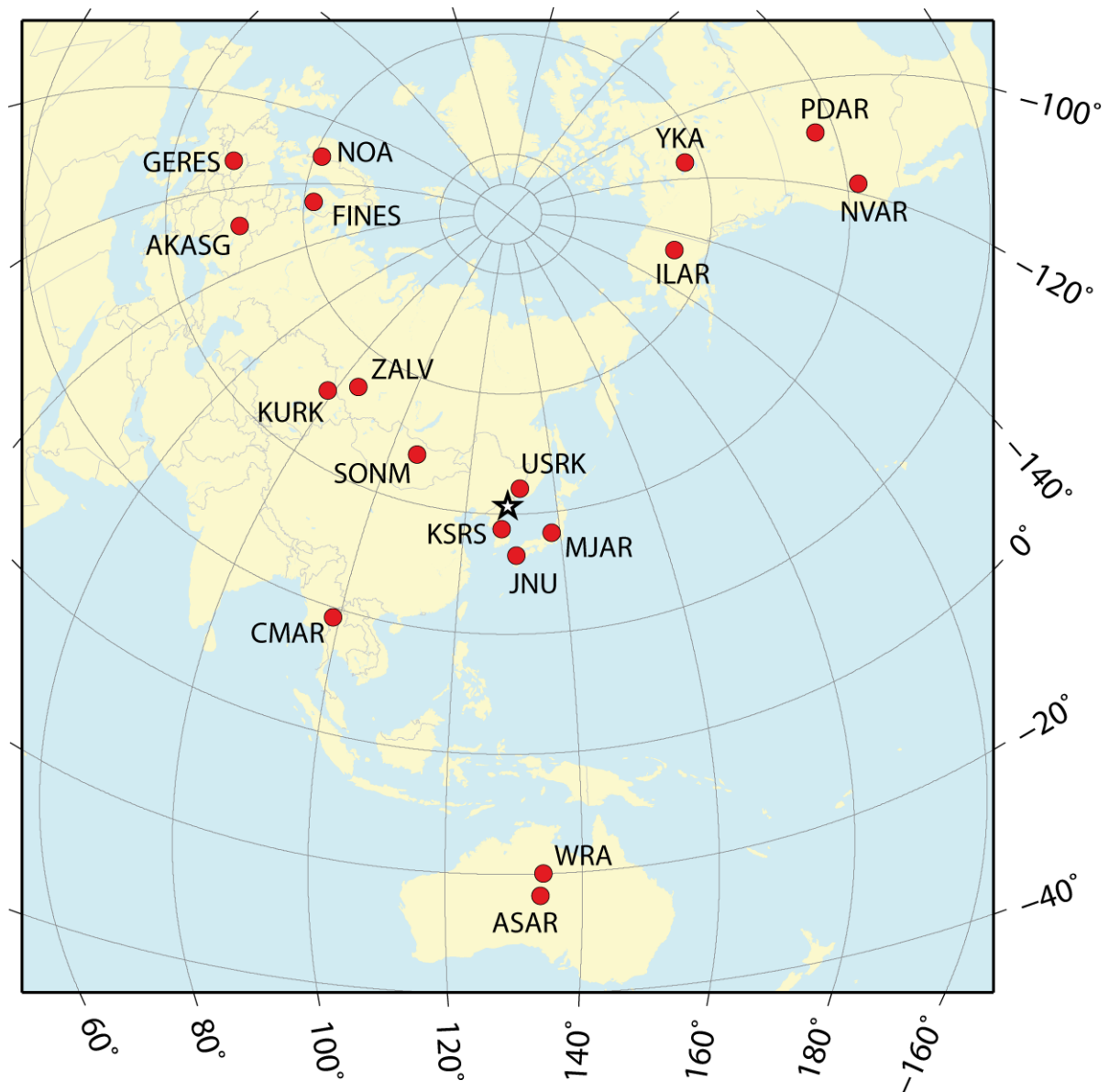

Fig. 6.1.5   IMS stations used in the relative location of the 2009 and 2013 DPRK nuclear tests.

6.1.4   Summary

The seismic signals generated by the February 12, 2013, nuclear test in the DPRK were detected clearly by seismic stations globally. The primary IMS stations in Norway, NOA and ARCES, both recorded the signals from this event with a high SNR.

In addition, the 2013 DPRK nuclear test was readily detected on the NOA array with a correlation detector using waveform templates from both the 2006 and 2009 DPRK events. Both detections passed the f-k post-processing screen which we deem to be essential for running correlation detectors at aggressively low detection thresholds with exceedingly low false alarm rates.

Using cross-correlation based relative time estimates on a selection of IMS seismic stations, using the method of Selby (2010), we estimate the location of the 2013 event to be approximately 400 to 500 meters to the South West of the 2009 event.

Acknowledgements

Steven J. Gibbons

References

Gibbons, S. J. and F. Ringdal (2006). The detection of low magnitude seismic events using array-based waveform correlation, Geophys. J. Int. 165, 149–165. http://dx.doi.org/10.1111/j.1365-246x.2006.02865.x

Gibbons, S. J., J. Fyen, J. and F. Ringdal (2009). SEISMO-11/J: Construction and Application of Time-Delay Correction Surfaces for Improved Detection and Estimation on Seismic Arrays, Poster presented at the ISS09 conference in Vienna. pdf-file of poster can be downloaded from the URL http://www.ctbto.org/specials/the-international-scientific-studies-project-iss/scientific-contributions/seismologyposters/

Gibbons, S. J. and F. Ringdal (2012). Seismic Monitoring of the North Korea Nuclear Test Site Using a Multichannel Correlation Detector, IEEE Transactions on Geoscience and Remote Sensing. 50, 1897–1909. http://dx.doi.org/10.1109/tgrs.2011.2170429

Murphy, J.R., B.C. Kohl, J.L. Stevens, T.J. Bennett and H.G. Israelsson (2010). Exploitation of the IMS and other data for a comprehensive, advanced analysis of the North Korean nuclear tests, in: Proceedings of the 2010 Monitoring Research Review: Ground-Based Nuclear Explosion Monitoring Technologies. Report LA-UR-10-05578. Los Alamos National Laboratory, pp. 456–465. http://www.rdss.info/librarybox/mrr/MRR2010/PAPERS/04-11.PDF

Richards, P., F. Waldhauser, D. Schaff and W.-Y. Kim (2006). The Applicability of Modern Methods of Earthquake Location. Pure and Applied Geophysics 163, 351–372. http://dx.doi.org/10.1007/s00024-005-0019-5

Schlittenhardt, J., M. Canty and I. Grünberg (2010). Satellite Earth Observations Support CTBT Monitoring: A Case Study of the Nuclear Test in North Korea of Oct. 9, 2006 and Comparison with Seismic Results. Pure and Applied Geophysics 167, 601–618. http://dx.doi.org/10.1007/s00024-009-0036-x

Selby, N.D. (2010). Relative locations of the October 2006 and May 2009 DPRK announced nuclear tests using International Monitoring System seismometer arrays. Bulletin of the Seismological Society of America. Volume 100 (4), pp. 1779-1784. http://dx.doi.org/10.1785/0120100006

Waldhauser, F. and W.L. Ellsworth (2000). A Double-Difference Earthquake Location Algorithm: Method and Application to the Northern Hayward Fault, California. Bulletin of the Seismological Society of America 90, 1353–1368. http://dx.doi.org/10.1785/0120000006

Wen, L. and H. Long (2010). High-precision Location of North Korea's 2009 Nuclear Test. Seismological Research Letters 81, 26–29. http://dx.doi.org/10.1785/gssrl.81.1.26

6.2   Automatic Parameter Extraction for Three-Component Observations

6.2.1   Introduction

The development of data processing software at NORSAR concentrated during the last decades on reliable results for an automatic analysis of array data. NORSAR's system of STA/LTA detectors on different filtered data streams can easily be copied to the case of a single 3-component (3C) station, just without involving any beamforming of data from different array sites. However, any further data analysis and parameter extraction cannot be adapted so easily to an automatic analysis of 3C data. Although an analyst will recognize in most cases just by visual inspection the type of a seismic onset (P or S or surface phase), an automated analysis tool will encounter problems. The challenge in any 3C data analysis is reliable phase type identification, and without any possibility to measure the later parameters with an array, *e.g.*, by fk-analysis, the estimation of backazimuth (BAZ) and incidence angle (INC). INC is related to the apparent velocity, as measured with an array, via Snell's law.

Observations of seismic phases do not obviously show their character at first face: P- as well as S-phases are usually recorded with adequate amplitudes on all components of a 3C station. The analysis of the particle motion (polarization analysis) should solve the problem because the seismic phases can be separated after rotating the 3C traces of the station (ZNE) into a ray oriented Cartesian coordinate system (LQT): *e.g.*, pure P-phases should be only visible on the Longitudinal-trace (L-component), pure S-phases should be only visible on the two perpendicular oriented coordinates Q- (for SV-energy) and T- (for SH-energy), and the surface phase Rg should only have energy on the L- and Q-components.

However, real data are rarely pure onsets because P-to-SV and SV-to-P conversions occur at discontinuities and lateral heterogeneities. In addition, coda energy caused by the scattering of seismic waves, can be observed for all onsets, and may arrive at the observing station even from different BAZ directions than the main phase. Thus, seismic onsets are mixtures of the main phase and all these different types of disturbances, plus the time depending background noise. This makes polarization analysis of seismic phases more difficult, complicates its interpretation and contributes to the known scatter of polarization results.

In this contribution, a strategy and its theoretical background are presented on how the uncertainties of 3C data analysis results can be reduced and more reliable BAZ and apparent velocity parameters can be estimated, by applying an analysis algorithm consisting of several steps.

6.2.2   The approach

Assuming that the observed onset is either a P-, or an Rg- or an S-onset, one can separate the analysis in four steps:

- At first, the 3C data are rotated in the LQT-coordinate system under the assumption that the onset is a P-phase. If the phase under investigation is really a P-phase, BAZ and INC values must exist for which all energy is concentrated on the L component, while the Q- and T-components are almost zero. But *e.g.*, also an almost horizontally propagating, vertically polarized S-onset will have large vertical amplitudes but small horizontal amplitudes and can therefore be misinterpreted as a P-phase.

- In a second step, the Rg-phase hypothesis is assumed. For Rg-phases, one expects only energy on the L- and Q-components, with slightly larger amplitudes on the Q-component. The T-component should be zero as for P-type onsets.

- The third step is an analysis under the assumption that the onset is an S-phase. In this case, it should be possible to rotate the 3C data for one BAZ and INC value so, that in the L, Q, T system the L component has zero amplitudes and all the energy is concentrated on the Q and T components.

- In a last step, the results found for the different phase types, BAZ and INC combinations are compared and weighted to decide if the observed phase is most probably a P-, an Rg- or an S-phase and which BAZ and incidence angle (*i.e.*, slowness) fits best with this phase identification.

In any case, this approach is based on the assumption that there is only one dominating seismic phase type, which reaches the station from below. Seismic signals coming from above the 3C station (as *e.g.,* recordings by underground installations or of acoustic signals) cannot be correctly analyzed.

6.2.3 The method

At first some basic formulas and definitions are listed:

Z   vertical component of the 3C recording

E   east-west oriented horizontal component of the 3C recording

N   north-south oriented horizontal component of the 3C recording

R   radial component after rotating the horizontal components for a specific BAZ

T   transverse component after rotating the horizontal components for a specific BAZ; identical with the SH component after rotating all three components in the ray oriented LQT-coordinate system by applying a specific BAZ and INC

Q   SV component after rotating all three components in the ray oriented LQT-coordinate system by applying a specific BAZ and INC

L   longitudinal = compressional P-component after rotating all three components in the ray oriented LQT-coordinate system by applying a specific BAZ and INC

BAZ   backazimuth, angle φ measured between North and the direction of the incoming wavefield (onset) at the seismic station

INC   incidence angle α measured between the horizontal plane and the direction of the incoming wavefield (onset) at the seismic station

The relation between the different components is defined as:

$$R = -N * \cos(BAZ) - E * \sin(BAZ)$$
$$T = +N * \sin(BAZ) - E * \cos(BAZ)$$
$$L = +Z * \cos(INC) + R * \sin(INC)$$
$$Q = -Z * \sin(INC) + R * \cos(INC)$$

Squaring these formulas gives:

$R^2 = N^2 * cos^2(BAZ) + 2NE * \cos(BAZ) * \sin(BAZ) + E^2 * \sin^2(BAZ)$
$T^2 = N^2 * \sin^2(BAZ) - 2NE * \cos(BAZ) * \sin(BAZ) + E^2 * \cos^2(BAZ)$
$L^2 = Z^2 * \cos^2(INC) + 2ZR * \cos(INC) * \sin(INC) + R^2 * sin^2(INC)$
$Q^2 = Z^2 * sin^2(INC) - 2ZR * \cos(INC) * \sin(INC) + R^2 * cos^2(INC)$

6.2.4 P-phase inversion

To invert for the best BAZ and INC in the case of a P-phase, the Q- and T-components have to be minimized, which means that

$Q = 0 ; T = 0 ; L = \sqrt{N^2 + E^2 + Z^2} ; R = \sqrt{N^2 + E^2}$
$Q^2 = 0 ; T^2 = 0 ; L^2 = N^2 + E^2 + Z^2 ; R^2 = N^2 + E^2$

First, the BAZ is estimated by solving with a Least-Squares algorithm (LSQ) the following system of n+1 equations

$$\begin{bmatrix} N_1^2 & -2N_1E_1 & E_1^2 \\ \vdots & \vdots & \vdots \\ N_n^2 & -2N_nE_n & E_n^2 \\ 1 & 0 & 1 \end{bmatrix} * \begin{bmatrix} sin^2(BAZ) \\ \sin(BAZ) * \cos(BAZ) \\ cos^2(BAZ) \end{bmatrix} = \begin{bmatrix} 0 \\ \vdots \\ 0 \\ 1 \end{bmatrix}, \qquad \text{(Eq. 1)}$$

for the n samples in the time window that has to be analyzed. The three unknown variables are $sin^2(BAZ)$, $\sin(BAZ) * \cos(BAZ)$ and $cos^2(BAZ)$. The last, (n+1)[th] equation is a side condition to avoid a zero solution and to force that $sin^2(BAZ) + cos^2(BAZ) \equiv 1$. Then, the backazimuth φ is defined as

$\varphi = atan\sqrt{sin^2(BAZ)/cos^2(BAZ)}$ (Eq. 2)

Because of the periodicity of the trigonometric functions, one gets four different solutions:

$$BAZ = \begin{Bmatrix} \varphi \\ 180 + \varphi \end{Bmatrix} \; if \; \sin(BAZ) * \cos(BAZ) \geq 0 \quad \text{(Eq. 3)}$$

$$BAZ = \begin{Bmatrix} 180 - \varphi \\ 360 - \varphi \end{Bmatrix} \; if \; \sin(BAZ) * \cos(BAZ) < 0 \quad \text{(Eq. 4)}$$

Theoretically, the sign of the inverted parameter $\sin(BAZ) * \cos(BAZ)$ is reducing the four into two possible solutions. However, for BAZ values close to the original coordinate axes and higher noise levels, the application of this rule may lead to wrong results at this stage. Using only horizontal components, the ambiguity between the two remaining possibilities cannot be resolved. Therefore, all four possible BAZ values are considered in the following analysis steps.

The LSQ algorithm gives also standard deviations ($\sigma_{sin^2(BAZ)}, \sigma_{cos^2(BAZ)}$) for the unknown variables of Eq. 1. These standard deviations σ_{BAZ} can then be used to calculate the uncertainty of the BAZ estimates by applying standard rules for calculating derivatives and Gauss' law of error propagation:

$$\sigma_\varphi = \sqrt{\frac{\partial \varphi}{\partial \sin^2(BAZ)} * \sigma^2_{\sin^2(BAZ)} + \frac{\partial \varphi}{\partial \cos^2(BAZ)} * \sigma^2_{\cos^2(BAZ)}} \quad =$$

$$\frac{1}{2} * \sqrt{\cot^2(BAZ) * \sigma^2_{\sin^2(BAZ)} + \tan^2(BAZ) * \sigma^2_{\cos^2(BAZ)}} \qquad \text{(Eq. 5)}$$

To invert also for the incidence angle α, a second equation system has to be solved under the condition that the energy on the Q-component should also become minimum when applying the four possible BAZ values to calculate R:

$$\begin{bmatrix} Z_1^2 & -2Z_1R_1 & R_1^2 \\ \vdots & \vdots & \vdots \\ Z_n^2 & -2Z_nR_n & R_n^2 \\ 1 & 0 & 1 \end{bmatrix} * \begin{bmatrix} \sin^2(INC) \\ \sin(INC) * \cos(INC) \\ \cos^2(INC) \end{bmatrix} = \begin{bmatrix} 0 \\ \vdots \\ 0 \\ 1 \end{bmatrix}, \text{(Eq. 6)}$$

As shown for Eq.1, Eq. 6 can be solved for the unknown variables $sin^2(INC)$, $\sin(INC) * \cos(INC)$ and $cos^2(INC)$. The incidence angle α is then defined as:

$$\alpha = atan\sqrt{sin^2(INC)/cos^2(INC)} \qquad \text{(Eq. 7)}$$

The standard deviation σ_α can then be derived in analogy to σ_{BAZ}:

$$\sigma_\alpha = \sqrt{\frac{\partial \alpha}{\partial \sin^2(INC)} * \sigma^2_{\sin^2(INC)} + \frac{\partial \alpha}{\partial \cos^2(INC)} * \sigma^2_{\cos^2(INC)}}$$

$$= \frac{1}{2} * \sqrt{\cot^2(INC) * \sigma^2_{\sin^2(INC)} + \tan^2(INC) * \sigma^2_{\cos^2(INC)}} \qquad \text{(Eq. 8)}$$

There is a trade-off between the sign of $\sin(INC) * \cos(INC)$ and the incidence direction of the seismic phase. At this stage, one has to make the assumption that the seismic phase is reaching the station either from below or above the seismic station. In the algorithm described herein, the assumption is made that seismic waves are coming from below in the case of body waves or horizontally in the case of surface waves. Then, a negative sign of $\sin(INC) * \cos(INC)$ indicates that the phase arrives from the opposite direction (a 180° change) than the applied BAZ, which theoretically solves the 180° ambiguity of Eqs. 3 and 4.

It is well known that seismic stations at the Earth's surface record a mixture of directly arriving and reflected seismic energy. The reflected wavefield can contain P-to-S or S-to-P converted waves, which changes the amplitude ratio between the vertical and horizontal components in a characteristic way and consequently influences the measured incidence angle α, which is therefore called an apparent incidence angle. Following Wiechert (1907) or *e.g.*, Müller (2007), for P-phases the relation between the apparent incidence angle α and the free-surface corrected incidence angle β can be written as

$$a = \arctan\left(\frac{2*\sin(\beta)*\left(\gamma - \sin^2(\beta)\right)^{1/2}}{(\gamma - 2*\sin^2(\beta))} \right).$$

Knowing the seismic velocity ratio $\gamma = (v_P/v_S)^2$ below the 3C station and assuming that α is always positive and v_P is always larger than v_S, one can show that

$$sin^2(\beta) = \frac{\gamma}{2}(1 - cos(\alpha))$$

and

$$\beta = arcsin\left(\frac{v_P}{v_S} * sin(\frac{\alpha}{2})\right). \qquad \text{(Eq. 9)}$$

The uncertainty of β is then

$$\sigma_\beta = (\partial\beta/\delta\alpha) * \sigma_\alpha = \frac{v_P}{2*V_S} * \frac{cos(\alpha/2)}{cos(\beta)} * \sigma_\alpha \qquad \text{(Eq. 10)}$$

By knowing the local P velocity one can also convert the apparent or the free-surface corrected incidence angles into apparent velocities by applying Snell's law

$$v_{app} = \frac{v_P}{sin(inc)} \qquad \text{(Eq. 11)}$$

with an uncertainty of

$$\sigma_{vapp} = v_{app} * tan(inc) * \sigma_{inc} \qquad \text{(Eq. 12)}$$

The corrected incidence angle and the apparent velocity including their uncertainties depend on the seismic velocities below the station. In the real Earth, where seismic velocities change with depth, the velocities to be used are the effective velocities of the uppermost layers, depending on the dominant wavelength of the analyzed seismic phase. Contrary to measurements with a seismic array without topography effects (see *e.g.*, Schweitzer *et al.*, 2012), in the 3C case all incidence angle and apparent velocity measurements become frequency depending.

6.2.5   Rg-phase inversion

Rg-phases can be handled as part of the P-phase case. Eqs. 1 – 2 are also true for Rg-onsets: The best BAZ for Rg-phases minimizes the energy on the T-component. However, Rg-phases have significant energy on the Z- and R-components. In addition, contrary to P type onsets, one can observe a time shift between the Rg-onsets on the Z- and R-components. Therefore, it does not make sense to rotate this phase in an LQT-coordinate system. To test this, R-traces are calculated for all four possible BAZ values and then cross-correlated with the original Z-component. Another possibility would be to compare the two traces after a Hilbert transform of one of them. Whenever a significant time shift between the onsets on both components is observed, this is taken as a strong indication for an Rg-onset, since such time shifts are not observable for P or S-phases.

6.2.6   S-phase inversion

In the case of an S-phase, one can only use the rule that in the LQT-system the L-component should show no energy, all seismic energy being polarized in a plane perpendicular to the propagation direction. The distribution of energy between the Q- and T-components mostly depends on the radiation pattern of SV and SH at the seismic source and cannot be used here as an analysis criterion.

In a first step, the best fitting BAZ and INC are inverted for, to minimize the L-component. Once again some definitions:

$U \equiv N^2 + E^2 + Z^2 \equiv T^2 + Q^2$ (Eq. 13)

From $L = +Z * \cos(INC) + R * \sin(INC) = 0$ follows that $Z = -R * \tan(INC)$ and $R = -Z * \tan(INC)$. Using these relations and $Q^2 = R^2 + Z^2$ one can show that

$$Q^2 = Z^2 * \frac{1}{sin^2(INC)}. \quad \text{(Eq. 14)}$$

Setting the definition of $T^2 = N^2 * \sin^2(BAZ) + 2NE * \cos(BAZ) * \sin(BAZ) + E^2 * \cos^2(BAZ)$ and of Q^2 from Eq. 14 in Eq. 13 one gets:

$$N^2 * \sin^2(BAZ) - 2NE * \cos(BAZ) * \sin(BAZ) + E^2 * \cos^2(BAZ) + \frac{Z^2}{\sin^2(INC)} = U$$

$$\frac{N^2 * \sin^2(BAZ)}{U} - \frac{2NE * \cos(BAZ) * \sin(BAZ)}{U} + \frac{E^2 * \cos^2(BAZ)}{U} + \frac{Z^2}{U * \sin^2(INC)} = 1$$

This can be solved again with the LSQ algorithm as in the P-phase case, with the only difference that there are now four unknowns:

$$\begin{bmatrix} \frac{N_1^2}{U} & \frac{-2N_1 E_1}{U} & \frac{E_1^2}{U} & \frac{Z_1^2}{U} \\ \vdots & \vdots & \vdots & \vdots \\ \frac{N_n^2}{U} & \frac{-2N_n E_n}{U} & \frac{E_n^2}{U} & \frac{Z_n^2}{U} \\ 1 & 0 & 1 & 0 \end{bmatrix} * \begin{bmatrix} \sin^2(BAZ) \\ \sin(BAZ) * \cos(BAZ) \\ \cos^2(BAZ) \\ 1/\sin^2(INC) \end{bmatrix} = \begin{bmatrix} 1 \\ \vdots \\ 1 \\ 1 \end{bmatrix}, \quad \text{(Eq. 15)}$$

As for the P-phase case, the backazimuth φ can be determined by applying Eq. 2 and for its uncertainty σ_φ Eq. 5 can be used:

$$\varphi = atan\sqrt{\sin^2(BAZ)/\cos^2(BAZ)} \quad \text{(Eq. 15)}$$

$$\sigma_\varphi = \frac{1}{2} * \sqrt{\cot^2(BAZ) * \sigma^2_{\sin^2(BAZ)} + \tan^2(BAZ) * \sigma^2_{\cos^2(BAZ)}} \quad \text{(Eq. 16)}$$

With the fourth modeled parameter $a = 1/\sin^2(INC)$ the incidence angle α can be calculated:

$$\alpha = \arcsin\left(\sqrt{\frac{1}{a}}\right), \quad \text{(Eq. 17)}$$

and the uncertainty σ_α is defined as

$$\sigma_\alpha = \frac{\partial \alpha}{\partial a} * \sigma_{1/\sin^2(INC)} = \frac{1}{2a} * \tan(\alpha) * \sigma_{1/\sin^2(INC)} \quad \text{(Eq. 18)}$$

To obtain the apparent velocity of the S-onset one has to apply again Snell's law, now with the local S velocity v_S as input parameter:

$$v_{app} = \frac{v_S}{\sin(INC)} \quad \text{(Eq. 19)}$$

The uncertainty of the apparent S-velocity becomes

$$\sigma_{vapp} = v_{app} * \tan(\alpha) * \sigma_\alpha . \quad \text{(Eq.20)}$$

The S-phase incidence angle is also influenced by the free-surface effect, but contrary to the case of P-phases there exists no uniform theoretical solution to correct for this. Therefore, incidence angles of S-phases and consequently their apparent velocities are not identical with other measuring methods like *e.g.*, array-based fk-results.

Also for S-phases exists the ambiguity between the different BAZ values due to the properties of the trigonometric functions. This problem can only be solved in a later stage. Tests made for numerous examples showed that inverting for both parameters (BAZ and INC) in one step does not always give the best solution. Therefore, two additional inversions are added to validate the found results.

1) At first the obtained BAZ values are used to calculate T- and R-traces and then an inversion is performed to find the best INC values. This is done in analogy to Eq. 6, but now for a minimized L-component:

$$\begin{bmatrix} R_1^2 & 2R_1Z_1 & Z_1^2 \\ \vdots & \vdots & \vdots \\ R_n^2 & 2R_nZ_n & Z_n^2 \\ 1 & 0 & 1 \end{bmatrix} * \begin{bmatrix} sin^2(INC) \\ sin(INC)*\cos(INC) \\ cos^2(INC) \end{bmatrix} = \begin{bmatrix} 0 \\ \vdots \\ 0 \\ 1 \end{bmatrix}, \quad \text{(Eq. 21)}$$

The incidence angle α can then again be calculated with Eq. 7 and its uncertainty with Eq. 8. For obtaining the corresponding apparent velocities and their uncertainties one can apply Eqs. 19 and 20.

2) Then, in a second additional inversion the obtained INC value from Eq. 17 is applied and the corresponding best BAZ values are calculated:

When setting $R = -Z/\tan(INC)$ in the definition of the R^2 one gets

$$R^2 = E^2 * sin^2(BAZ) + 2NE * \cos(BAZ) * \sin(BAZ) + N^2 * cos^2(BAZ) = \frac{Z^2}{\tan^2(INC)}$$

and one can define the equation system:

$$\begin{bmatrix} \frac{E_1^2*\tan^2(INC)}{Z^2} & \frac{2E_1N_1*\tan^2(INC)}{Z^2} & \frac{N_1^2*\tan^2(INC)}{Z^2} \\ \vdots & \vdots & \vdots \\ \frac{E_n^2*\tan^2(INC)}{Z^2} & \frac{2E_nN_n*\tan^2(INC)}{Z^2} & \frac{N_n^2*\tan^2(INC)}{Z^2} \\ 1 & 0 & 1 \end{bmatrix} * \begin{bmatrix} sin^2(BAZ) \\ sin(BAZ)*\cos(BAZ) \\ cos^2(BAZ) \end{bmatrix} = \begin{bmatrix} 1 \\ \vdots \\ 1 \\ 1 \end{bmatrix}, \text{(Eq. 22)}$$

For solutions of the BAZ values φ one can again use Eq. 2 and for their uncertainties σ_φ Eq. 5. The results are all four new possible BAZ values because of the known ambiguity of the trigonometric functions.

6.2.7　Evaluation of the solutions and selection of the best possible phase estimate

The final step in this analysis scheme for seismic onsets observed with 3C stations is an evaluation of the different solutions and deciding on the most probable phase type, BAZ and INC (*i.e.*, apparent velocity) of the observation. This is done in two steps. In a first step, the best solution for each phase type is selected and in a second step, the results for three possible phase types are compared with

each other. To evaluate the different solutions, the original 3C traces are rotated into R-,T-, L- and Q-traces. Then, for each component C (*i.e.*, for Z, N, E, R, T, L and Q) the vector sums sZ, sN, sE, sR, sT, sL and sQ are calculated over all samples i by using the formula $sC = \sqrt{\sum_i sample_i^2}$. In addition, normalized relations between some of the components ($C_1 C_2$) are calculated (*i.e.*, for RZ, RL, QZ, QR and ZL). For each of the relations between two components, the following formula is used $C_1 C_2 = \frac{\sum_i sample_{c1}*sample_{c2}}{sC_1*sC_2}$.

Also the following sums are used during the different evaluation steps:

$$sH = \sqrt{sQ^2 + sT^2}; \quad sH0 = \sqrt{sE^2 + sN^2} \equiv \sqrt{sT^2 + sR^2};$$
$$SUM = \sqrt{sZ^2 + sN^2 + sE^2}; \quad sRG = \sqrt{sZ^2 + sR^2}; \quad QT = sH/sH0$$

All these values are used to express phase type specific characteristics, as specified in the next sections. However, the applied relations are strictly true only for ideal onsets. In the following decisions the assumption is that the joint application of many different phase type specific characteristics will give the most plausible analysis result.

6.2.7.1   The best P-phase solution

Assuming the phase is a P-phase, eight different solutions were found: four solutions for the BAZ and for each BAZ value one solution for an INC. For observed amplitudes on the different traces, an ideal P-phase should show the following relations between the above calculated parameters:

sL > sZ ; sL > sQ; sL > sT ; sL > sH ; sL > sH0 ;
sR > sT ; sR > sQ ; sH0 > sH ; sL = SUM ; and RZ > 0

Taking these rules in a product of factors one can calculate the following decision factor:

$$F_P = \left| RZ * ZL * RL * \frac{RZ*sL*sL*sL*sR*sR*sL*sL*sH0}{QZ*sZ*sQ*sT*sT*sQ*sH0*sH*sH} \right| = \left| \frac{RZ^2*ZL*RL*sL^5*sR^2}{QZ*sZ*sQ^2*sT^2*sH^2} \right| \qquad \text{(Eq. 23)}$$

All BAZ/INC combinations for which RZ < 0 & sH > 0.2 * sL or sH > 1.05 * sH0 or sL < 0.95 * sZ or sT > sR & sH0 > 0.2 * sL are directly rejected. Then, the P-phase with the largest value of F_p defines the most probable BAZ and INC.

6.2.7.2   The best Rg-phase solution

The possible Rg-phase has four possible BAZ solutions. Being a surface wave, Rg has no values for INC, *i.e.*, the rotation from Z- and R- into Q-and L-components does not make any sense. However, time shifts found between the R- and the Z-components after the rotation of the original horizontal N- and E-components into R- and T-components are taken in account when calculating the above mentioned vector sums and trace relations. The following rules can be used to find the best parameters of the Rg-onset:

sZ > sT ; sR > sT; sRG > sT; sH0 > sT ; sRG > sZ ; sRG > sR ; and RZ > 0

Taking these rules as in a product of factors one can calculate the following decision factor:

$$F_{Rg} = \left| \frac{RZ*sR*sZ*sRG*sH0*sRG*sRG}{sT*sT*sT*sT*sZ*sR} \right| = \left| \frac{RZ*sRG^3*sH0}{sT^4} \right| \qquad \text{(Eq. 24)}$$

All solutions for which RZ < -0.1 or sT > sZ or sT > sR are rejected. Then the parameters for BAZ and INC are chosen, which result in the largest value of F_{Rg}.

6.2.7.3   The best S-phase solution

From the three inversions for S-phases described in Section 6.2.6, one gets 12 different BAZ/INC combinations: four different BAZ values and one INC value from the first inversion, four different INC values from the second solution and four different BAZ values from the last inversion. The S-phase related rules are as following:

RQ > RZ ; sH > sH0 ; sH > sZ ; sH > sL ; sH > sR ; sH > sT ; sH0 > sZ ; sZ > sL ; and RZ < 0

Then one can define the following decision factor F_S for choosing the best S-phase onset:

$$F_S = \left| \frac{RQ*sH*sH*sH*sH*sH*sH0*sZ}{RZ*sH0*sZ*sL*sR*sT*sZ*sL} \right| = \left| \frac{RQ*sH^5}{RZ*sL^2*sR*sT*sZ} \right| \qquad \text{(Eq. 25)}$$

All combinations for which RZ > 0.5 or sL > 1.05*sZ & sZ > 0.3*sH0 or sH < 0.95 *sH0 are directly rejected. Then the parameters for BAZ and INC are chosen, which result in the largest value of F_S.

6.2.7.4   Choosing the right phase

To decide which one of the three phase types is the most likely one, a parameter D is calculated which is representative of the seismic energy of the different phase types. To avoid results biased by the chosen contributing factors, it is important that the parameter D consists for all three phase types of the same number of single factors with similar value ranges.

The parameters D are defined for the different phases as:

$$D_P = \left| \frac{ZL_P}{QT_P} \right| * \frac{sZ^3*sL_P^{15}}{sN^2*sE^2*sH_P*sH0_P*sQ_P{}^2*sT_P{}^2*sRG_P*sL_S*sL_{Rg}*sH_S*sH_{Rg}*sRG_S*sRG_{Rg}*SUM} \qquad \text{(Eq. 26)}$$

$$D_S = \left| \frac{QT_S}{ZL_S} \right| * \frac{sH0^3*sH_S^{15}}{sZ^2*sN*sE*sL_S{}^2*sQ_S{}^2*sT_S{}^2*sRG_S*sL_P*sL_{Rg}*sH_P*sH_{Rg}*sRG_P*sRG_{Rg}*SUM} \qquad \text{(Eq. 27)}$$

$$D_{Rg} = \left| \frac{RZ_{Rg}}{sT_{Rg}} \right| * \frac{sZ^2*sR_{Rg}^3*sRG_{Rg}^{13}}{sN^3*sE^3*sT_{Rg}{}^3*sH0^2*sL_P*sL_S*sH_P*sH_S*sRG_P*sRG_S*SUM} \qquad \text{(Eq. 28)}$$

Then, the phase type with the largest value of D is assumed to fit best with the observed onset and is chosen as the result of the 3C onset analysis.

6.2.8   Examples

From the formulas derived above it becomes clear that to decide on the phase type and best onset parameters BAZ and INC, the signal amplitudes should be clearly visible above the background noise level. In particular for components with theoretically small amplitudes, a relatively high noise level can easily result in wrong analysis results. In the following, some examples are shown for unequally successful analysis results and phase types. In all cases the algorithm decided about the phase type

by applying Eqs. 26 – 28 and reported the best fitting BAZ and INC values by applying Eqs. 23 – 25.
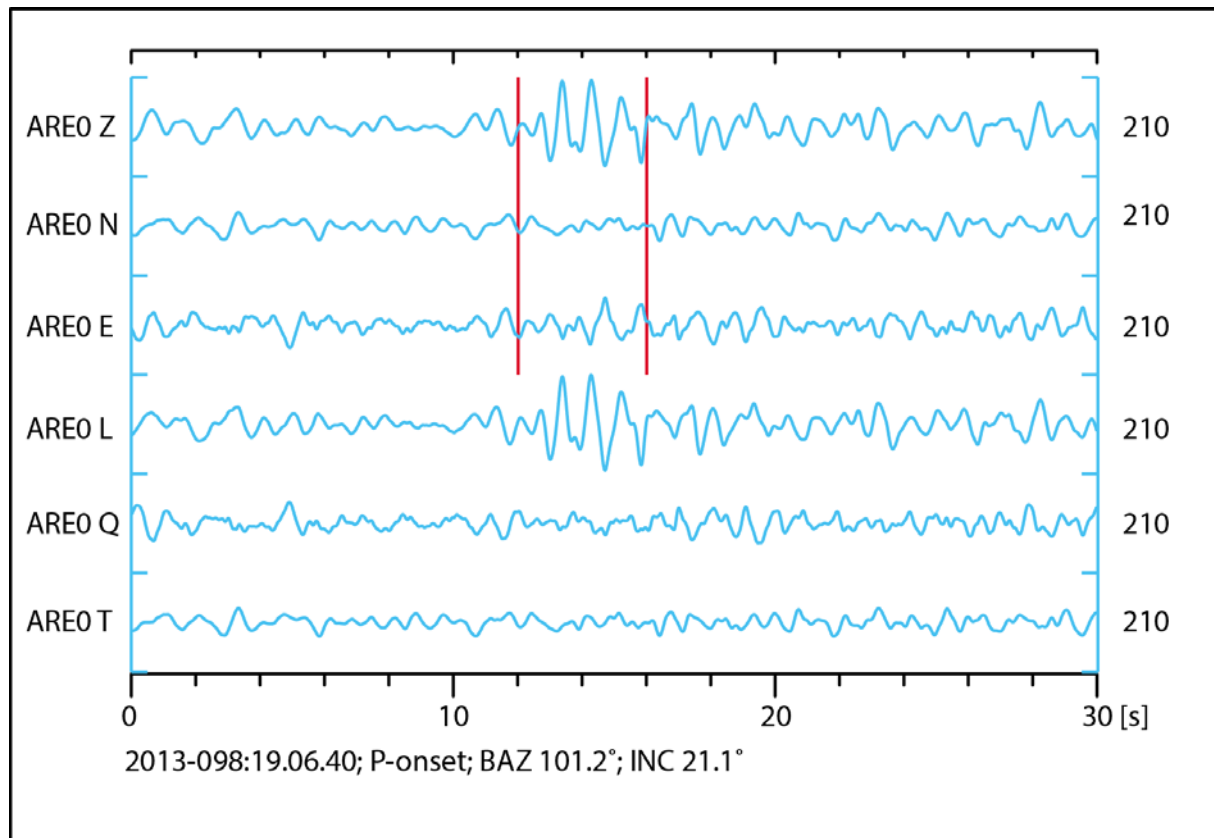

*Fig. 6.2.1   Data (bandpass filtered 1 – 4 Hz) of a teleseismic P-onset observed at the ARCES 3C-site
ARE0. The time window used for the 3C analysis is marked (red lines) and the maximum
amplitude is given on the right. The three top traces show the original 3C (ZNE) and the
three bottom traces the LQT-rotated data. For further details see text.*

Fig. 6.2.1 shows the P-onset of an mb 5.2 event (IDC REB hypocenter: Lat -6.99°, Lon 106.15°, depth
47 km, source time 8 April 2013, 18:53:44) recorded with the 3C broadband station of the ARCES
array (ARE0) at a distance of 93.24°. The maximum signal-to-noise ratio (SNR) on the Z-component is
5.65, on E 2.60 and on the N-component only 1.84. The data are bandpass filtered for the best SNR
between 1 and 4 Hz. The 3C analysis of the onset gave BAZ = 81.54° and INC = 21.1°, which, after
applying the free surface correction, corresponds to an apparent velocity of 17.3 km/s. The
theoretical values based on the REB location are BAZ = 101.18° and 24 km/s for the apparent
velocity. The ARCES array analysis of all vertical components for the same time window gives BAZ =
97.10° and 22.5 km/s for the apparent velocity, which is much closer to the theoretically expected
values. The discrepancies between theory and 3C analysis results are probably influenced by the low
SNR values on the two horizontal components.

Fig. 6.2.2 shows the ARE0 recordings of a mining event at Kiruna (13 April 2013, 23:49:50). The
applied bandpass filter was between 1.5 and 4.0 Hz and the 3C analysis tool was used for the clearly
visible Sg-onset. The 3C analysis result was BAZ = 214.9° and INC = 62.9°, corresponding to an
apparent velocity of 3.6 km/s. This fits with the theoretical values BAZ = 231.2° and an apparent
velocity of 3.9 km/s. An fk-analysis of the same data, but using the vertical components of the whole
ARCES array, confirms this result by measuring 225.4° for the BAZ and 4.3 km/s for the apparent

velocity. After rotation, the L-component shows clearly time-varying amplitudes which cannot be explained as a single S-type polarized onset. Choosing another time window for the 3C analysis may result in different, eventually even totally wrong results, depending on the scattered energy on the Z-component.
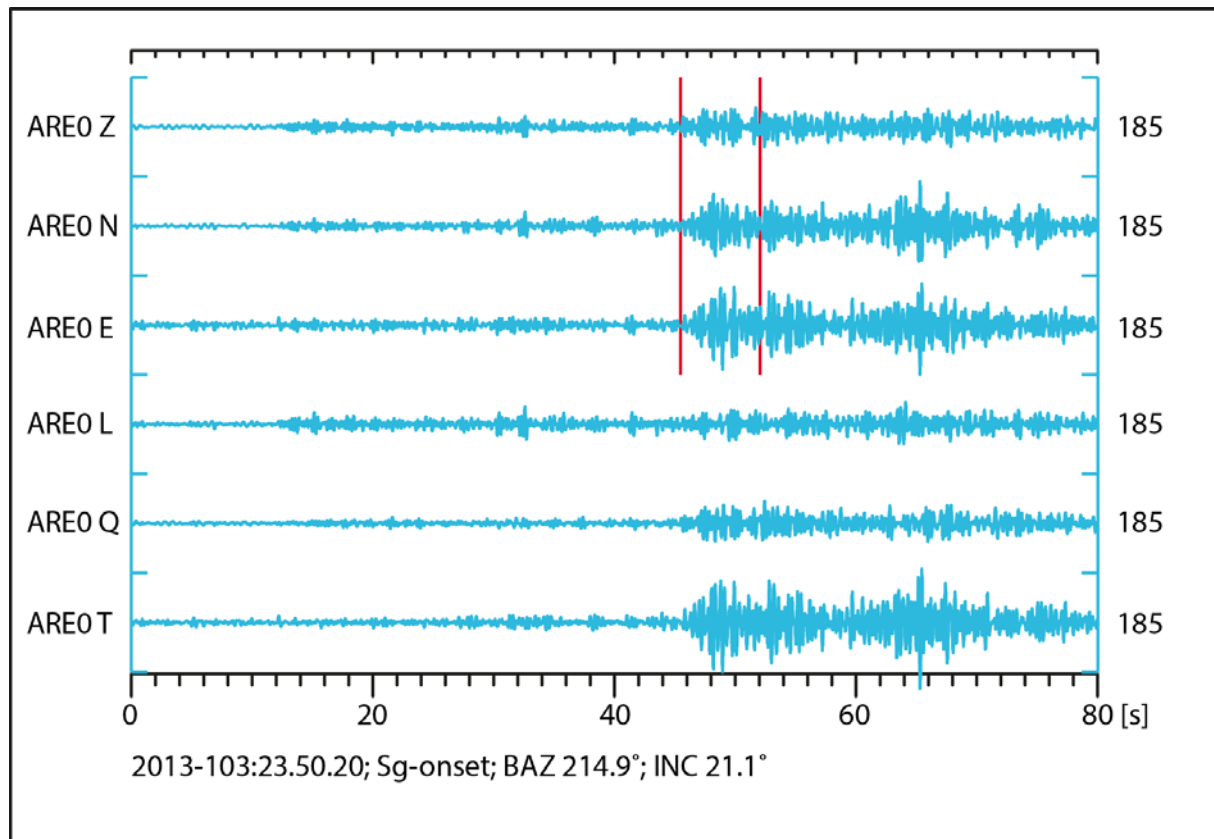

Fig. 6.2.2   Data (bandpass filtered 1.5 – 4 Hz) of a regional Sg-onset observed at the ARCES 3C-site ARE0. The time window used for the 3C analysis is marked (red lines) and the maximum amplitude is given on the right. The three top traces show the original 3C (ZNE) and the three bottom traces the LQT-rotated data. For further details see text.

Fig. 6.2.3 shows an icequake recorded very near to the center element SPA0 of the SPITS array on Svalbard (epicentral distance ~10 km), here bandpass filtered between 1.5 and 4 Hz. The 3C analysis of the P-onset (red lines) gives a BAZ of 121.9°, which is confirmed by an fk-analysis applied for the full array (BAZ = 122.6°). The INC value of 27.8° results in an apparent velocity of 12.5 km/s, which is quite high with respect to the fk-result of 4.7 km/s. However, the 3C result for the apparent velocity was calculated using some standard values for P- and S-velocities without taking in account the local velocity structure. The duration of the event is quite short; the S-onset is arriving only 2 s after the P-onset. Already the original Z-component shows that there is significant P-energy arriving during the S-phase. This is mostly a continuation of the P-phase and its coda, but also the effect of the elliptical polarization of SV-energy due to interaction with the free surface. Therefore, it is no surprise that a 3C analysis fails when analyzing a short time window like the one indicated with the dashed magenta lines around the largest S-onset. When using a longer time window (green lines) and analyzing the whole S-phase group one gets BAZ = 116.9 and INC = 64.6, which corresponds to an apparent velocity of 3.3 km/s. The full array fk-analysis for the same time window gives BAZ = 123.5° and an apparent

velocity of 2.3 km/s. That the apparent velocity result for the 3C analysis is different from the fk-result can be explained again with the incorrectly modeled local velocity structure.
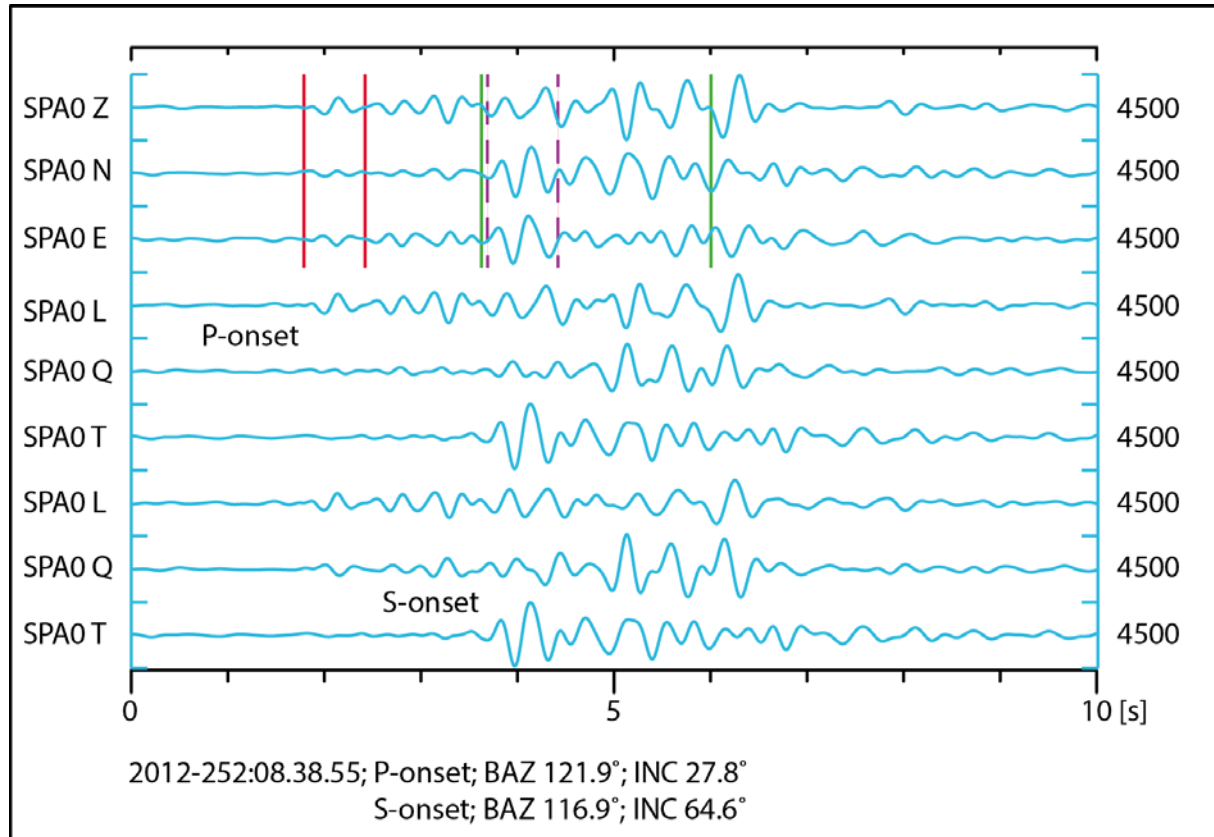

Fig. 6.2.3   Data (bandpass filtered 1.5 – 4 Hz) of an icequake observed at the SPITS 3C-site SPA0. The time window used for the 3C analysis of the P-onset is marked with red lines, of the S-onset with green lines and the amplitude is given on the right. The dashed magenta lines indicate another possible time window to analyze the S-onset. The three top traces show the original 3C (ZNE), the three middle traces the LQT, resulting from rotation using the P-phase parameters, and the three bottom traces the LQT data, resulting from rotation using the S-phase parameters. For further details see text.

Fig. 6.2.4 shows the same icequake as Fig. 6.2.3, but now bandbpass filtered between 0.8 and 2.5 Hz. The figure shows a clear Rg-onset on the Z-component, which is typical for events with hypocenters close to the Earth's surface, as *e.g.*, also for icequakes on Svalbard. The figure shows also that the Rg-onset is not so clearly visible on the original horizontal N- and E-components due to still arriving energy of the S-phase and its coda. Here, the correct position and the length of the data window to be analyzed are as critical as in the case of the S-onset. The 3C-analysis of the marked time window correctly identifies the onset as an Rg-onset and finds a BAZ of 121.7°, which is very close to the value achieved by an fk-analysis of all data from the whole array (BAZ 128.25°, apparent velocity 1.63 km/s). The 3C-analysis cannot measure the apparent velocity of a surface wave (here Rg). After rotating the N- and E-components into R- and T-components, the Rg-onset becomes visible on the R-component. The T-component is dominated by S-energy, which already had the largest S-amplitudes after rotating in the LQT-system with S-onset parameters (compare with Fig. 6.2.3). As typical for Rg onsets, a time shift of about ¼ of the dominating signal period is observed between the phase onset on the Z- and the R-component (see the green arrows).
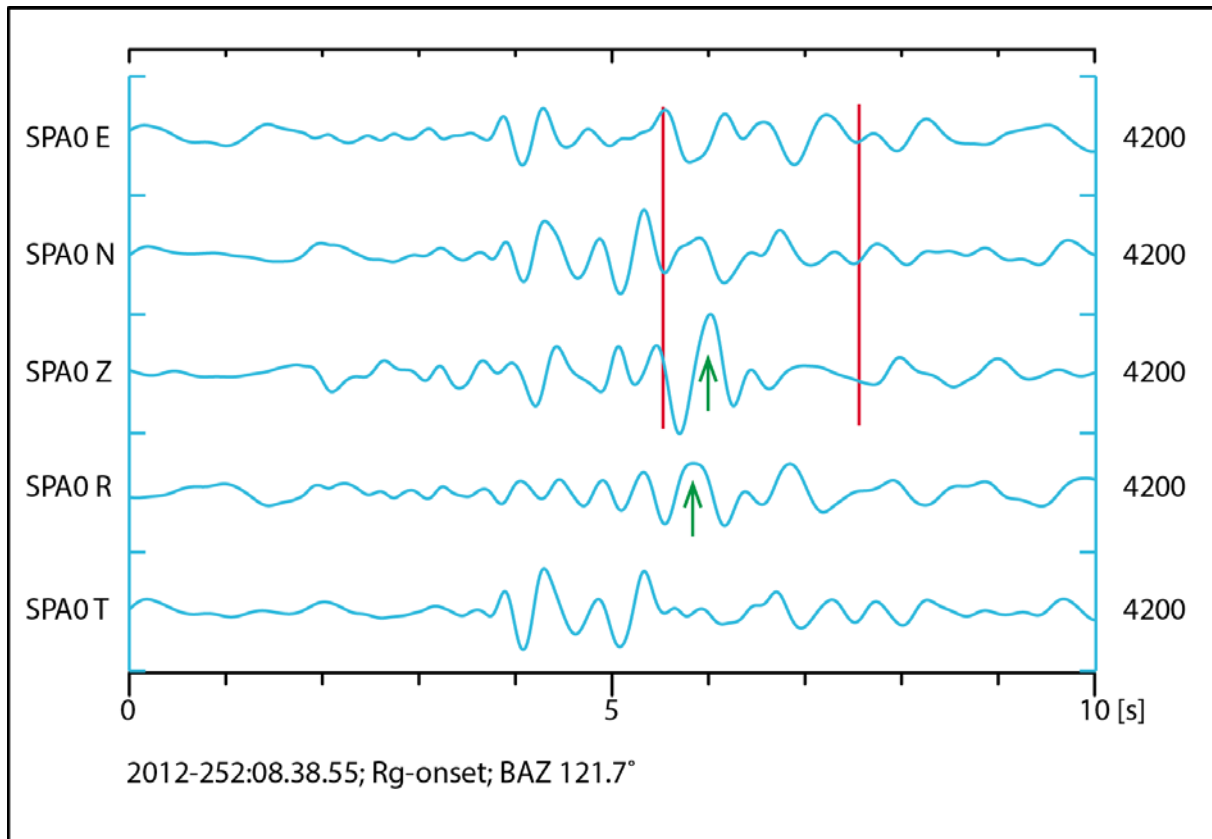
Fig. 6.2.4   As Fig. 6.2.3. The data are now filtered between 0.8 and 2.5 Hz and the red lines show the time window used for the 3C-analysis of the Rg-onset. The three time series on top show the original 3C (ZNE) traces and the two on bottom the R- and T-traces after rotation with the BAZ of the Rg onset. For further details see text.

6.2.9   Conclusions

An algorithm to analyze 3C data for phase type, BAZ and INC has been developed, which works fine for ideal data. Reliable results can be achieved also in the case of more noisy and difficult data, as presented in the examples discussed above. However, a systematic study of a large amount of 3C data is missing. For this it is planned to use data from one of NORSAR's arrays and analyze data from array sites with 3C recordings with the tool presented herein. In parallel, a conventional fk-analysis for data from the whole array will be performed as reference. As already seen from the examples shown above, the SNR of the onsets on the different 3C recordings will be particularly critical for the results and it will be interesting to find the SNR-threshold and/or other limits for reliable results from an automated 3C-analysis tool.

J. Schweitzer

References

Müller, G. (2007). Theory of elastic waves. GeoForschungsZentrum Potsdam, Scientific Technical Report STR 07/03, DOI: 10.2312/GFZ.b103-0737, p. 81-84.

Schweitzer, J., J. Fyen, S. Mykkeltveit, S. J. Gibbons, M. Pirli, D. Kühn and T. Kværna (2012). Seismic Arrays. In: P. Bormann (ed.) (2012), New Manual of Seismological Observatory Practice (NMSOP-2). 2nd (revised) edition, Potsdam: Deutsches GeoForschungsZentrum GFZ., http://ebooks.gfz-potsdam.de/pubman/item/escidoc:43213:7; doi:10.2312/GFZ.NMSOP-2_ch9; 80 pp.

Wiechert, E. (1907). Über Erdbebenwellen. Theoretisches über die Ausbreitung der Erdbebenwellen. Nachrichten von der Königlichen Gesellschaft der Wissenschaften zu Göttingen, Mathematisch-physikalische Klasse, 413-529.

6.3 The Ural Mountains Event on 24 December 2012

6.3.1 Introduction

NORSAR, the Kola Regional Seismological Centre (KRSC, Apatity, Russia) and the Institute of Ecological Problems of the North, Ural Branch of the Russian Academy of Sciences (IEPN UB RAS, Arkhangelsk, Russia) have recently signed a cooperative agreement on scientific cooperation in seismology and infrasound research. Within this agreement we have shared data segments from a newly established seismic station in Amderma (AMD[2]), northwest Russia deployed by IEPN UB RAS in November 2011 (see Fig. 6.3.1).

During the time period 1993-1999 another seismic station in Amderma (AMD[1]) was operated by KRSC at a slightly different location (see Fig. 6.3.2). During this time period, the AMD[1] station recorded a number of interesting events in the Novaya Zemlya - northwest Russia region, among them the well-known events in the Kara Sea on 16 August 1997 (Kremenetskaya and Asming, 1998; Ringdal et al., 2002; Gibbons and Ringdal, 2006; Schweitzer and Kennett, 2002, 2007).

As seen from Fig. 6.3.1, NORSAR's regional monitoring system of regional arrays has for the time period 1990-2013 detected only a small number of events in the Barents/Kara Sea region. An even smaller number of events from this low-seismicity area are reported in the ISC bulletin. However, because of the large hydrocarbon exploration activity in the region and its proximity to the former Novaya Zemlya nuclear test site, seismic events occurring in the area are of high interest to the seismological community.

The newly established station AMD[2], consisting of a Güralp CMG-40-T-1 seismometer and a Geosig GSR-24 digitizer sampling at 50 Hz, is expected to contribute significantly to improving the seismic event monitoring of this region. The station is installed at the premises of the Hydrometeorological Center on a concrete pedestal in a former bomb shelter.

The m_b 3.8 event on 24 December 2012 in the Ural Mountains was one of the first larger events within regional distances recorded at this station. The event was located approximately 100 km south of the city of Vorkuta, on the territory of the Republic of Komi. Location and magnitude estimates of this events reported by different agencies are given in Table 6.3.1.
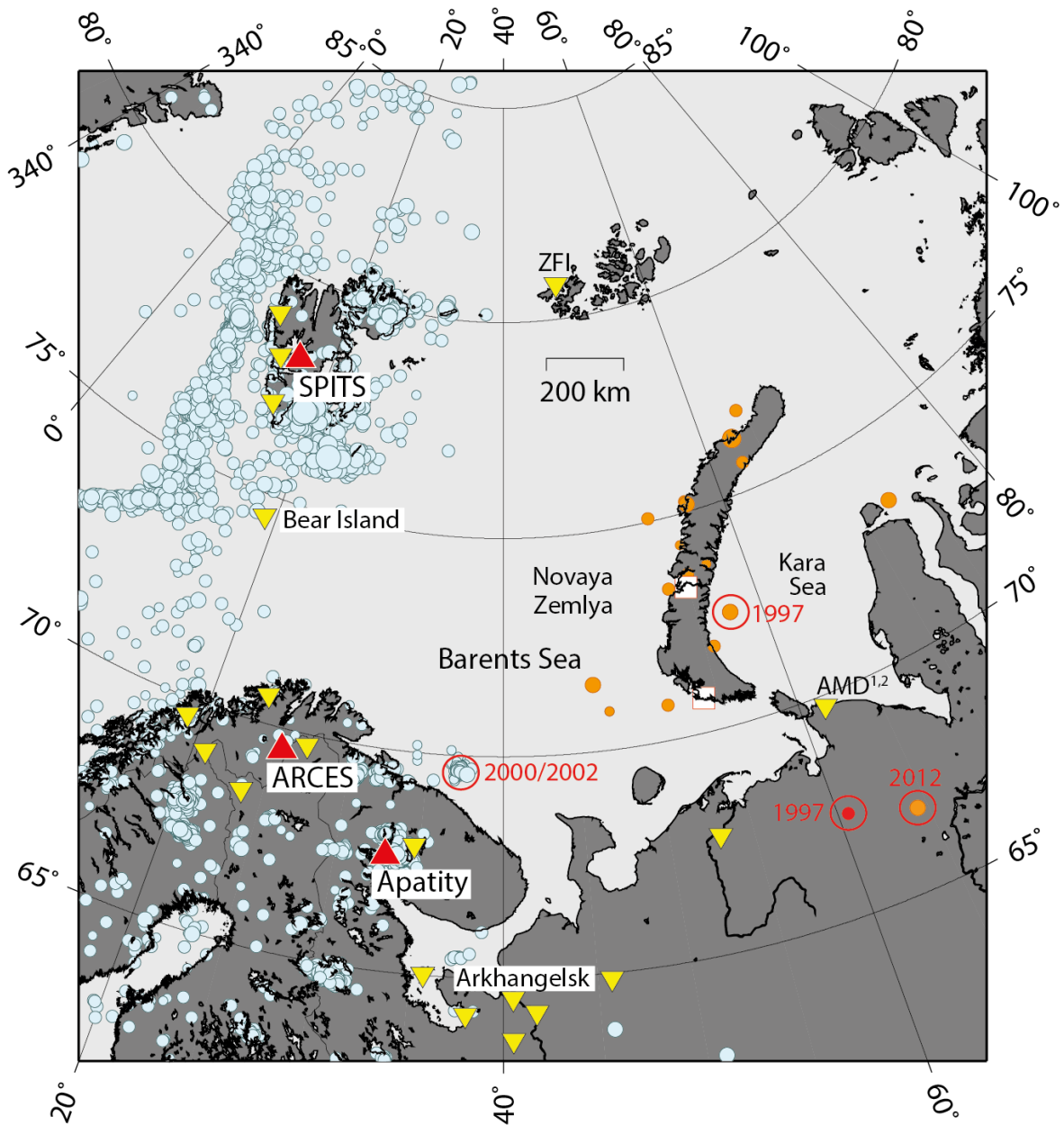
Fig. 6.3.1   *The map shows locations of seismic events (orange dots) in and near Novaya Zemlya that have been detected by the NORSAR regional monitoring system since the Soviet moratorium on nuclear explosions began in 1990. Many of these events have not been reported by any other agency. The blue dots represent other seismic events (mostly earthquakes and mining explosions) that have occurred in the region during the same time interval. Key seismic arrays (red triangles) and three-component stations (yellow triangles) in northern Norway, Finland and northwest Russia are also shown on the map. Events analyzed in this study are highlighted by red circles and the year in which they occurred. The 1997 event located south of Amderma (AMD), marked by a red symbol, was detected at that station only. The former nuclear test sites at Novaya Zemlya are marked with white squares.*

*Fig. 6.3.2
Locations of the two seismic stations deployed in Amderma, northwest Russia, by KRSC, Apatity (AMD[1], 1993-1999) and IEPN UB RAS, Arkhangelsk (AMD[2], November 2011 ->). The distance between the two stations is about 2 km.*

Agency	Origin Time	Lat	Lon	Depth	Mag
Alert Survey GS RAS [www.ceme.gsras.ru]	06:22:39.9	66.52	63.77	20	m_b=4.0
ISC / IDC [www.isc.ac.uk]	06:22:36.8	66.81	64.40	0f	m_b=3.8
ORFEUS [www.seismicportal.eu]	06:22:34.0	66.94	64.49	2	m_b=3.9
Arkhangelsk seismic network	06:22:39.1	66.47	64.73	10	M_L=3.8
NORSAR [www.norsardata.no]	06:22:39.1	66.94	63.95	0f	m_b=4.5

Table 6.3.1   Location and magnitude estimates of the 24 December 2012 Ural Mountains event reported by different agencies.
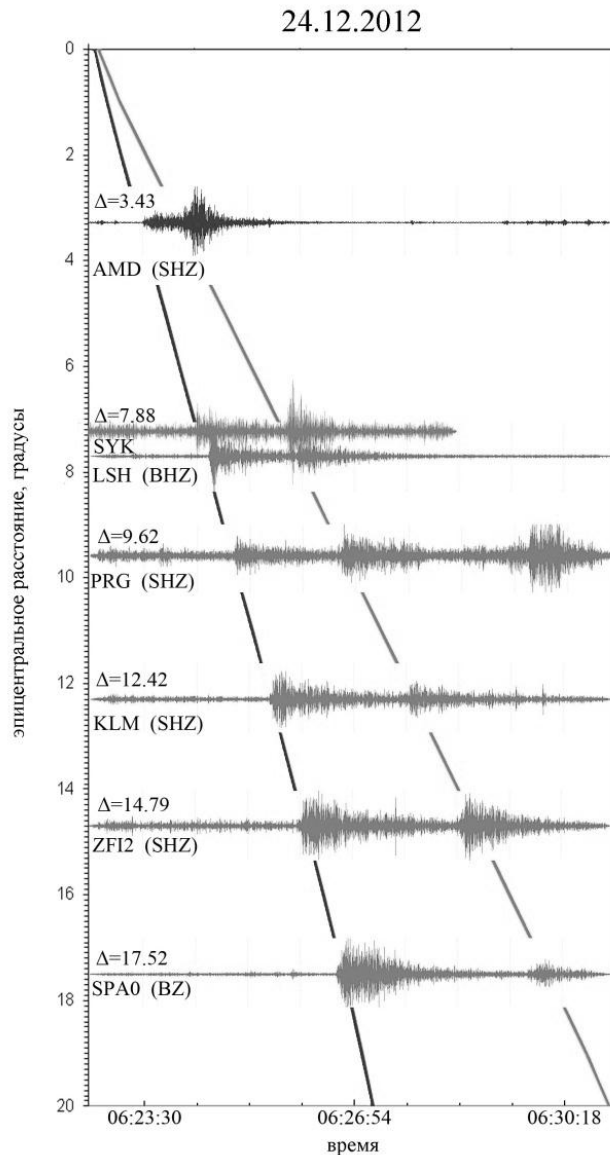
Fig. 6.3.3
Seismogram section of the 24 December 2012 Ural Mountains event as observed at seismic stations on mainland Russia (Arkhangelsk network + Syktyvkar (SYK)), Franz Josef Land (ZFI2) and Spitsbergen (SPA0). The vertical distance axis is given in degrees.

In order to assess the data quality and performance of the new AMD[2] station, we compare the characteristics of the 24 December 2012 event with events recorded at the previous AMD[1] station, operated by KRSC. In addition, we compare the Amderma recordings with ARCES recordings of underwater explosions associated with the Kursk accident in year 2000 and the demolishing of the Kursk wreckage in 2002. The list of events and corresponding recording stations are given in Table 6.3.2.

Date	Origin Time	Lat.	Lon.	Mag.	Station	Dist. (km)	Back-azimuth	Event type
2012/12/24	06:22:37	66.8	64.4	3.8	AMD[2]	347	160	Most likely earthquake
1997/08/16	02:11:00	72.43	57.57	3.5	AMD[1]	334	336	Most likely earthquake
1997/01/31	04:23:53	67.3	60.7	2.5	AMD[1]	275	189	Most likely mine blast
2000/08/12	07:30:42	69.59	37.41	3.5	ARCES	463	84	Underwater explosion
2002/09/08	17:16:28	69.59	37.41	2.8	ARCES	463	84	Underwater explosion

*Table 6.3.2   List of analyzed events and the corresponding recording stations.
Station AMD[2] is operated by IEPN UB RAS, Arkhangelsk, Russia.
Station AM1[2] was operated by KRSC, Apatity, Russia.*

6.3.2   Seismograms and spectra

We show in Fig. 6.3.4 seismograms and ground velocity spectra of the 24 December 2012 event recorded at the new AMD[2] station. The spectra of the P-phase (red) and the S-phase (green) are calculated from the vertical component trace, whereas the blue-colored S-phase spectrum is calculated from the horizontally rotated transverse component. A 30 second time window, starting at the phase arrival time is used as the basis for spectral estimation. The noise spectrum (black) is estimated from the vertical component channel using a 30 second time window preceding the P-phase. For comparison we show the noise spectrum preceding the P-phase from the 16 August 1997 event in the Kara Sea, observed at the previous AMD[1] station operated by KRSC, Apatity.

We notice from the seismograms of Fig. 6.3.4 that both the S-phase and the P-coda amplitudes are about a factor of two larger on the horizontal components as compared with the vertical component. The P-coda energy increases gradually on all components during the first 20 seconds after the P onset. From the spectra we observe that the amplitude of the S-phase, as observed on the transverse horizontal component, is more than a factor 10 larger than for the P-phase, observed on the vertical component, for the wide frequency band 0.8 – 8 Hz. We also observe that the previous AMD[1] station had a significantly lower noise level at high frequencies at the time of the 16 August 1997 Kara Sea event as compared with the noise observed at the new AMD[2] station of 24 December 2012. The AMD[1] station was located at a relatively quiet place in an abandoned mine. For frequencies below 3 Hz, the situation is opposite, and the new AMD[2] station shows the lowest noise level. This may be explained by microseisms caused by ocean waves in the open, ice-free Barents and Kara Seas during the Arctic summer.
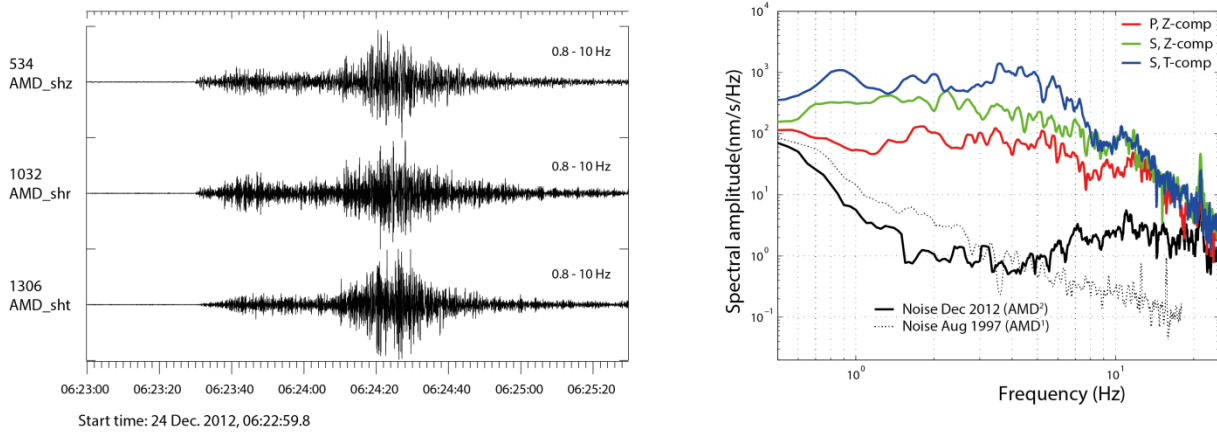
Start time: 24 Dec. 2012, 06:22:59.8

Fig. 6.3.4   The left-hand panel shows recordings at the new AMD[2] station (operated by IEPN UB RAS) of the event on 24 December 2012. The station-event distance is estimated at 347 km. The upper trace shows the vertical component, whereas the two lower traces show the rotated horizontal components (radial and transverse). The data are bandpass filtered between 0.8 and 10 Hz. The right-hand panel shows noise, P- and S-phase ground velocity spectra. The black dotted line shows the noise spectrum preceding the P-phase from 1997 Kara Sea event, observed at the AMD[1] station operated by KRSC.

Fig. 6.3.5 shows waveforms and spectra from the 16 August 1997 event in Kara Sea recorded at the AMD[1] station operated by KRSC. The analysis conducted by Schweitzer and Kennett (2002, 2007) suggested that this was an earthquake located in the middle crust. Different from the 24 December 2012 event, we see a rather impulsive S-arrival at the transverse component, and a larger fraction of the energy at higher frequencies.

Start time: 16 Aug. 1997, 02:11:18.2
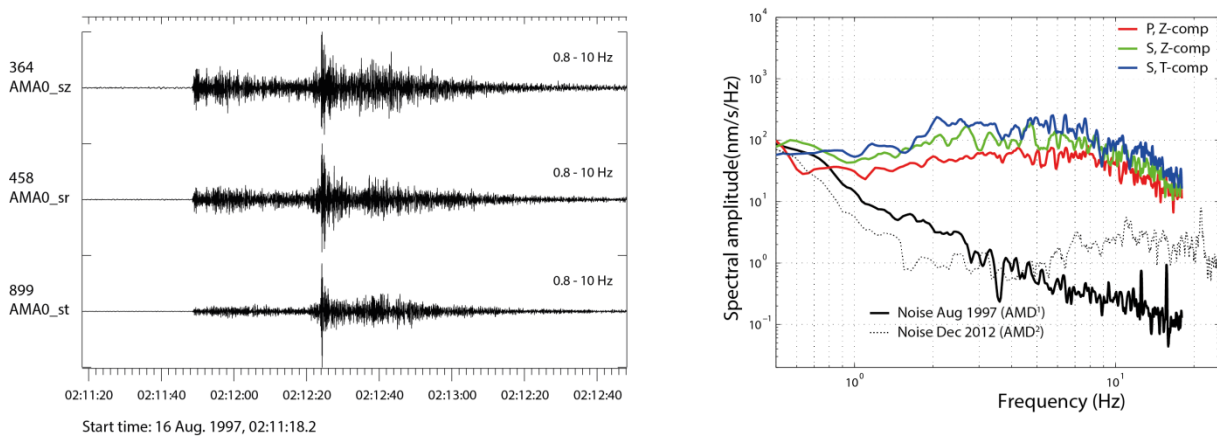
Fig. 6.3.5   The left-hand panel shows recordings at the AMD[1] station (operated by KRSC) of the Kara Sea event on 16 August 1997. The station-event distance is estimated at 334 km. See Fig. 6.3.4 for details. In this case the black dotted line shows the noise spectrum preceding the P-phase from 24 December 2012, observed at the AMD[2] station operated by IEPN UB RAS.

The spectral amplitude of the S-phase, as observed on the transverse horizontal component, is between a factor 3 and 4 larger than for the P-phase, observed on the vertical component, for the wide frequency band 1 – 8 Hz.

Waveforms and spectra from an event located about 275 km to the south of the Amderma station, which occurred on 31 January 1997, are shown in Fig. 6.3.6. Analysis of several years of AMD[1] data conducted by KRSC scientists has shown that the source region where this event occurred is characterized by large mining activity and numerous events, most likely mine blasts, occurring during working hours. The event on 31 January 1997 falls within this category. Different from the events shown in Figs. 6.3.4 and 6.3.5 we observe relatively small differences between the amplitudes of the P- and S-phases, and a relatively strong drop-off of energy at high frequencies. However, the event does not show any significant spectral scalloping which is sometimes associated with ripple-fired mine blasts and underwater explosions. We observe also in this case lower long-period noise levels during the Arctic winter (Jan 1997) as compared with the Arctic summer (Aug 1997), most likely caused by the variability of the strength of the microseisms due to frozen/unfrozen Arctic oceans.

Figs. 6.3.7 and 6.3.8 show ARCES waveforms and velocity spectra for the underwater explosions associated with the Kursk accident in year 2000 and the demolishing of the Kursk wreckage in 2002. The event-station distance is estimated at 463 km (see Table 6.3.2). For both events we observe significant spectral scalloping, and different from the 1997 Kara Sea event observed at AMD[1], there is no dominance of the S-phase energy on the horizontal transverse component.
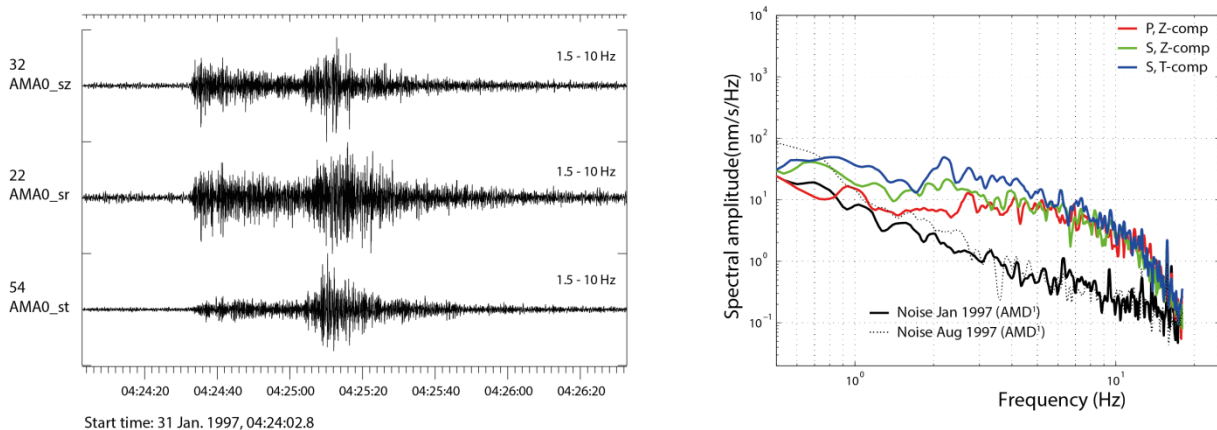

Fig. 6.3.6   *The left-hand panel shows recordings at the AMD[1] station (operated by KRSC) of a presumed mine blast in the Vorkuta region on 31 January 1997. The station-event distance is estimated at 275 km. See Fig. 6.3.4 for details. The black dotted line shows the noise spectrum preceding the P-phase from 16 August 1997 Kara Sea event, observed at the same station.*
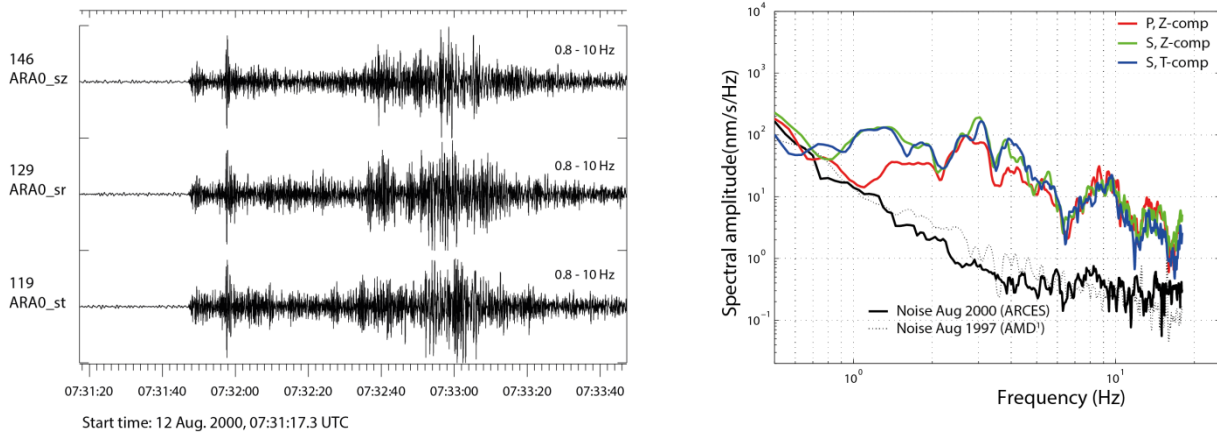
Fig. 6.3.7   The left-hand panel shows recordings at the center element of the ARCES array of the underwater explosion associated with the Kursk accident on 12 August 2000. The station-event distance is estimated at 463 km. See Fig. 6.3.4 for details. The black dotted line shows the noise spectrum preceding the P-phase from 16 August 1997 Kara Sea event, observed at AMD[1], and we notice good correspondence between the ARCES and AMD[1] noise levels.
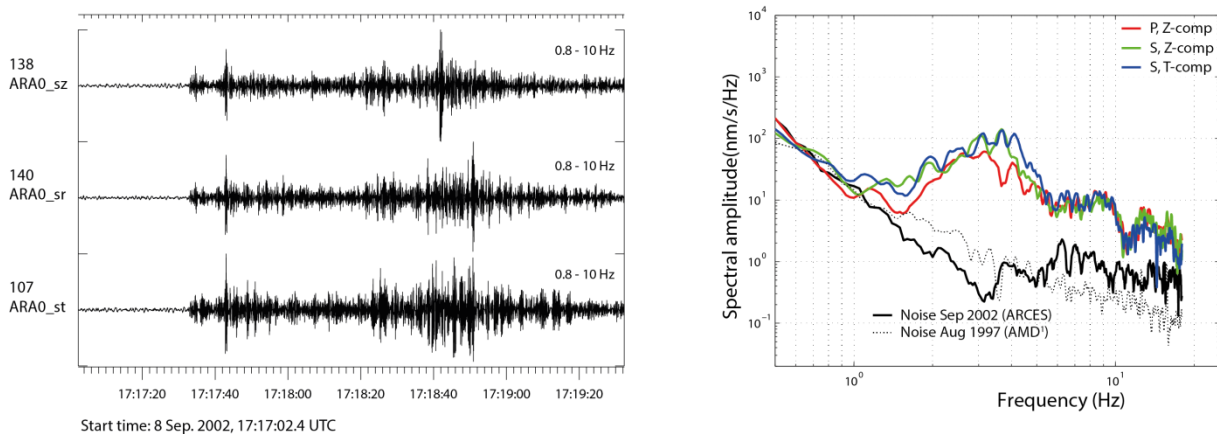

Fig. 6.3.8   The left-hand panel shows recordings at the center element of the ARCES array of the underwater explosion associated with the demolishing of the Kursk wreckage on 9 September 2002. The station-event distance is estimated at 463 km. See Fig. 6.3.4 for details. The black dotted line shows the noise spectrum preceding the P-phase from 16 August 1997 Kara Sea event, observed at AMD[1].

6.3.3   Summary

The new station in Amderma (AMD[2]) operated by the Institute of Ecological Problems of the North, Ural Branch of the Russian Academy of Sciences (IEPN UB RAS, Arkhangelsk, Russia) provided high signal-to-noise ratio recordings of the 24 December 2012 m_b 3.8 event in the north Ural Mountains region. For the time interval investigated (24 December 2012), AMD[2] shows lower background noise levels at frequencies below 3 Hz as compared with the examples shown for the previously operated AMD[1] station (January and August 1997). This may be explained by microseisms caused by ocean waves in the open, ice-free Barents and Kara Seas during the Arctic summer. For frequencies above 3

Hz, higher noise levels are observed for AMD[2], indicating anthropogenic noise sources in the vicinity of the station.

The observation of a very large S/P ratio, the largest S-phases found on the horizontal components, and the long-duration and energetic P- and S-codas suggest that site effects may influence the quality of the observations. Without a detailed study of site effects at the AMD[2] station, it is difficult to derive any firm conclusion regarding the characteristics of the 24 December 2012 event, but the large S/P ratio points in the direction of the event being an earthquake. The event is located in an area with no known mining activity and very low natural seismicity.

Acknowledgements

T. Kværna   **(NORSAR)**
G. Antonovskaya   **(IEPN UB RAS, Arkhangelsk, Russia)**
Y. Konechnaya   **(IEPN UB RAS, Arkhangelsk, Russia)**
V. E. Asming   **(KB GS RAS / KRSC, Apatity, Russia)**

References

Gibbons, S. J. and F. Ringdal (2006). The detection of low magnitude seismic events using array-based waveform correlation, Geophys. J. Int. 165, 149–165.

Kremenetskaya, E. O, and V.E. Asming (1998). Seismology on Kola: Monitoring Earthquakes and Explosions in the Barents Region, IRIS Newsletter XVII(2), 11-12

Ringdal, F., E.O. Kremenetskaya and V.E. Asming (2002). Observed Characteristics of Regional Seismic Phases and Implications for P/S Discrimination in the European Arctic. Pure and Applied Geophysics, Vol. 159, No. 4., pp. 701-719, doi:10.1007/s00024-002-8655-5

Schweitzer, J. and B.L.N Kennett (2002). Comparison of location procedures- The Kara Sea event of 16 August 1997. NORSAR Sci. Rep. 1-2002, 97-114..

Schweitzer, J. and B.L.N Kennett (2007). Comparison of location procedures: The Kara Sea event of 16 August 1997. Bull. Seismol. Soc. Am. 97, 389-400, doi 10.1785/0120040017.

6.4   Responses of the Infrasound Channels of ARCES and NORES

6.4.1   ARCES infrasound station instrument response

ARCES has been complemented with an experimental infrasound array. Three sites, ARA1, ARA2, ARB2, were installed in 2008 (Roth et al., 2008) and one additional site ARB3 was installed in 2010. The infrasound sensors and digitizers share the same pit as the seismic sensors and the acquisition system consists of a Güralp CMG-DM24 digitizer and a Martec MB2005 microbarometer.

Fig. 6.4.1   ARCES seismic and infrasound instrumentation, as installed in the field.

Fig. 6.4.1 above shows one ARCES pit with seismic and infrasound acquisition system. Clockwise from top we see the short-period GS13 seismometer (red casing), the pit tamper switch, the power/communication box, the Nanometrics digitizer for the seismic sensor, the MB2005 microbarometer , the Güralp CMG-DM24 digitizer (black Pelicase) and an inlet for the hose and GPS cable. Outside of the pit we are using four twelve meter long porous hoses laid out in a cross pattern acting as air inlet and wind noise reduction system. The infrasound data from the four pits are recorded on a laptop in the ARCES central recording facility for local backup and are immediately forwarded to the NORSAR data center at Kjeller.

Fig. 6.4.2   Picture of an opened MB2005 sensor (left: electronic card, right: barometric aneroid bellows and displacement transducer).

The response characteristics (poles/zeros, sensitivity values and digital filters) of the ARCES (ARCI) infrasound stations, equipped with MB2005 microbarometers and Güralp CMG-DM24 digitizers, are listed below.

	Real part	Imaginary part
Poles (2)		
Real pole	-0.03141593	0
Real pole	-99.9968941	0
Zeros (1)		
Zero	0	0

Table 6.4.1. Poles and zeros in rad/s for the MB2005 microbarometer (MARTEC, 2007).

The sensitivity of the MB2005 is equal to 20 mV/Pa.

The sensitivity values for the digitizers installed at ARCI are shown in Table 6.4.2.

Channel	Digitizer serial number	sensitivity
ARA1 BDF	A087	3.185 µV/count
ARA2 BDF	A222	3.189 µV/count
ARB2 BDF	A093	3.170 µV/count
ARB3 BDF	A216	3.178 µV/count

Table 6.4.2. Digitizer sensitivity values for the ARCES infrasound channels.

ARCES infrasound channels output data at 80 sps. The digital filters of the DM24 used to output this sampling rate are listed in Table 6.4.3. They correspond to a TTL value of 79 in the Güralp Systems tabulated, decimation cascade look-up system.

Input sampling rate	Digital filter name	Decimation	Symmetry	N coeff.
512000 sps	CS5376 stage 1, sinc-1	8	symmetric even	36
64000 sps	CS5376 stage 3, sinc-2	2	symmetric even	6
32000 sps	CS5376 stage 4, sinc-2	2	symmetric odd	7
16000 sps	CS5376 stage 5, FIR 1	4	symmetric even	48
4000 sps	CS5376 stage 6, FIR 2	2	symmetric even	126
2000 sps	DM24 FIR stage 1, SWA-D24-3D08	5	symmetric odd	501
400 sps	DM24 FIR stage 2, SWA-D24-3D08	5	symmetric odd	501

Table 6.4.3. Digital FIR filter cascade TTL = 79 and corresponding filter characteristics, used to output the selected sampling rate for the ARCES infrasound data.

The ARCES infrasound (ARCI) configuration described above and corresponding *Respid* flags (Pirli, 2010) are listed in Table 6.4.4.

Time	Channel	Installation name Respid(s)	System components	Calib [Pa/count]	Calper [s]
2008/05/13 – …	ARA1 BDF ARA2 BDF ARB2 BDF	ARCIBD1	MB2005 microbarometer CMG-DM24 digitizer	0.00015925 0.00015945 0.00015850	1
2010/10/08 – …	ARB3 BDF	ARCIBD1	MB2005 microbarometer CMG-DM24 digitizer	0.00015890	1

Table 6.4.4. Instrument configuration for the ARCES infrasound stations.

The amplitude and phase response of the ARCI configuration described above is shown in Fig. 6.4.5 (blue curve), at the end of section 6.4.2.

6.4.2   NORES infrasound station instrument response

In 2013, we started with the installation of infrasound sensors at the NORES array, with the intention to establish a 9-site infrasound array using the inner sites (ring A and B) of the seismic array. Three sites, NRA1, NRA2, NRA3, were completed in February and five more, NRA0, NRB2, NRB3, NRB4, NRB5, on April 19. At site NRB1 the infrasound sensor was installed on May 6, 2013. The infrasound acquisition system consists of Hyperion IFS-3000 sensors and Güralp CMG-DM24 digitizers. Infrasound and seismic sensors are co-located in the same pit and they are connected to the same digitizer. The seismic sensor is connected to the conventional Z, N, E channels of the digitizer and the infrasound sensor to the so-called X channel (the X-channels have similar sensitivities to the

conventional data channels and can be used amongst others as calibration signal monitor). Data are recorded in the NORES central recording facility and forwarded to the NORSAR data centre at Kjeller. Fig. 6.4.3 below shows the geometry of the NORES array. The sites marked with magenta symbols have seismic and infrasound sensors. The outer sites marked in red are currently not used, but will be equipped with seismic sensors at a later time.
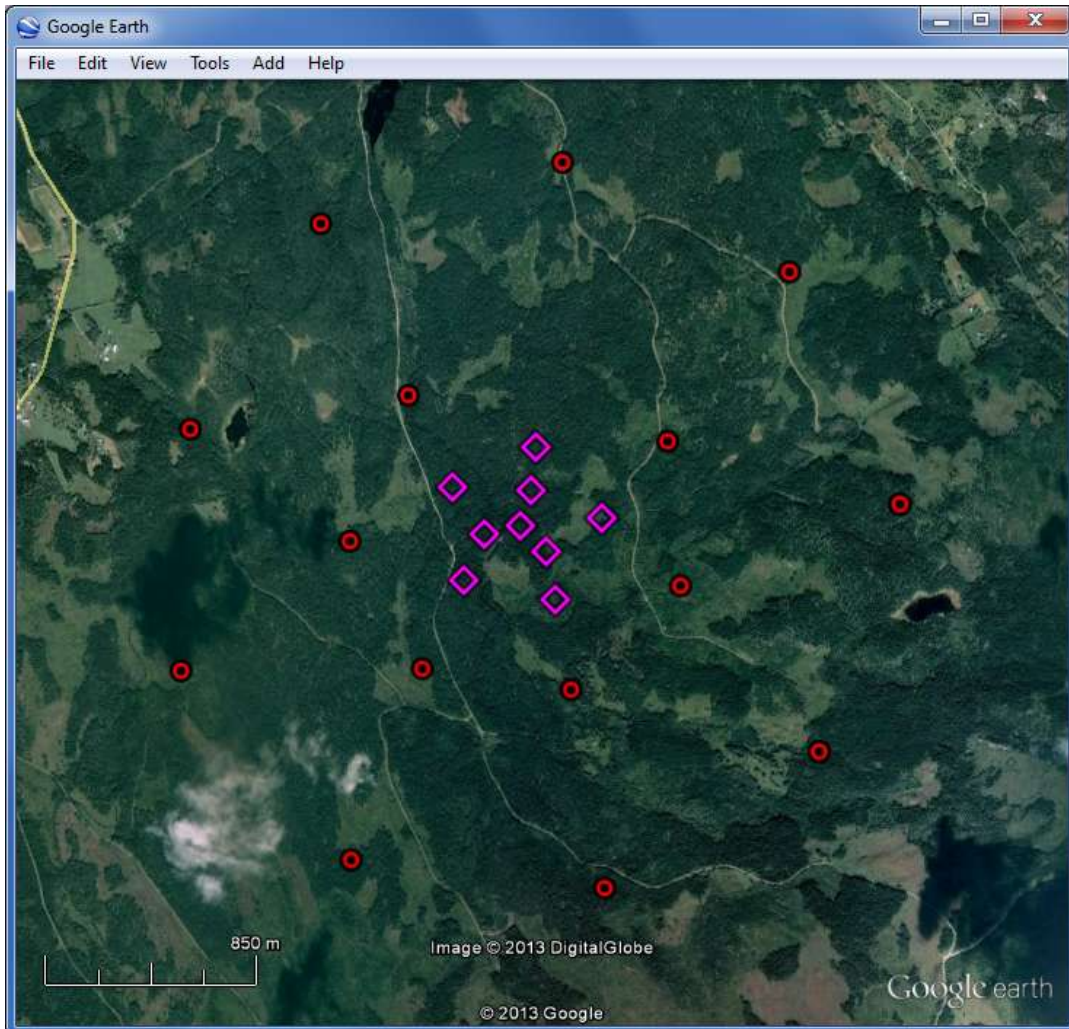

Fig. 6.4.3   Map of NORES array location and geometry. Circles note future sites with seismic channels, while rhombuses note currently sites with both seismic and infrasound channels (top). Cover (left) and entrance (right) to one of the NORES sites (bottom).

For the time being, we do not have a wind noise reduction system for the infrasound sensors. The sensor is simply placed at the floor of the pit and air pressure variations can access the pit through the gap between the lid and the rim of the pit. We are using screw nuts and washers placed on the rim of the entrance (see Fig. 6.4.3, photo at bottom right) to create a small gap/inlet to the pit.

Fig. 6.4.4   NORES seismic and infrasound instrumentation, as installed in the field.

Fig. 6.4.4 above shows clockwise from the top left corner one of the two horizontal short-period seismic sensors (red casing), the seismometer pre-amplifiers, a coupling box, the Hyperion infrasound sensor (white casing) and the Güralp CMG-DM24 digitizer. The inlet of the IFS-3000 is protected by a piece of sponge rubber.

The response characteristics (poles/zeros, sensitivity values and digital filters) of the NORES infrasound stations, equipped with Hyperion IFS-3000 infrasound sensors and Güralp CMG-DM24 digitizers are listed below.

	Real part	Imaginary part
Poles (3)		
Real pole	-0.00931796379	0
Real pole	-0.0212811486	0
Real pole	-0.185291134	0
Zeros (3)		
Zero	0	0
Zero	0	0
Zero	0	0

Table 6.4.5. Poles and zeros in rad/s for the IFS-3000 infrasound sensor (Hyperion Technology Group, 2012).

The sensitivity of the IFS-3000 is equal to 150 mV/Pa at 1 Hz.

The sensitivity values for the digitizers installed at NORES are shown in Table 6.4.6. As mentioned earlier, the Calibration Signal Monitoring channel of the digitizer is being used for the infrasound channels.

Channel	Digitizer serial number	sensitivity
NRA0 BDF	A203 (A203X2)	3.185 µV/count
NRA1 BDF	A098 (A098X2)	3.177 µV/count
NRA2 BDF	A085 (A085X2)	3.171 µV/count
NRA3 BDF	A253 (A253X2)	3.180 µV/count
NRB1 BDF	A309 (A309X2)	3.173 µV/count
NRB2 BDF	A247 (A247X2)	3.173 µV/count
NRB3 BDF	A287 (A287X2)	3.184 µV/count
NRB4 BDF	A217 (A217X2)	3.182 µV/count
NRB5 BDF	A313 (A313X2)	3.162 µV/count

Table 6.4.6. Digitizer sensitivity values for the NORES infrasound channels.

NORES infrasound channels output data at 80 sps. The digital filters of the CMG-DM24 used to output this sampling rate are listed in Table 6.4.7. They correspond to a TTL value of 91.

Input sampling rate	Digital filter name	Decimation	Symmetry	N coeff.
512000 sps	CS5376 stage 1, sinc-1	8	symmetric even	36
64000 sps	CS5376 stage 3, sinc-2	2	symmetric even	6
32000 sps	CS5376 stage 4, sinc-2	2	symmetric odd	7
16000 sps	CS5376 stage 5, FIR 1	4	symmetric even	48
4000 sps	CS5376 stage 6, FIR 2	2	symmetric even	126
2000 sps	DM24 FIR stage 1, SWA-D24-3D08	5	symmetric odd	501
400 sps	DM24 FIR stage 2, SWA-D24-3D08	5	symmetric odd	501

Table 6.4.7. Digital FIR filter cascade TTL = 91 and corresponding filter characteristics, used to output the selected sampling rate for the NORES infrasound data.

The NORES infrasound configuration described above and corresponding *Respid* flags (Pirli, 2010) are listed in Table 6.4.8.

Time	Channel	Installation name Respid(s)	System components	Calib [Pa/count]	Calper [s]
2013/02/06 – …	NRA1 BDF NRA2 BDF NRA3 BDF	NORESBD1	IFS-3000 infrasound sensor CMG-DM24 digitizer	0.00002118 0.00002114 0.00002120	1
2013/04/19 – …	NRA0 BDF NRB2 BDF NRB3 BDF NRB4 BDF NRB5 BDF	NORESBD1	IFS-3000 infrasound sensor CMG-DM24 digitizer	0.00002123 0.00002115 0.00002123 0.00002121 0.00002108	1
2013/05/06 – …	NRB1 BDF	NORESBD1	IFS-3000 infrasound sensor CMG-DM24 digitizer	0.00002115	1

Table 6.4.8. Instrument configuration for the NORES infrasound stations.

The amplitude and phase response for the NORES infrasound configuration described above is shown in Fig. 6.4.5 (red curve). The shaded area marks the frequency range beyond the Nyquist frequency.
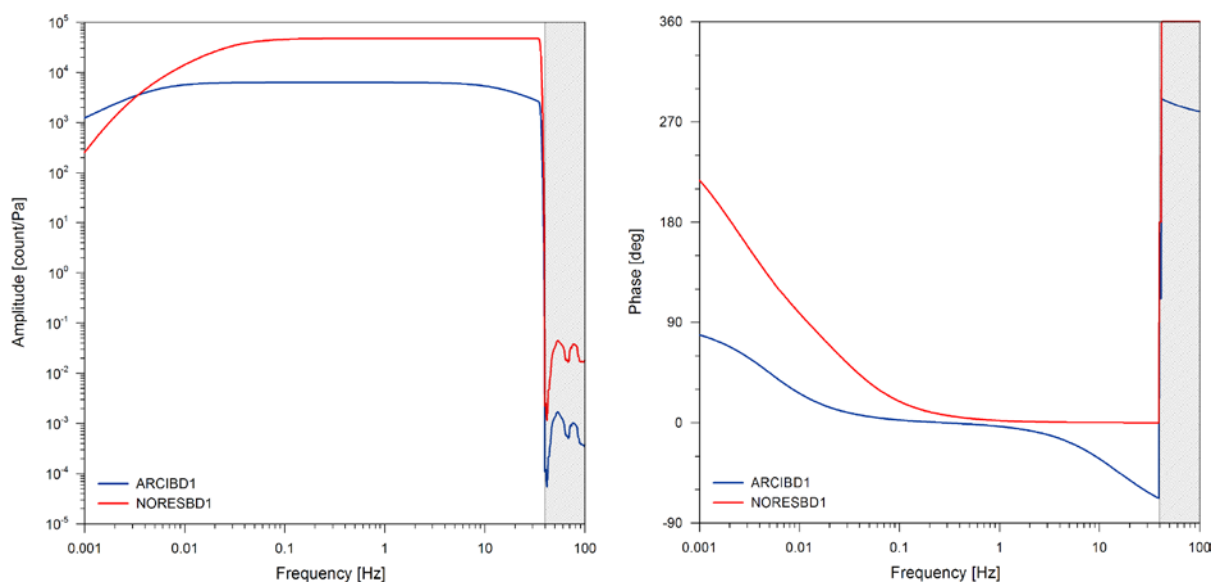
Fig. 6.4.5   Amplitude and phase response for the infrasound stations of ARCES (blue) and NORES (red). Shading marks the frequency range beyond the Nyquist (= 40 Hz).

M. Roth
M. Pirli

References

Hyperion Technology Group (2012): IFS-3000 Series Infrasound Sensor User Manual. Hyperion
        Technology Group, Inc., Tupelo, Mississippi, 11 p.

MARTEC (2007): MB2005 User Manual. Reference 14643-C, Edition 17/01/2007, CEA, 20 p.

Pirli, M. (2010): NORSAR System Responses Manual, 2nd Edition. NORSAR, Kjeller, Norway, 180 p.

Roth, M., J. Fyen and P.W. Larsen (2008): Setup of an experimental infrasound deployment within
        the ARCES array. NORSAR Sci. Rep. 2-2008 , Kjeller, Norway, 52-59.

6.5   Classifying Seismic Signals at Small–Aperture Arrays via Stochastic Modeling of F-K Image Sequences

6.5.1   Automatic seismic event classification systems

For any seismic monitoring task (volcano, geothermal, microseismic, …) it is desirable to detect and classify seismic events consistently (objectively and time-invariantly) and with little/no need for (costly) expert intervention. The seismic event categorization should be based on wave field properties including temporal structure and context. A similar problem in the realm of speech recognition applications is termed the word spotting problem. Thus, Ohrnberger (2001) transferred successfully hidden Markov model (HMM) techniques from the field of acoustic level speech recognition to tackle the seismic event spotting task applied to volcano-seismic signal observations. Since then, a number of HMM based classification approaches have been reported in seismology (*e.g.*, Beyreuther and Wassermann, 2008; Benitez *et al.*, 2007; Hammer *et al.*, 2012).

6.5.2   Seismic events casted as doubly stochastic process

HMMs are doubly stochastic processes that allow modeling of trajectories of observed sequences forming a seismic event (signal of interest) in a representative multidimensional space, which is referred to as feature space. In Fig. 6.5.1 (top) we show examples of trajectories for two distinct events in a two-dimensional feature space (*e.g.*, this may be amplitude and dominant frequency). Different signal properties result in clearly distinct paths traversing the feature space in time.
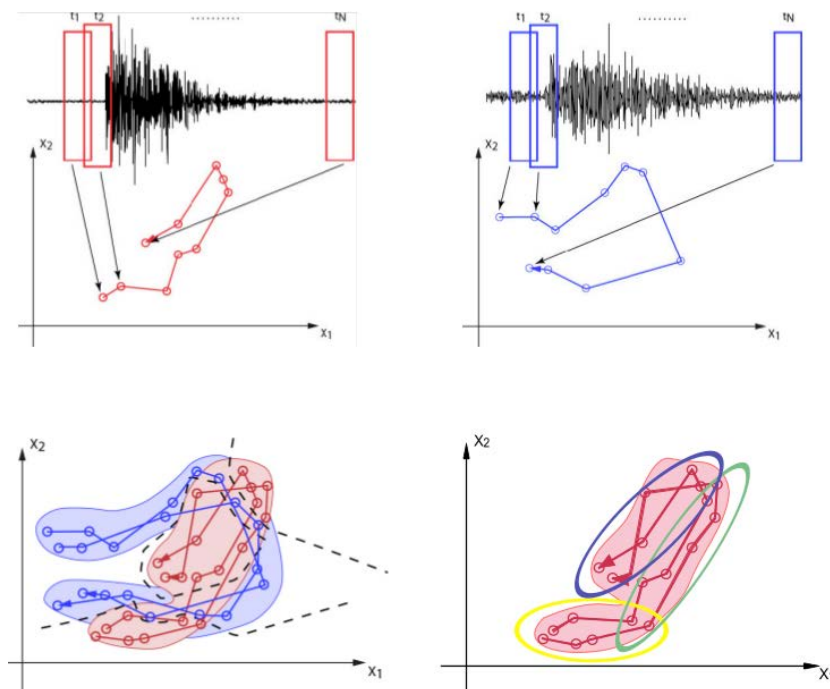
Fig. 6.5.1   Modeling trajectories of feature vector sequences as doubly stochastic processes.

When there are several examples for one event class that share similar behavior in feature space, similar trajectories will be observed. The distribution of observed trajectories for one and the same event type may then be described by a dynamically evolving probability density function of

observations (Fig. 6.5.1, bottom right). One particularly well suited stochastic model for describing such dynamically evolving probability density functions are Hidden Markov Models (HMM). Thus, the distribution of trajectories for any event class can be modeled as outcome of a HHM. The first underlying (hidden) process of a HMM creates a sequence of discrete states obeying Markov properties. At each time step, the system emits an observation drawn from a state-dependent multivariate Gaussian (see Fig. 6.5.2). For details about the underlying mathematics and the main standard computational issues about HMMs (*i.e.*, parameter learning) we refer here to the tutorial paper by Rabiner (1989), to fundamental work on the speech processing by Rabiner and Juang (1993) or the summary given in Ohrnberger (2001).
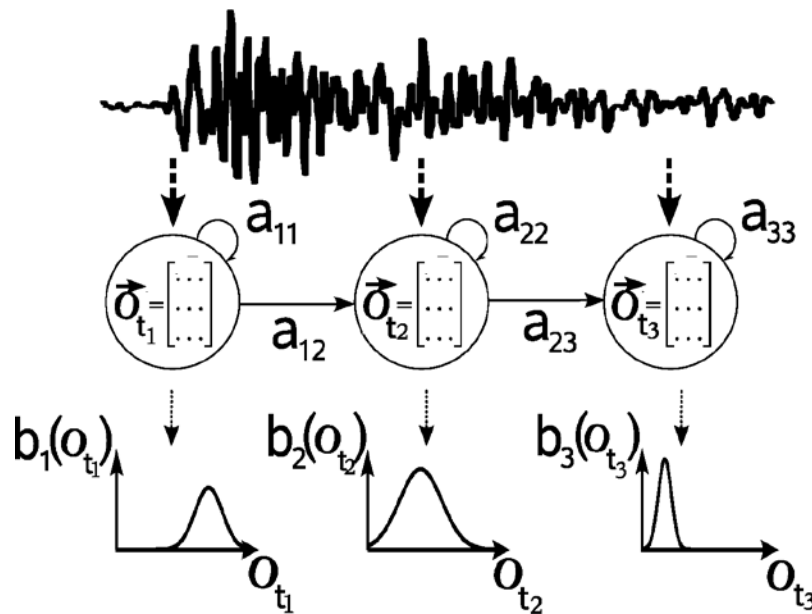
Fig. 6.5.2   HMM as a double stochastic process. The underlying state sequence of hidden state variables creatse an observation (seismic time series attributes) at each time step. The sequences of seismic time series attributes are then interpreted as having been created by a HMM. Model parameters are transition probabilities (a_{ij}) and output probability density functions (PDFs) related to a current state index (b_i).

The parameters of HMMs (state transition probabilities and output power-density-functions) are usually learned for each class of interest from a large training set (several tens of examples needed for each class). Here, we follow an alternative approach recently proposed by Hammer *et al.* (2012), which avoids the costly preparation of training sets. Indeed it is possible to start off with a single reference event by exploiting abundant information from unlabeled and therefore cheap training data (mostly continuous background/noise wave field information). The main idea for the proposed training procedure is to estimate with high confidence parameters of the probability density functions describing the general wave field characteristics in feature space (see Fig. 6.5.3). The parameters of the event class are then estimated from adjustments to these probability density functions based on a single/few reference event(s) for a specific class (see Fig. 6.5.4).
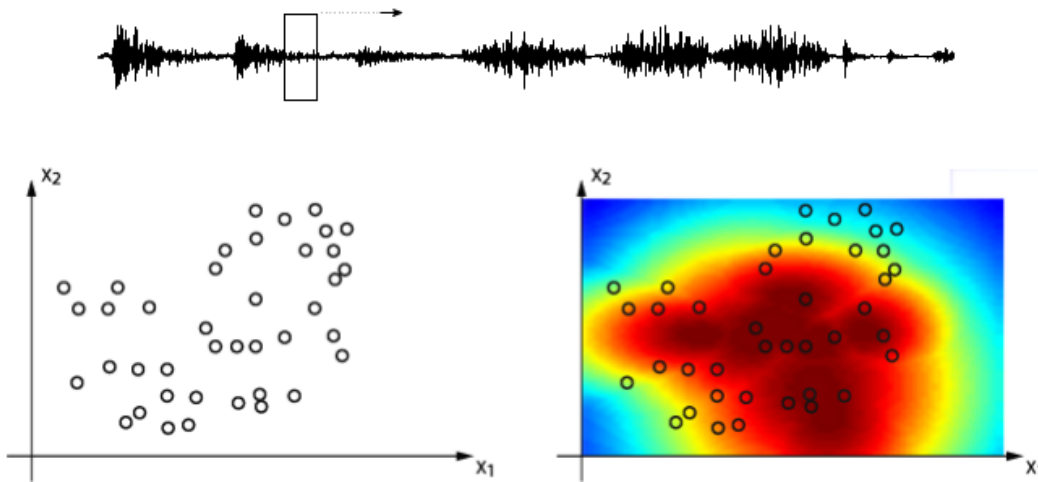
Fig. 6.5.3   *Learning general background model from continuous data (unsupervised clustering from "cheap" training data).*
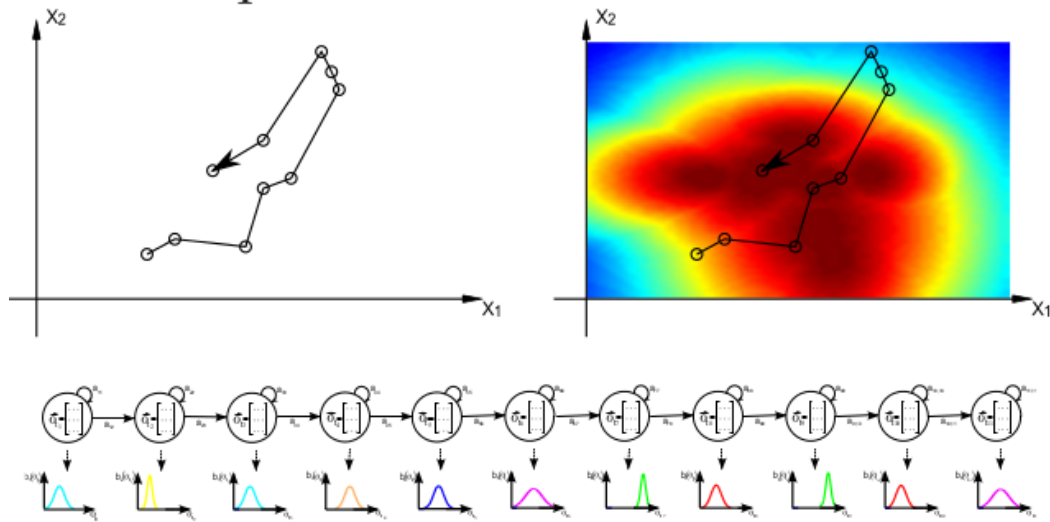

Fig. 6.5.4   *Single reference waveform to update an event-specific classifier. The reference pattern is modeled as sequence of "visited" Gaussians.*

6.5.3 Sliding window multi-broadband f-k array analysis as representative feature sequence

Seismic arrays are superior to single station observations allowing for determination of wave field direction and apparent speed along the earth surface. Three-component broadband arrays like SPITS (located on the Svalbard Archipelago, Norway) even enable a quite complete decomposition of the entire seismic wave field. We apply a sliding window f-k analysis in three overlapping, broad frequency bands to the vertical component recordings of SPITS. The example given in Fig. 6.5.5 shows that blurry f-k images indicate "noise" or non-plane wave / multiple wave arrivals. Clear arrivals are easily detected by eye as the focused f-k image resembles the theoretical broadband array response pattern shifted to the wave group arrival's slowness vector position.
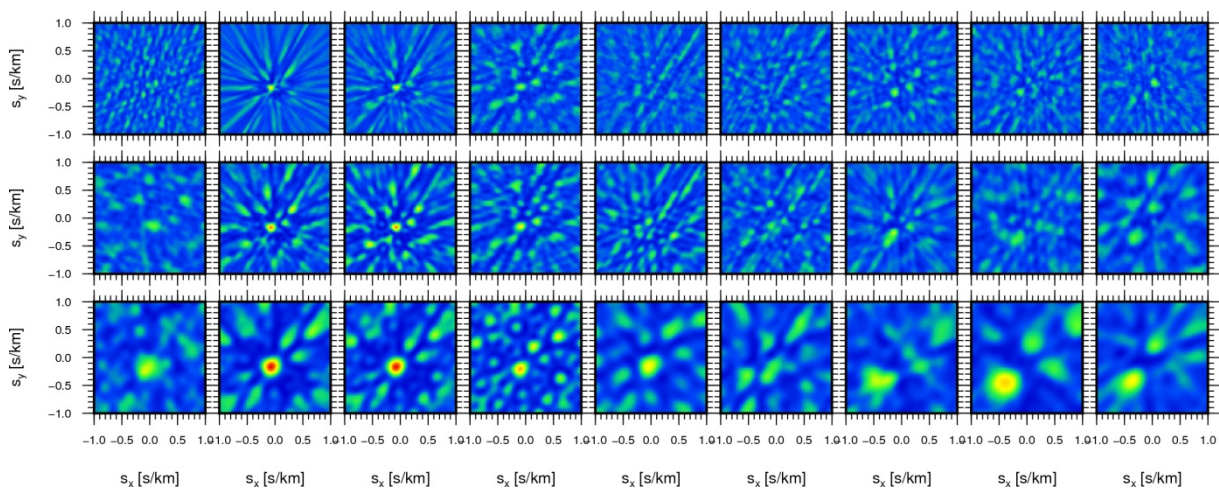
Fig. 6.5.5   Temporal sequence of f-k images computed in sliding window analysis for multiple broad frequency bands (from bottom to top row evaluated frequency bands are 1.5-4.5 Hz, 3-9 Hz, and 6-18 Hz; horizontal axis indicates time).

In order to encode the visual impression of an f-k image, we compute additionally the residual f-k image by subtracting the theoretical array response centered on the maximal coherent plane wave (see Fig. 6.5.6). Then we derive robust statistical parameters from broadband f-k and residual f-k images computed for bands 1.5 – 4.5 Hz, 3 – 9 Hz, and 6 – 18 Hz (101 × 101 grid in [-1, 1] s/km in 1.5 s windows and 0.1 s steps). In total we obtain a set of 51 parameters, including: μ, σ, rms, med, L1-scale, sx, sy, max/min-coherence, max-power. Certainly this selection is just one possible encoding of the f-k image information that would span a 6 x 101 x 101 = 61206 dimensional feature space in its raw representation.
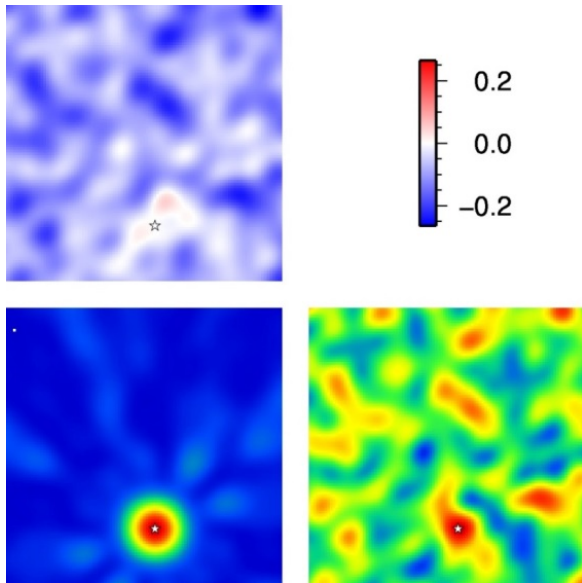
Fig. 6.5.6
Top left: Residual image resulting from subtracting the theoretical response from the observed f-k image. Bottom right: example of observed f-k image for a broad frequency band. Bottom left: Theoretical array response function computed for the same frequency band and centered on the most coherent plane wave arrival (maximum of the f-k image on the bottom right).

The 51-dimensional feature space ($f \in R^{51}$) has been examined visually. The discriminative power of features was judged when reviewing the temporal structure of feature series for selected events (Figs. 6.5.7 and 6.5.8).
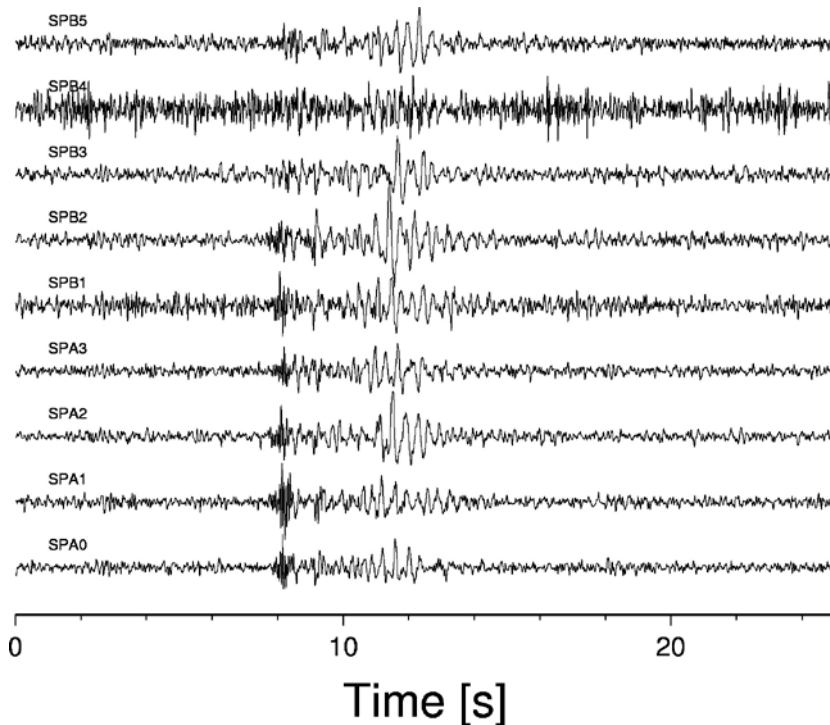
Fig. 6.5.7
The reference event observed at SPITS.

20110822070949.SPITS.cartesian.multibbfk.max
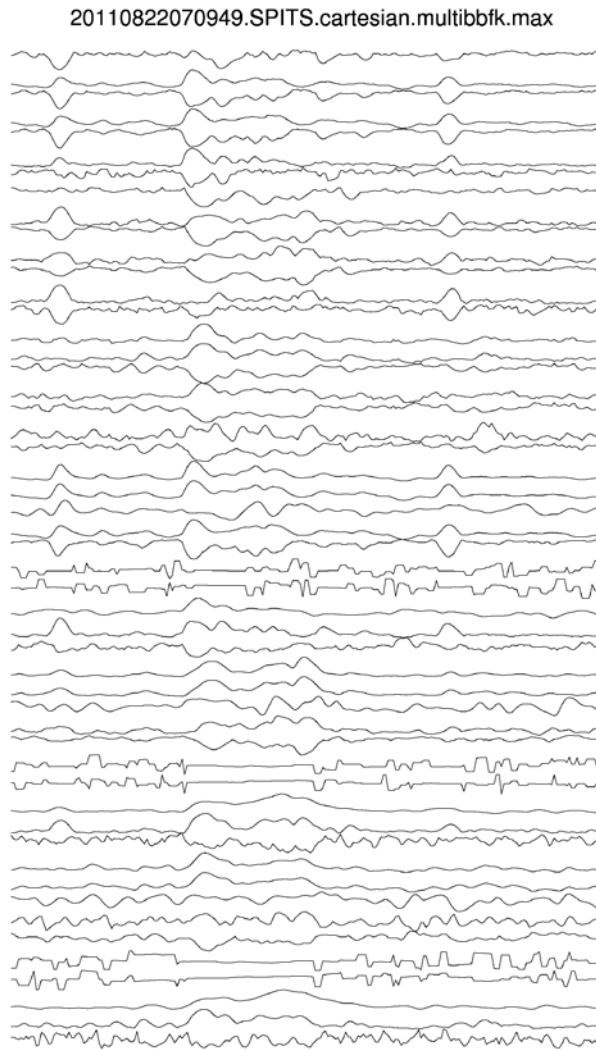
Fig. 6.5.8   Time series of 51 feature components for the reference event shown in Fig. 6.5.7.

Simple crossplots - omitting the temporal context - were used for finding correlated feature components (Fig. 6.5.9) for a large number of observations (6 hours of background data). Finally, we selected feature subsets with dimensions of 18, 21, 27, 33, and 39, based on the findings of the visual control and by seismological expertise. Those feature sets were then tested for the classifier design and the classification of continuous data.
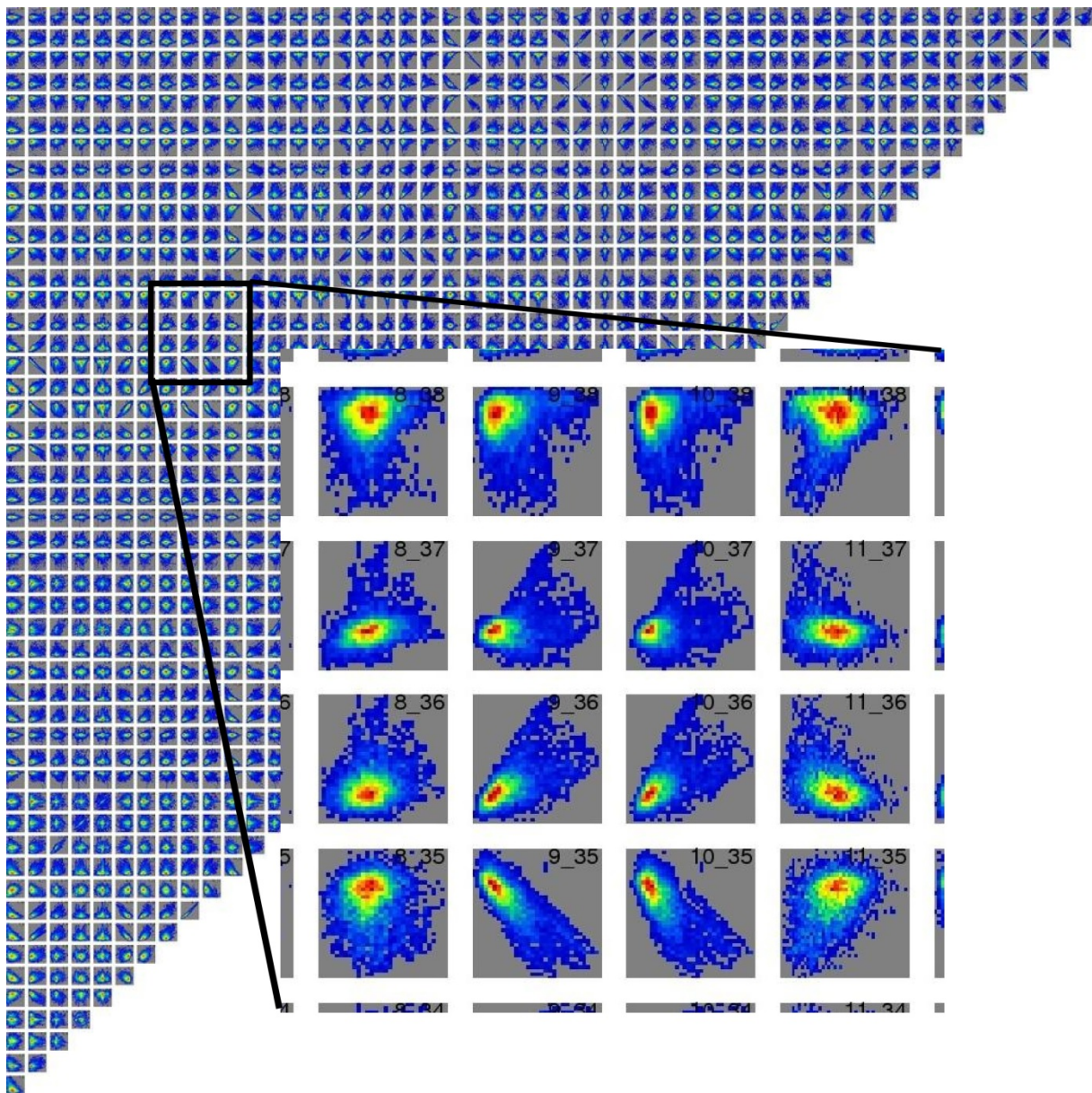
Fig. 6.5.9   Density crossplot of all pairs of feature components (see Fig. 6.5.8) for 6 hours of background data.

A large set of (cheap) unlabeled feature vectors are the ingredients for learning the background wave field properties as multivariate Gaussian mixture (Gaussian Mixture Model - GMM) in unsupervised fashion (k-means algorithm). Event HMM classifiers are then constructed on the base of the GMM using a single reference feature vector sequence for updating the HMM parameters (compare also Fig. 6.5.3 and 6.5.4). Both background and event models are finally integrated as a parallel grammar network (see Fig. 6.5.10). At each time step, a partial sequence of feature vectors is presented to the classifier network and the most likely hidden state path is decoded using the Viterbi-algorithm (Viterbi, 1967; Forney, 1973). Whenever the Viterbi-path is passing states related to the event HMM, a detection of this event-class is declared. Note that also multi-class systems can be constructed easily by adding more classifiers in parallel to the grammar network.
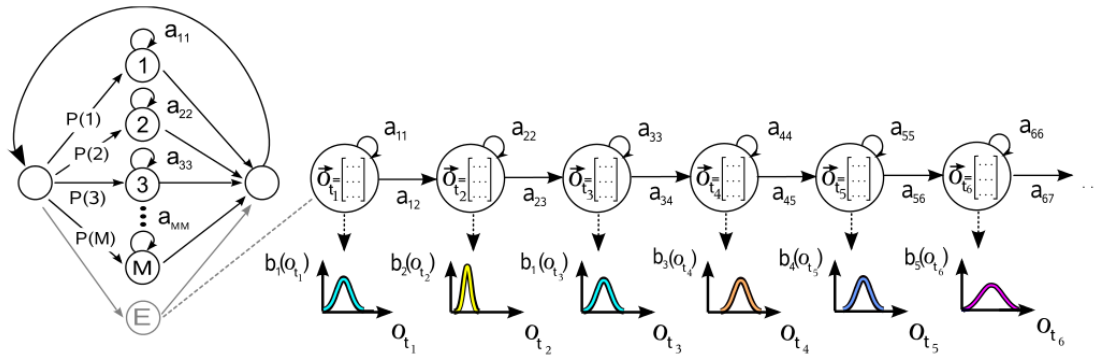
Fig. 6.5.10 Parallel grammar network in which each Gaussian mixture is part of the background model description and the event model HMM is connected in parallel.

An alternative approach for applying the HMM based detector to continuously recorded data is the use of running classifier and in parallel keeping track at each time step of the likelihood scores (Fig. 6.5.11). We may choose to use a noise only, or noise-event-noise grammar types and compare the average log likelihoods for the models in short time windows. This approach enables a judgment of the quality of detection by the log-likelihood difference as a confidence measure, but usually shows less accuracy in the segmentation of the event start and end times.
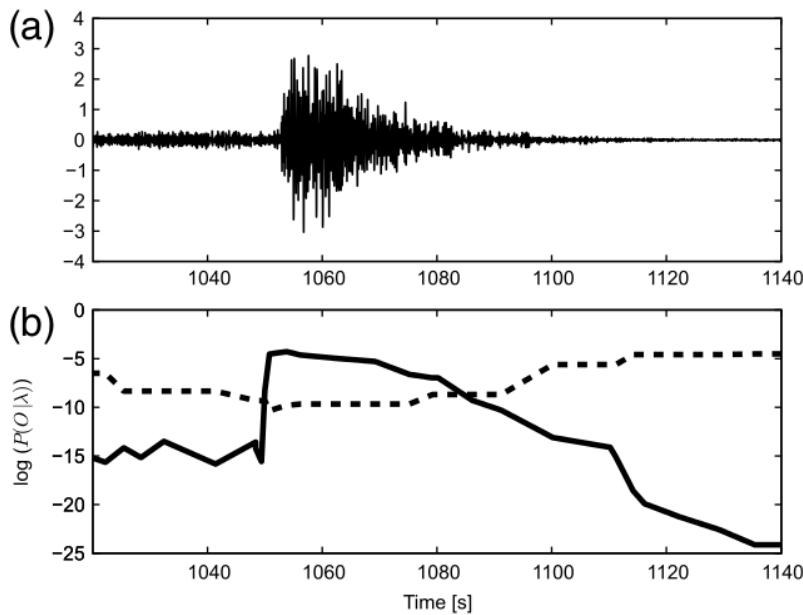

Fig. 6.5.11 Likelihood scoring of alternative HMM models (background and event models).

6.5.4 Test data at SPITS array and preliminary results

We use data from the SPITS array as a test environment to adapt the recently proposed classification technique by Hammer *et al.* (2012) for array settings. Our main goal is to:

- screen out events not interesting to analysts in NDC/CTBT context
- count glacier related events as a link to climatic change in arctic regions

We used 6 hours of continuous recordings for learning the background model (typical example of background activity shown in Fig. 6.5.12) and used a single record of an event which is assumed to be related to glacier activity (see Fig. 6.5.7). We expect glacier related events to show quite some variation in wave field appearance due to the variability of source location and complexity of source processes. We consider the HMM-based approach to be particularly suited for this task. One (rather typical) restriction for evaluating the quality of the classifier approach in a quantitative way is the lack of real ground truth for the observed seismicity.
There are only two tunable parameters for the classifier:

i)   the number of Gaussians;
ii)   feature vectors pre-whitened or not.

In combination with the distinct feature subsets there are then numerous settings to be considered. In Fig. 6.5.13 we show brief examples of classifier outcomes for the same waveform portion (only the vertical seismogram at the array site SPA0 is shown). Note the distinct scoring techniques (parallel classifiers vs. network).

6.5.5 Concluding remarks

- Preliminary classification results obtained for selected time windows allow the detection of a predefined event class (glacier related short and high frequency events).
- However, the comparison of results for distinct feature sets and parameters indicates sub-optimal performance. Spurious detections occur frequently.
- We conclude that there is a need for retraining and testing other selections of background training data.
- The final aim is to run the classifier for a longer time span of data with confidence. This ultimate goal requires ground truth data, which is at the moment lacking.
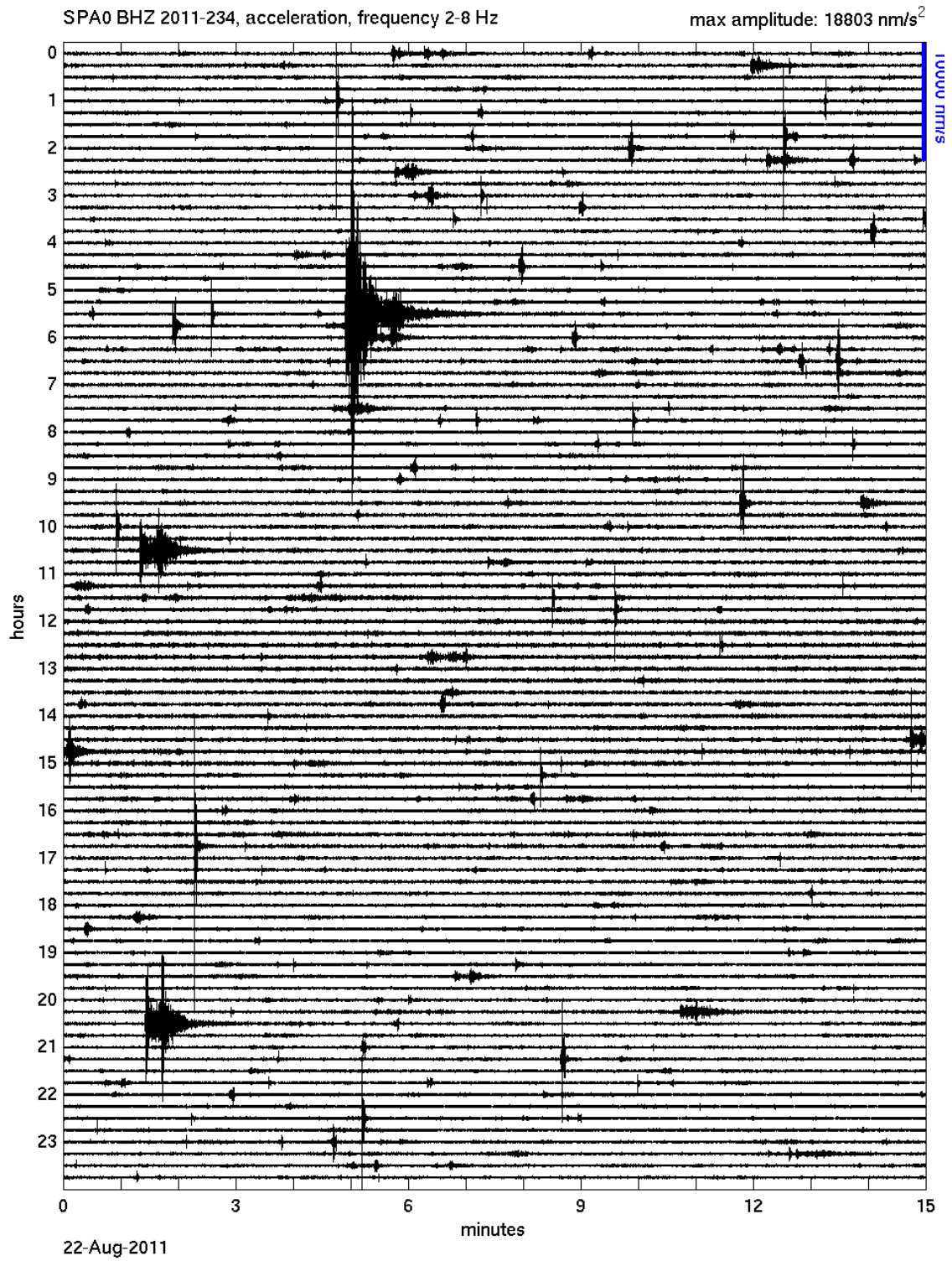
Fig. 6.5.12 *A typical daily helicorder plot simulation for station SPA0 provides insight of the normal seismic activity levels at this arctic island region.*
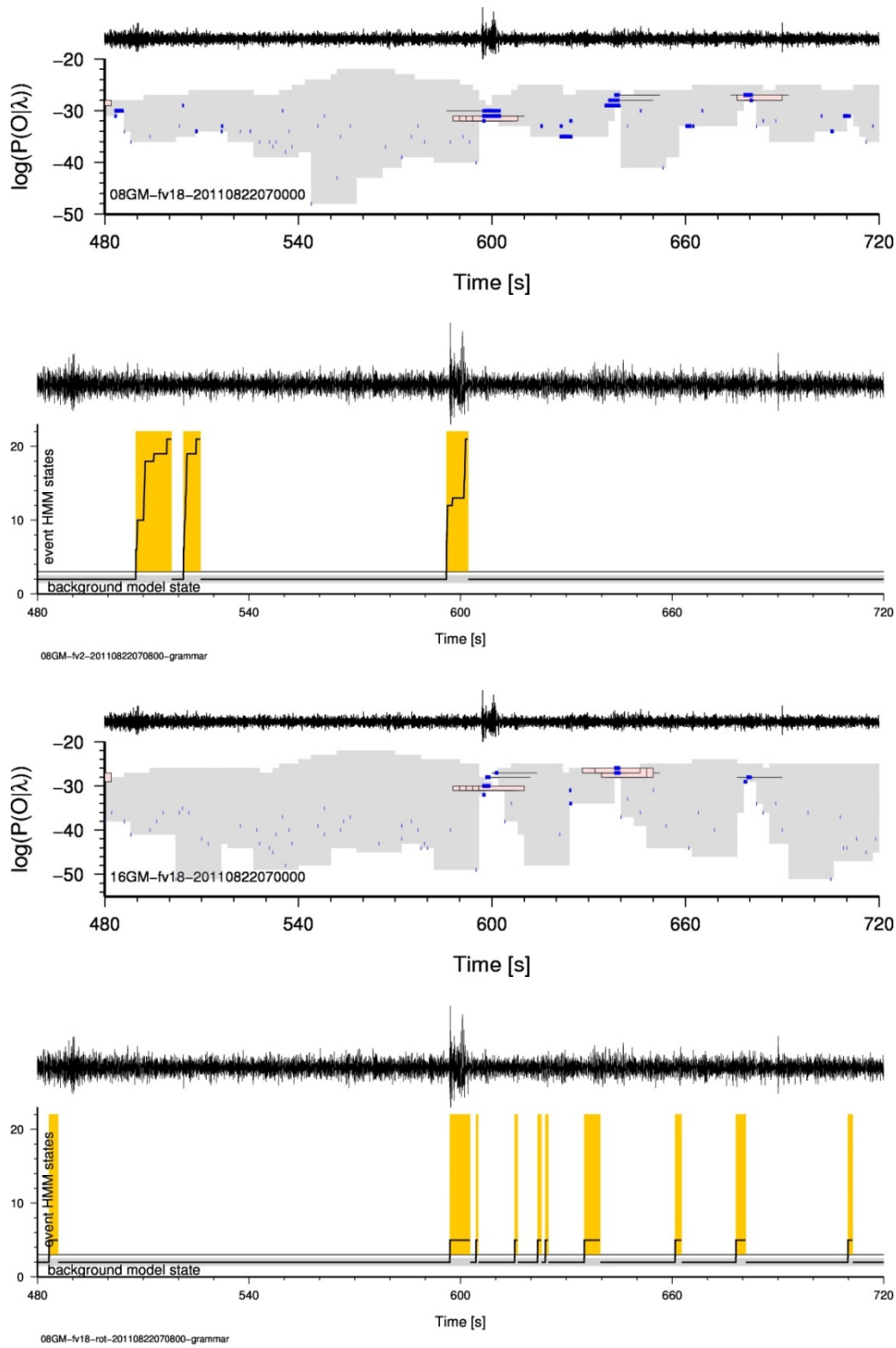
Fig. 6.5.13 *Results of continuous classification (just a short example window for visualization) using either the grammar network or the relative likelihood scoring approach. Spurious detections are visible in both approaches and indicate not yet optimal classification performance.*

Matthias Ohrnberger, University of Potsdam
Conny Hammer, University of Potsdam
Nikos Giannotis, University of Potsdam
Johannes Schweitzer

References

Benitez, M.C., J. Ramirez, J.C. Segura, J.M. Ibanez, J. Almendros, A. Garcia-Yeguas and G. Cortes (2007). Continuous HMM-based seismic-event classification at Deception Island, Antarctica. IEEE Trans. Geosciences Remote Sensing, 45(1), 138–146.

Beyreuther, M. and J. Wassermann (2008). Continuous earthquake detection and classification using discrete Hidden Markov Models. Geophys. J. Inter., 175(3), 1055–1066.

Forney, G. (1973). The Viterbi algorithm. Proc. IEEE, 61(3), 268 -278.

Hammer, C., M. Beyreuther and M. Ohrnberger (2012). A seismic event spotting system for volcano fast response systems. Bull. Seism. Soc. Amer., 102(3), 948-960.

Ohrnberger, M. (2001). Continuous automatic classification of seismic signals of volcanic origin at Mt. Merapi, Java, Indonesia. Ph.D. Thesis, Universität Potsdam.

Rabiner, L. (1989). A tutorial on hidden Markov models and selected applications in speech recognition. Proc. IEEE, 77(2), 257 -286.

Rabiner, L. and B. Juang (1993). Fundamentals of speech recognition. Prentice-Hall, XXXV+507 pp.

Viterbi, A. (1967). Error bounds for convolutional codes and asymptotically optimal decoding algorithm. IEEE Trans. Inf. Theory, IT-13(2), 260 -269.

Report Documentation Page

NORSAR

Report Number: 13-007	Confidential: Unlimited: x	External: Internal: x	NORSAR Project No.
Title:	NORSAR Scientific Report No. 2-2012 Semiannual Technical Summary 1 July – 31 December 2012		
Client:	The work reported in this Semiannual Technical Summary is supported by various clients and relates to nuclear test ban verification activities at NORSAR		
Project Managers:			
Authors / Prepared by:	Tormod Kværna (Ed.)		
Submitted to:			
Contract Reference:			
Archive reference:	NORSAR folders/projects/Semiannual/Dec12		
Approved by: NDC Manager: Program Manager: Program Coordinator:	Name: Jan Fyen Tormod Kværna Svein Mykkeltveit	Signature: *Tormod Kværna*	Date: 15 June 2013